Clusters and groups of galaxies

6

Galaxies are not uniformly distributed in space, but instead show a tendency to gather together in *galaxy groups* and *clusters of galaxies*. This effect can be clearly recognized in the projection of bright galaxies on the sky (see Figs. 6.1 and 6.2). The Milky Way itself is a member of a group, called the Local Group (Sect. 6.1), which implies that we are living in a locally overdense region of the Universe.

The transition between groups and clusters of galaxies is smooth. Historically, the distinction was made on the basis of the number of their member galaxies. Roughly speaking, an accumulation of galaxies is called a group if it consists of $N \lesssim 50$ members within a sphere of diameter $D \lesssim 1.5h^{-1}$ Mpc. Clusters have $N \gtrsim 50$ members and diameters $D \gtrsim 1.5h^{-1}$ Mpc. A formal definition of a cluster is presented further below. An example of a group and a cluster of galaxies is displayed in Fig. 6.3.

Clusters of galaxies are very massive: typical values are $M \gtrsim 3 \times 10^{14} M_\odot$ for massive clusters, whereas for groups $M \sim 3 \times 10^{13} M_\odot$ is characteristic, with the total mass range of groups and clusters extending over $10^{12} M_\odot \lesssim M \lesssim$ few$\times 10^{15} M_\odot$.

Originally, clusters of galaxies were characterized as such by the observed spatial concentration of galaxies. Today we know that, although the galaxies determine the optical appearance of a cluster, the mass contained in galaxies contributes only a small fraction to the total mass of a cluster. Through advances in X-ray astronomy, it was discovered that galaxy clusters are intense sources of X-ray radiation which is emitted by a hot gas ($T \sim 3 \times 10^7$ K) located between the galaxies. This intergalactic gas (*intracluster medium*, ICM) contains more baryons than the stars seen in the member galaxies. From the dynamics of galaxies, from the properties of the intracluster gas, and from the gravitational lens effect we deduce the existence of dark matter in galaxy clusters, dominating the cluster mass like it does for galaxies.

Clusters of galaxies play a very important role in observational cosmology. They are the most massive bound and relaxed (i.e., in a state of approximate dynamical equilibrium) cosmic structures, and therefore mark the most prominent density peaks of the large-scale structure in the Universe. For that reason, their cosmological evolution is directly related to the growth of cosmic structures, as will be discussed in Chaps. 7 and 8. Due to their high galaxy number density, clusters and groups are also ideal laboratories for studying interactions between galaxies and their effect on the galaxy population. For instance, the fact that elliptical galaxies are preferentially found in clusters indicates the

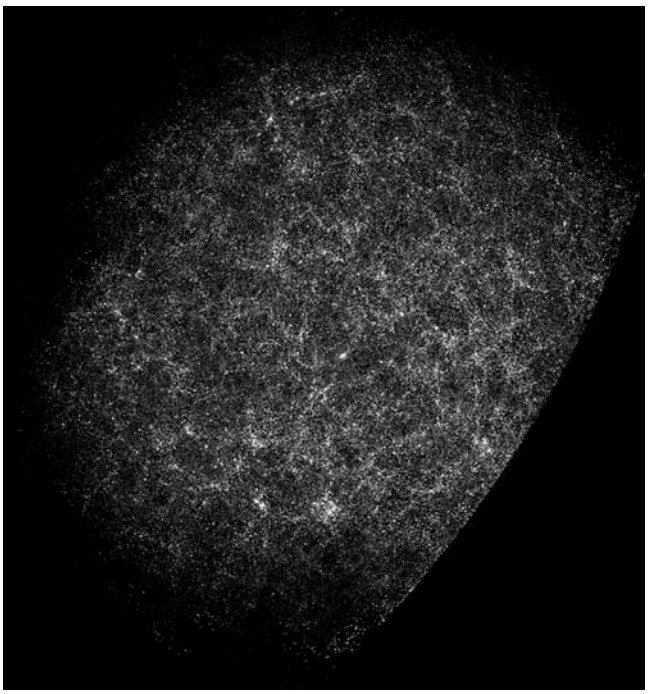

Fig. 6.1 The distribution of galaxies in the Northern sky, as compiled in the Lick catalog. This catalog contains the galaxy number counts for 'pixels' of $10' \times 10'$ each. It is clearly seen that the distribution of galaxies on the sphere is far from being homogeneous. Instead it is distinctly structured. For an all-sky map of bright galaxies, as observed at near-IR wavelengths, see Fig. 1.52. Source: Webpage E.J. Groth, Princeton University; adapted from M. Seldner et al. 1977, *New reduction of the Lick catalog of galaxies*, AJ 82, 249

P. Schneider, *Extragalactic Astronomy and Cosmology*, DOI 10.1007/978-3-642-54083-7_6,

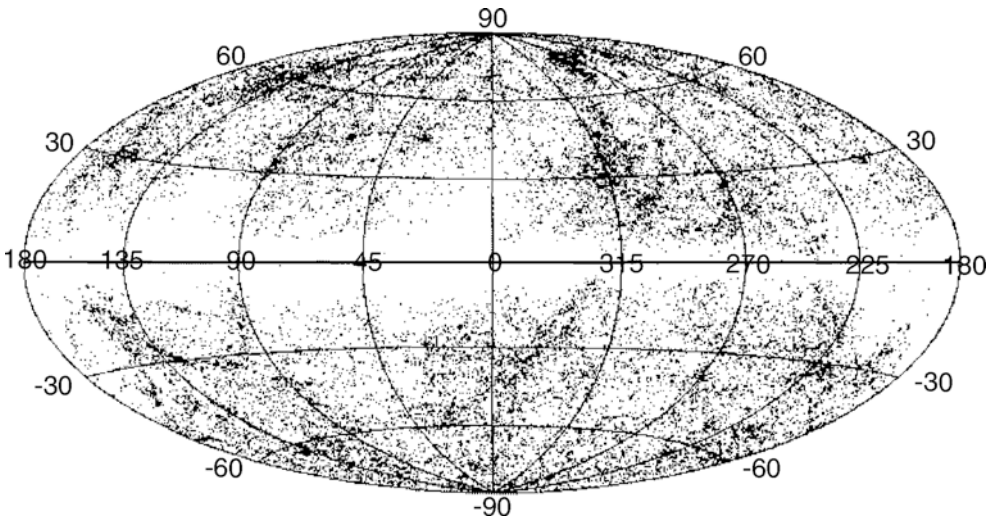

Fig. 6.2 The distribution of all galaxies brighter than $B < 14.5$ on the sphere, plotted in Galactic coordinates. The Zone of Avoidance is clearly seen as the region near the Galactic plane. Source: N.A. Sharp 1986, *The whole-sky distribution of galaxies*, PASP 98, 740, p. 753, Fig. 14

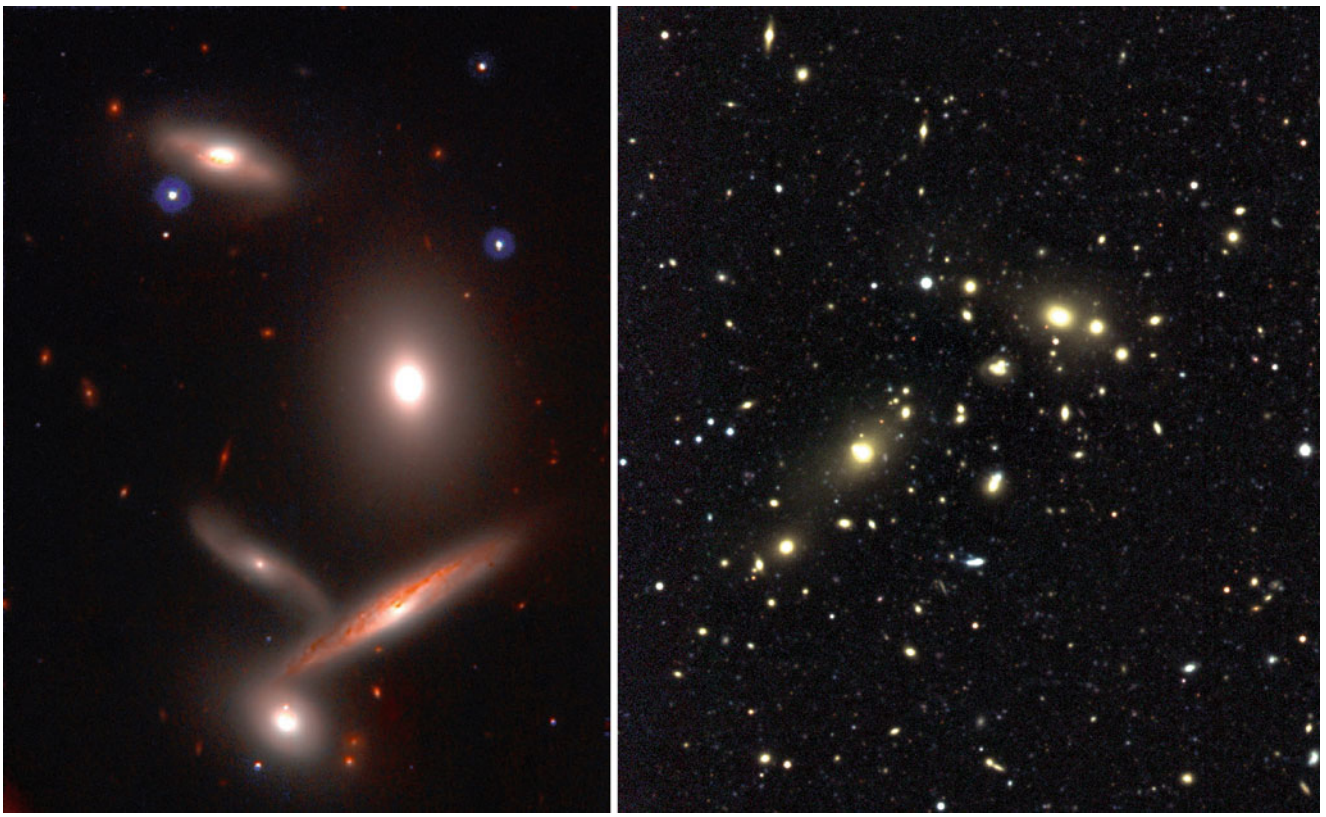

Fig. 6.3 The *left panel* shows HCG40, a compact group of galaxies, observed with the Subaru telescope on Mauna-Kea. The *right panel* displays the cluster of galaxies Cl 0053−37, observed with the WFI at the ESO/MPG 2.2-m telescope. Credits: *Left*: Copyright @ Subaru Telescope, NAOJ. All rights reserved. *Right*: M. Schirmer, European Southern Observatory

impact of the local galaxy density on the morphology and evolution of galaxies.

Outline of this chapter. We will start be discussing the nearest association of galaxies, namely the Local Group, of which the Milky Way is a member. In Sect. 6.2, we describe the identification of galaxy clusters with optical methods, and some of the resulting cluster and group catalogs. The spatial distribution of galaxies in clusters and their dynamics will be studied in Sect. 6.3. We will show that the relative motion of galaxies in clusters implies a much higher cluster mass than can be accounted for by the stars seen in the member galaxies. Whereas not all stars are bound in individual cluster galaxies, but some are distributed throughout the cluster,

forming the intracluster light component, this additional stellar component only constitutes a $\sim 20\,\%$ contribution to the overall stellar mass budget.

The space between the galaxies is filled by a hot gas, detected by its X-ray emission and its impact on the spectrum of the observed cosmic microwave background radiation seen in the direction of clusters. We study this intracluster medium in Sect. 6.4; in particular we show how the properties of the gas can be used for mass determination of clusters. These mass estimates are in good agreement with those obtained from the dynamics of galaxies, reinforcing the conclusion the clusters contain more mass than directly observed, even if the mass of the hot gas is taken into account. The central galaxies of many clusters contain an AGN, whose energy output has a distinct impact on the properties of the hot gas.

In Sect. 6.5 we show that there exist tight relations between the temperature of the hot intracluster gas, its X-ray and optical/near-IR luminosities, the galaxy velocity dispersion and the cluster mass. These scaling relations, analogous to the scaling relations of galaxies, indicate that clusters of the same mass have rather similar properties.

Clusters of galaxies can act as gravitational lenses, giving rise to spectacular imaging phenomena. Those will be discussed in Sect. 6.6, together with a method which allows one to obtain maps of the total matter distribution in clusters. In particular, gravitational lensing yields a third, fully independent method for determining cluster masses. We will find that more than $80\,\%$ of the cluster mass is made of dark matter, only $\sim 3\,\%$ of stars, and some $15\,\%$ of the baryons in the intracluster medium.

The dense environment of groups and clusters may affect the evolution of their member galaxies; we shall therefore discuss the galaxy population of clusters in Sect. 6.7; more generally, we will describe the properties of galaxies in relation to the density of their environment. Finally, we discuss in Sect. 6.8 some evolutionary aspects of the cluster population.

6.1 The Local Group

The Milky Way is a member of the *Local Group*. Within a distance of ~ 1 Mpc around our Galaxy, about 35 galaxies were known at the turn of the Millennium; these 'classical' Local Group members are listed in Table 6.1, and a sketch of their spatial distribution is given in Fig. 6.4. With the Sloan Digital Sky Survey (SDSS; see Sect. 1.4), about 20 additional very faint galaxies in the Local Group have been found. Most of them cannot be detected solely as overdensity of stars on the sky, because their density contrast is too low. However, by filtering the star catalog according to stellar colors and magnitudes, which together allow for the selection of stars from an old population at similar distances, spatial overdensities can be identified. We will return to them in Sect. 7.8.

6.1.1 Phenomenology

The Milky Way (MW), M31 (Andromeda; see Fig. 6.5), and M33 (Fig. 6.6) are the three spiral galaxies in the Local Group, and they are also its most luminous members. The Andromeda galaxy is located at a distance of 770 kpc from us, M33 at about 850 kpc. The Local Group member next in luminosity is the Large Magellanic Cloud (LMC, see Fig. 6.7), which is orbiting around the Milky Way, together with the Small Magellanic Cloud (SMC), at a distance of $\sim$ 50 kpc ($\sim$ 60 kpc, respectively, for the SMC). Both are satellite galaxies of the Milky Way and belong to the class of irregular galaxies (like about 11 other Local Group members). The other members of the Local Group are dwarf galaxies, which are very small and faint (see Fig. 6.8 for three examples). Because of their low luminosity and their low surface brightness, many of the known members of the Local Group were detected only fairly recently. For example, the Antlia galaxy, a dwarf spheroidal galaxy, was found in 1997. Its luminosity is about 10^4 times smaller than that of the Milky Way.

Many of the dwarf galaxies are grouped around the Galaxy or around M31; these are known as *satellite galaxies*. Distributed around the Milky Way are the LMC, the SMC, and about 20 dwarf galaxies, several of them in the so-called *Magellanic Stream* (see Fig. 2.19), a long, extended band of neutral hydrogen which was stripped from the Magellanic Clouds about 2×10^8 yr ago by tidal interactions with the Milky Way. The Magellanic Stream contains about $3 \times 10^8 M_\odot$ of neutral hydrogen.

The spatial distribution of satellite galaxies around the Milky Way shows a pronounced peculiarity, in that the 11 closest satellites form a highly flattened system. These satellites appear to lie essentially in a plane which is oriented perpendicular to the Galactic plane, concentrated along the minor axis of the disk. The satellites around M31 also seem to be distributed in an anisotropic way around their host. In fact, satellite galaxies around spirals seem to be preferentially located near the short axes of the projected light distribution, which has been termed the Holmberg effect, although the statistical significance of this alignment has been questioned, in particular in recent years. We will come back to this issue in Sect. 7.8.

In fact, the Local Group is not a group of galaxies in the sense of this chapter; its spatial extent is too large for a group of this mass, and it is not dynamically relaxed. The bimodal distribution of galaxies in the Local Group seen in Fig. 6.4 instead suggests that two small galaxy groups—one centered

Table 6.1 'Classical' members of the Local Group

Galaxy	Type	M_B	RA/dec.	ℓ,b	D(kpc)	v_r (km/s)
Milky Way	Sbc I-II	−20.0	1830 − 30	0, 0	8	0
LMC	Ir III-IV	−18.5	0524 − 60	280, −33	50	270
SMC	Ir IV-V	−17.1	0051 − 73	303, −44	63	163
Sgr I	dSph?		1856 − 30	6, −14	20	140
Fornax	dE0	−12.0	0237 − 34	237,−65	138	55
Sculptor Dwarf	dSph	−9.8	0057 − 33	286, −84	88	110
Leo I	dSph	−11.9	1005 + 12	226, +49	790	168
Leo II	dSph	−10.1	1110 + 22	220, +67	205	90
Ursa Minor	dSph	−8.9	1508 + 67	105, +45	69	−209
Draco	dSph	−9.4	1719 + 58	86, +35	79	−281
Carina	dSph	−9.4	0640 − 50	260, −22	94	229
Sextans	dSph	−9.5	1010 − 01	243, +42	86	230
M31	Sb I-II	−21.2	0040 + 41	121, −22	770	−297
M32 = NGC 221	dE2	−16.5	0039 + 40	121, −22	730	−200
M110 = NGC 205	dE5p	−16.4	0037 + 41	121, −21	730	−239
NGC 185	dE3p	−15.6	0036 + 48	121, −14	620	−202
NGC 147	dE5	−15.1	0030 + 48	120, −14	755	−193
And I	dSph	−11.8	0043 + 37	122, −25	790	–
And II	dSph	−11.8	0113 + 33	129, −29	680	–
And III	dSph	−10.2	0032 + 36	119, −26	760	–
Cas = And VII	dSph		2326 + 50	109, −09	690	–
Peg = DDO 216	dIr/dSph	−12.9	2328 + 14	94, −43	760	–
Peg II = And VI	dSph	−11.3	2351 + 24	106, −36	775	–
LGS 3	dIr/dSph	−9.8	0101 + 21	126, −41	620	−277
M33	Sc II-III	−18.9	0131 + 30	134, −31	850	−179
NGC 6822	dIr IV-V	−16.0	1942 − 15	025, −18	500	−57
IC 1613	dIr V	−15.3	0102 + 01	130, −60	715	−234
Sagittarius	dIr V	−12.0	1927 − 17	21, +16	1060	−79
WLM	dIr IV-V	−14.4	2359 − 15	76, −74	945	−116
IC 10	dIr IV	−16.0	0017 + 59	119, −03	660	−344
DDO 210, Aqr	dIr/dSph	−10.9	2044 − 13	34, −31	950	−137
Phoenix Dwarf	dIr/dSph	−9.8	0149 − 44	272, 68	405	56
Tucana	dSph	−9.6	2241 − 64	323, −48	870	–
Leo A = DDO 69	dIr V	−11.7	0959 + 30	196, 52	800	–
Cetus Dwarf	dSph	−10.1	0026 − 11	101, −72	775	–

Listed are the name of the galaxy, its morphological type, the absolute B-band magnitude, its position on the sphere in both right ascension/declination and in Galactic coordinates, its distance from the Sun, and its radial velocity. A sketch of the spatial configuration is displayed in Fig. 6.4

on M31, the other one centered on the Milky Way—are in a process of merging.

6.1.2 Mass estimate

We will present a simple mass estimate of the Local Group, from which we will find that it is considerably more massive than one would conclude from the observed luminosity of the associated galaxies.

M31 is one of the very few galaxies with a blueshifted spectrum. Hence, Andromeda and the Milky Way are approaching each other, at a relative velocity of $v \approx 120\,\mathrm{km/s}$. This value results from the velocity of M31 relative to the Sun of $v \approx 300\,\mathrm{km/s}$, and from the motion of the Sun around the Galactic center. Together with the distance to M31 of $D \sim 770\,\mathrm{kpc}$, we conclude that both galaxies will collide on a time-scale of $\sim 6 \times 10^9\,\mathrm{yr}$, if we disregard the transverse component of the relative velocity. From measurements of the proper motion of M31, one finds that its transverse velocity is small—thus a collision with the Milky Way will almost certainly occur.

The luminosity of the Local Group is dominated by the Milky Way and by M31, which together produce about 90 % of the total luminosity. If the mass density follows the light distribution, the dynamics of the Local Group should also

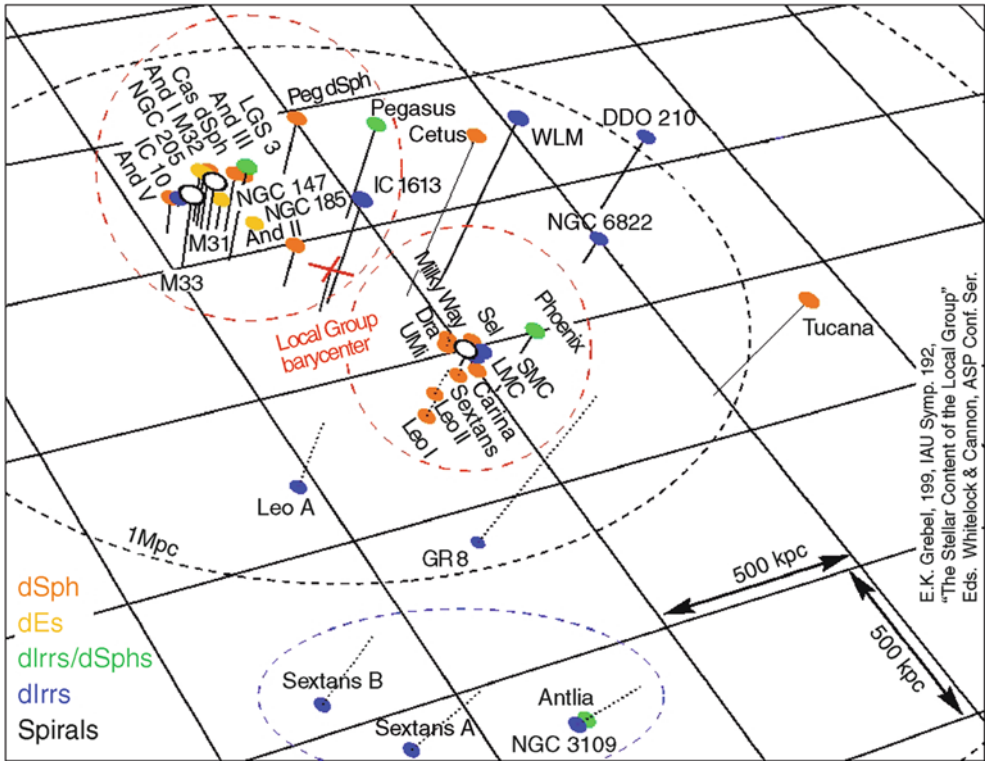

Fig. 6.4 Schematic distribution of galaxies in the Local Group, with the Milky Way at the center of the figure Shown are only the 'classical' Local Group members which were known before 2000; most of the newly found galaxies in the Local Group are ultra-faint dwarfs. Credit: E. Grebel, Astronomical Institute, University of Basel, Switzerland

be dominated by these two galaxies. Therefore, one can try to estimate the mass of the two galaxies from their relative motion, and with this also the mass of the Local Group.

In the early phases of the Universe, the Galaxy and M31 were close together and both took part in the Hubble expansion. By their mutual gravitational attraction, their relative motion was decelerated until it came to a halt—at a time $t_{\max}$ at which the two galaxies had their maximum separation $r_{\max}$ from each other. From this time on, they have been moving towards each other. The relative velocity $v(t)$ and the separation $r(t)$ follow from the conservation of energy,

$$\frac{v^2}{2} = \frac{GM}{r} - C \ , \tag{6.1}$$

where M is the sum of the masses of the Milky Way and M31, and C is an integration constant, related to the total energy of the M31/MW-system. This constant can be determined by considering (6.1) at the time of maximum separation, when $r = r_{\max}$ and $v = 0$. With this,

$$C = \frac{GM}{r_{\max}}$$

follows immediately. Since $v = \mathrm{d}r/\mathrm{d}t$, (6.1) is a differential equation for $r(t)$,

$$\frac{1}{2}\left(\frac{\mathrm{d}r}{\mathrm{d}t}\right)^2 = GM\left(\frac{1}{r} - \frac{1}{r_{\max}}\right) \ .$$

It can be solved using the initial condition $r = 0$ at $t = 0$. For our purpose, an approximate consideration is sufficient. Solving the equation for $\mathrm{d}t$ we obtain, by integration, a relation between $r_{\max}$ and $t_{\max}$,

$$t_{\max} = \int_0^{t_{\max}} \mathrm{d}t = \int_0^{r_{\max}} \frac{\mathrm{d}r}{\sqrt{2GM}\sqrt{1/r - 1/r_{\max}}}$$
$$= \frac{\pi\, r_{\max}^{3/2}}{2\sqrt{2GM}} \ . \tag{6.2}$$

Since the differential equation is symmetric with respect to changing $v \to -v$, the collision will happen at $2t_{\max}$. Estimating the time from today to the collision, by assuming the relative velocity to be constant during this time, then yields $r(t_0)/v(t_0) = D/v = 770\,\mathrm{kpc}/(120\,\mathrm{km/s})$, and one obtains $2t_{\max} \approx t_0 + D/v$, or

$$t_{\max} \approx \frac{t_0}{2} + \frac{D}{2v} \approx 10^{10}\,\mathrm{yr} \ , \tag{6.3}$$

where $t_0 \approx 14 \times 10^9\,\mathrm{yr}$ is the current age of the Universe. Hence, together with (6.2) this yields

$$\frac{v^2}{2} = \frac{GM}{r} - \frac{GM}{r_{\max}} = \frac{GM}{r} - \frac{1}{2}\left(\frac{\pi GM}{t_{\max}}\right)^{2/3} \ . \tag{6.4}$$

Now by inserting the values $r(t_0) = D$ and $v = v(t_0)$, we obtain the mass M,

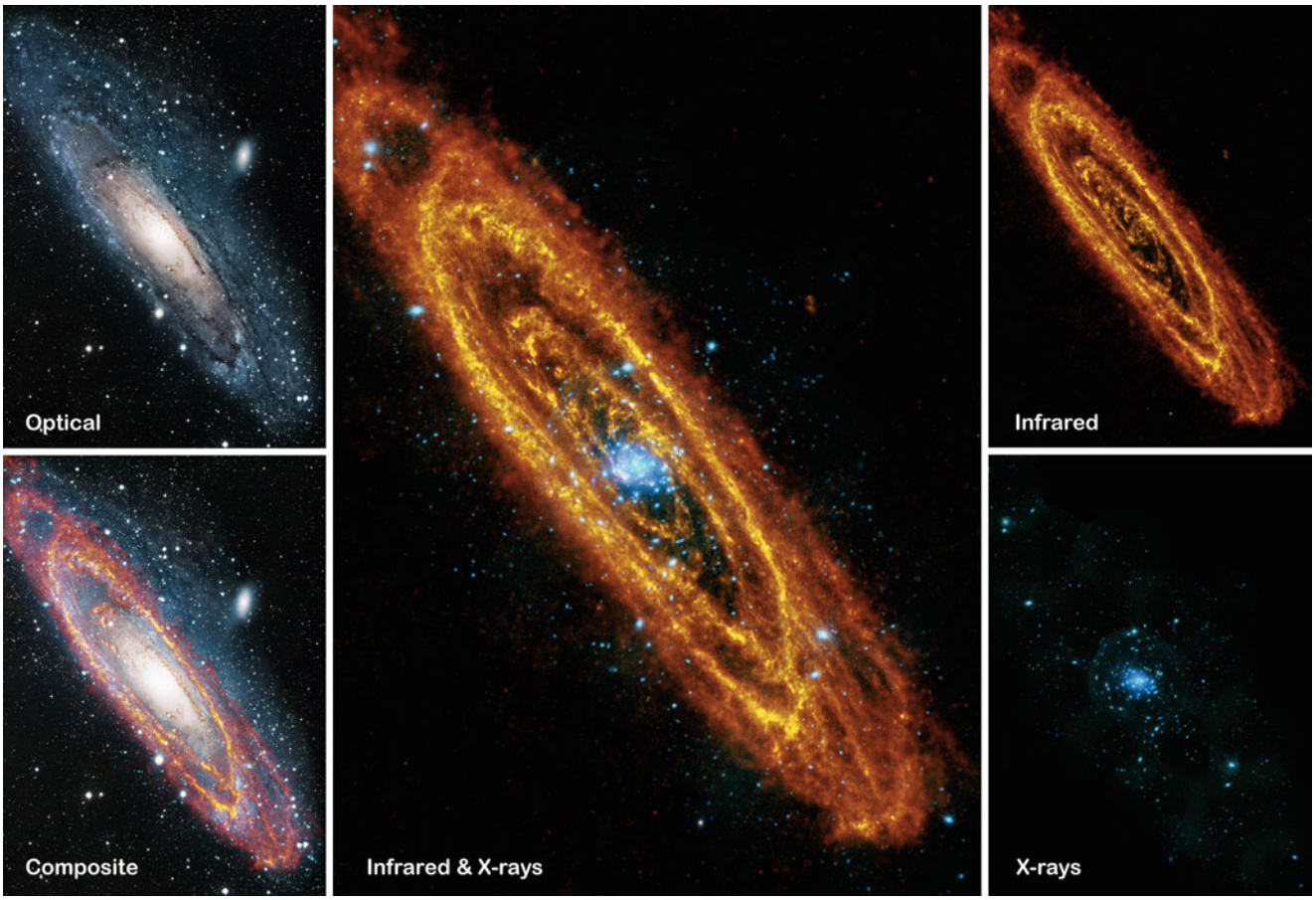

Fig. 6.5 M31, the Andromeda galaxy, seen in different wavelengths. All images show a region of $1.5° \times 2°$. Compared to the optical image (*top left*) which shows the stellar distribution of the galaxy, the far-infrared emission shown on the *top right* displays predominantly the dust component of the interstellar medium. Heated by young massive stars, the dust re-radiates the absorbed energy at long wavelengths, here shown with a 250 μm exposure taken with the Herschel Observatory. The X-ray image (*bottom right*), taken with XMM-Newton, mainly displays the distribution of X-ray binaries and supernova remnants; in particular the former are much more concentrated towards the central parts of the galaxy. The two composite images in the *center* and *bottom left* compare the distributions of the various components of M31. Credit & Copyright: infrared: ESA/Herschel/PACS/SPIRE/J. Fritz, U. Gent; X-ray: ESA/XMM-Newton/EPIC/W. Pietsch, MPE; optical: R. Gendler

$$M \sim 3 \times 10^{12} M_\odot \ . \tag{6.5}$$

This mass is much larger than the mass of the two galaxies as observed in stars and gas. The mass estimate yields a mass-to-light ratio for the Local Group of $M/L \sim 70\, M_\odot/L_\odot$, much larger than that of any known stellar population. This is therefore another indication of the presence of dark matter because we can see only about 5 % of the estimated mass in the Milky Way and Andromeda. Another mass estimate follows from the kinematics of the Magellanic Stream, which also yields $M/L \gtrsim 80 M_\odot/L_\odot$.

6.1.3 Other components of the Local Group

Tidal streams. One of the most interesting galaxies in the Local Group is the *Sagittarius dwarf galaxy* which was only discovered in 1994. Since it is located in the direction of the Galactic bulge, it is barely visible on optical images, if at all, as an overdensity of stars. Furthermore, it has a very low surface brightness. It was discovered in an analysis of stellar kinematics in the direction of the bulge, in which a coherent group of stars was found with a velocity distinctly different from that of bulge stars. In addition, the stars belonging to this overdensity have a much lower metallicity, reflected in their colors. The Sagittarius dwarf galaxy is located close to the Galactic plane, at a distance of about 16 kpc from the Galactic center and nearly in the direct extension of our line-of-sight to the GC. This proximity implies that it must be experiencing strong tidal gravitational forces on its orbit around the Milky Way; over the course of time, these will have the effect that the Sagittarius dwarf galaxy will be slowly disrupted. In fact, in recent years a relatively narrow band of stars was found around the Milky Way. These stars are located along the orbit of the Sagittarius galaxy (see Fig. 2.18). Their chemical composition supports the

Fig. 6.6 Multi-band (u,g,r) composite image of the Triangulum Galaxy (M33), a Local Group spiral with an estimated distance of $\sim$ 850 kpc. With its visible diameter of $\sim$ 15 kpc, it is the third largest galaxy of the Local Group; its stellar mass is about 1/10 that of the Milky Way. Observations of water masers in this galaxy enabled the measurement of its proper motion, indicating that it is heading towards M31. The bluish emission is due to regions of active star formation; indeed, the bright region near the top-right of the images is one of the most luminous HII regions known. This is the first image taken with the wide-field camera of the new 2-m Fraunhofer telescope on the Wendelstein Observatory and covers 30′ on a side. Credit: Wendelstein Observatory, Universitätssternwarte der Ludwig-Maximilians-Universität München

interpretation that they are stars stripped from the Sagittarius dwarf galaxy by tidal forces. In addition, globular clusters were identified which presumably once belonged to the Sagittarius dwarf galaxy, but which were also removed from it by tidal forces and are now part of the globular cluster population in the Galactic halo. Indeed, more tidal streams have been discovered recently, both in the Milky Way and in Andromeda, as well as in other neighboring galaxies.

The neighborhood of the Local Group. The Local Group is indeed a concentration of galaxies: while it contains more than 50 members within $\sim$ 1 Mpc, the next neighboring galaxies are found only in the Sculptor Group, which contains about six members[1] and is located at a distance of $D \sim 1.8$ Mpc. The next galaxy group after this is the M81-group of $\sim$ 8 galaxies at $D \sim 3.1$ Mpc, the two most prominent galaxies of which are displayed in Fig. 6.9.

[1]Of course, the numbers quoted here are those of currently known galaxies. Dwarf galaxies like Sagittarius would be very difficult to detect at the distances of these groups.

The other nearby associations of galaxies within 10 Mpc from us shall also be mentioned: the Centaurus group with 17 members and $D \sim 3.5$ Mpc, the M101-group with 5 members and $D \sim 7.7$ Mpc, the M66- and M96-group with together 10 members located at $D \sim 9.4$ Mpc, and the NGC 1023-group with 6 members at $D = 9.6$ Mpc.

Most galaxies are members of a group. Many more dwarf galaxies exist than luminous galaxies, and dwarf galaxies are located preferentially in the vicinity of larger galaxies. Some members of the Local Group are so under-luminous that they would hardly be observable outside the Local Group.

One large concentration of galaxies was already known in the eighteenth century (W. Herschel)—the *Virgo cluster*. Its galaxies extend over a region of about $10° \times 10°$ in the sky, and its distance is $D \sim 16$ Mpc. The Virgo cluster consists of about 250 large galaxies and more than 2000 smaller ones; the central galaxy of the cluster is the radio galaxy M87 (Fig. 1.11). In the classification scheme of galaxy clusters, Virgo is considered an irregular cluster. The closest regular massive galaxy cluster is the *Coma cluster* (see Fig. 1.17), at a distance of about $D \sim 90$ Mpc.

6.2 Optical cluster searches

6.2.1 The Abell catalog

George Abell compiled a catalog of galaxy clusters, published in 1958, in which he identified regions in the sky that show an overdensity of galaxies. This identification was performed by eye on photoplates from the *Palomar Observatory Sky Survey* (POSS), a photographic atlas of the Northern ($\delta > -30°$) sky (see Sect. 1.4). He omitted the Galactic disk region because the observation of galaxies is considerably more problematic there, due to extinction and the high stellar density (see also Fig. 6.2).

Abell's criteria and his catalog. The criteria Abell applied for the identification of clusters refer to an overdensity of galaxies within a specified solid angle. According to these criteria, a cluster contains $\geq$50 galaxies in a magnitude interval $m_3 \leq m \leq m_3 + 2$, where m_3 is the apparent magnitude of the third brightest galaxy in the cluster.[2] These galaxies must be located within a circle of angular radius

$$\theta_A = \frac{1'.7}{z}\,, \tag{6.6}$$

[2]The reason for choosing the third brightest galaxy is that the luminosity of the brightest galaxy may vary considerably among clusters. Even more important is the fact that there is a finite probability for the brightest galaxy in a sky region under consideration to not belong to the cluster, but to be located at some smaller distance from us.

Fig. 6.7 An image of the Large Magellanic Cloud (LMC), taken with the CTIO 4-m telescope. Credit & Copyright: AURA/NOAO/NSF

where z is the estimated redshift. The latter is estimated by the assumption that the luminosity of the tenth brightest galaxy in a cluster is the same for all clusters. A calibration of this distance estimate is performed on clusters of known redshift. θ_{A} is called the *Abell radius* of a cluster, and corresponds to a physical radius of $R_{\mathrm{A}} \approx 1.5h^{-1}\,\mathrm{Mpc}$.

The so-determined redshift should be within the range $0.02 \leq z \leq 0.2$ for the selection of Abell clusters. The lower limit is chosen such that a cluster can be found on a single POSS photoplate ($\sim 6° \times 6°$) and does not extend over several plates, which would make the search more difficult, e.g., because the photographic sensitivity may differ for individual plates. The upper redshift bound is chosen due to the sensitivity limit of the photoplates.

The Abell catalog contains 1682 clusters which all fulfill the above criteria. In addition, it lists 1030 clusters that were found in the search, but which do not fulfill all of the criteria (most of these contain between 30 and 49 galaxies). An extension of the catalog to the Southern sky was published by Abell, Corwin & Olowin in 1989. This ACO catalog contains 4076 clusters, including the members of the original catalog. Another important catalog of galaxy clusters is the Zwicky catalog (1961–1968), which contains more clusters, but which is considered less reliable, since the applied selection criteria resulted in more spurious cluster candidates than is the case for the Abell catalog.

Problems in the optical search for clusters. The selection of galaxy clusters from an overdensity of galaxies on the sphere is not without problems, in particular if these catalogs are to be used for statistical purposes. An ideal catalog ought to fulfill two criteria: first it should be complete, in the sense that all objects which fulfill the selection criteria are contained in the catalog. Second it should be pure (often also called 'reliable'), i.e., it should not contain any objects that do not belong in the catalog because they do not fulfill the criteria (so-called false positives). The Abell catalog is neither complete, nor is it pure. We will briefly discuss why completeness and reliability cannot be expected in a catalog compiled in this way.

A galaxy cluster is a three-dimensional object, whereas galaxy counts on images are necessarily based on the projection of galaxy positions onto the sky. Therefore, projection effects are inevitable. Random overdensities on the sphere caused by line-of-sight projection may easily be classified as clusters. The reverse effect is likewise possible: due to fluctuations in the number density of foreground galaxies, a cluster at high redshift may be classified as an insignificant fluctuation—and thus remain undiscovered.

Of course, not all members of a cluster classified as such are in fact galaxies in the cluster, as here projection effects also play an important role. Furthermore, the redshift estimate is relatively coarse. In the meantime, spectroscopic analyses have been performed for many of the Abell clusters, and it has been found that Abell's redshift estimates have an error of about 30 %—they are surprisingly accurate, considering the coarseness of his assumptions.

The Abell catalog is based on visual inspection of photographic plates. It is therefore partly subjective. Today, the Abell criteria can be applied to digitized images in an

Fig. 6.8 *Upper left*: NGC 6822, also known as Barnard's Galaxy, is one of the dwarf elliptical galaxies of the Local Group, located at a distance of 500 kpc from the Milky Way. This color composite image covers a region of 34′ on the side, and was taken with the WFI@ESO/MPG 2.2 m telescope on La Silla. The reddish nebulae in the image indicate regions of active star formation. *Upper right*: The Fornax dwarf spheroidal galaxy is a satellite of the Milky Way, at a distance of 140 kpc. The image size is about $17' \times 13'$, and was extracted from the Digitized Sky Survey II. *Bottom*: The Antlia dwarf galaxy lies at a distance of 1.3 Mpc, at the edge of the Local Group. This color-composite HST images covers $3'.2 \times 1'.5$. Credit: *Top left*: ESO; *Top right*: ESO/Digitized Sky Survey 2; *Bottom*: ESA/NASA

objective manner, using automated searches. From these, it was found that the results are not much different. The visual search thus was performed with great care and has to be recognized as a great accomplishment. For this reason, and in spite of the potential problems discussed above, the Abell and the ACO catalogs are still frequently used.

The clusters in the catalog are ordered by right ascension and are numbered. For example, Abell 851 is the 851st entry in the catalog, also denoted as A851. With a redshift of $z = 0.41$, A851 is the most distant Abell cluster.

Abell classes. The Abell and ACO catalogs divide clusters into so-called richness and distance classes. Table 6.2 lists the criteria for the richness classes, while Table 6.3 lists those for the distance classes, with the number of clusters in each class referring to the original Abell catalog (i.e., without the ACO extension).

There are six *richness classes*, denoted from 0 to 5, according to the number of cluster member galaxies. Richness class 0 contains between 30 and 49 members and therefore does not belong to the cluster catalog proper. One can see from Table 6.2 that the number of clusters rapidly decreases with increasing richness class, so only very few clusters exist with a very large number of cluster galaxies. As a reminder, the region of the sky from where the Abell clusters were detected is about half of the total sphere. Thus, only a few very rich clusters do indeed exist (at redshift $\lesssim 0.2$). The only cluster with richness class 5 is A 665.

The subdivision into six *distance classes* is based on the apparent magnitude of the tenth brightest galaxy, in accordance with the redshift estimate for the cluster. Hence, the distance class provides a coarse measure of the distance.

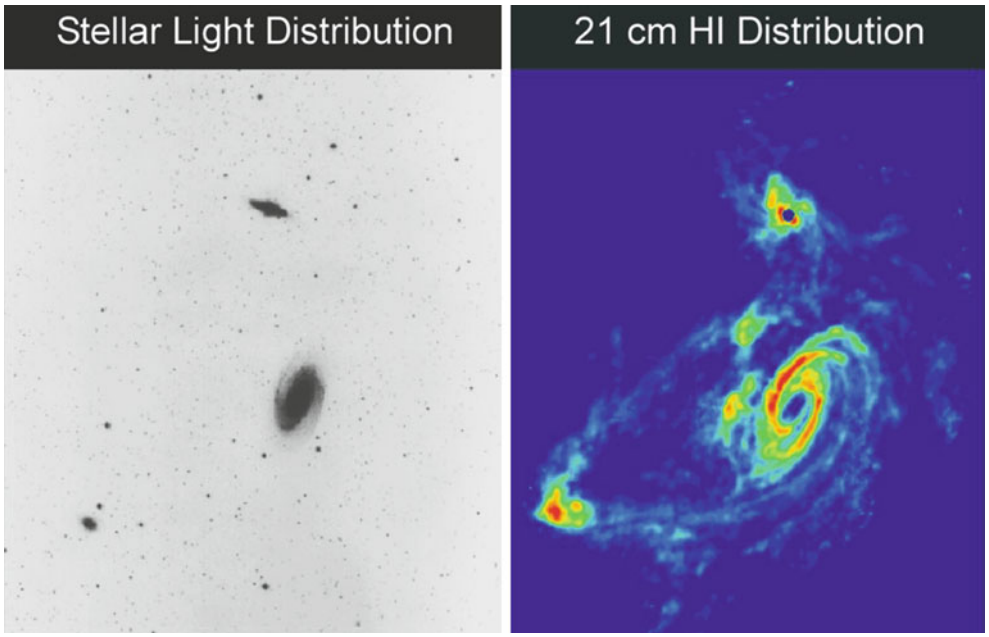

Fig. 6.9 *The left panel* shows an optical image of the galaxies M81 (*bottom*) and M82 (*top*), two members of the M81-group, about 3.1 Mpc away (see also Fig. 1.3 for a detailed view of M82). These two galaxies are moving around each other, and the gravitational interaction taking place, as clearly seen in the distribution of atomic hydrogen (*right panel*) which has been stripped off the galaxies due to gravitational interactions, may be the reason for the violent star formation in M82. M82 is an archetypical starburst galaxy. Credit: Image courtesy of National Radio Astronomy Observatory/AUI

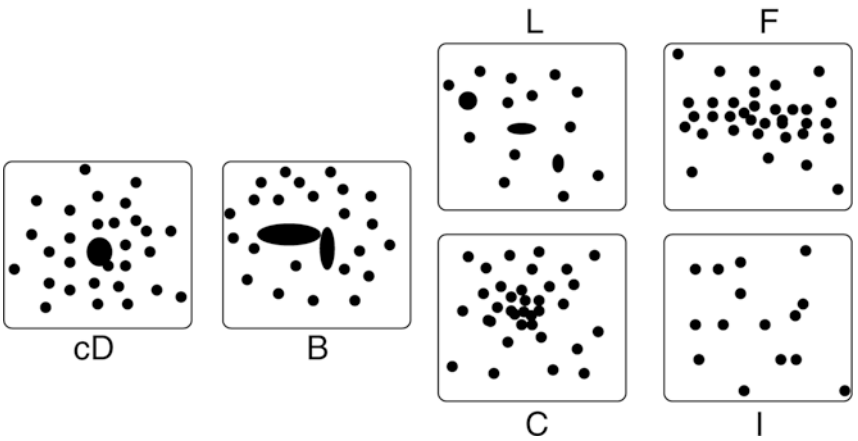

Fig. 6.10 Rough morphological classification of clusters by Rood & Sastry: cDs are those which are dominated by a central cD galaxy, Bs contain a pair of bright galaxies in the center. Ls are clusters with a nearly linear alignment of the dominant galaxies, Cs have a single core of galaxies, Fs are clusters with an oblate galaxy distribution, and Is are clusters with an irregular distribution. This classification has the more regular clusters at the *left* and irregular clusters at the *right*

6.2.2 Morphological classification of clusters

Clusters are also classified by the morphology of their galaxy distribution. Several classifications are used, one of which is displayed in Fig. 6.10. Since this is a description of the visual impression of the galaxy distribution, the exact class of a cluster is not of great interest. However, a rough classification can provide an idea of the state of a cluster, i.e., whether it is currently in dynamical equilibrium or whether it has been heavily disturbed by a merger process with another cluster. Therefore, one distinguishes in particular between regular and irregular clusters, and also those which are intermediate; the transition between classes is of course continuous. Regular clusters are 'compact' whereas, in contrast, irregular clusters are 'open' (Zwicky's classification criteria).

This morphological classification indeed points at physical differences between clusters, as correlations between morphology and other properties of galaxy clusters show. For example, it is found that regular clusters are completely dominated by early-type galaxies, whereas irregular clusters have a fraction of spirals nearly as large as in the general distribution of field galaxies. Very often, regular clusters are dominated by a cD galaxy at the center, and their central galaxy density is very high. In contrast, irregular clusters are significantly less dense in the center. Irregular clusters often show strong substructure, which is rarely found in regular clusters. Furthermore, regular clusters have a high richness, whereas irregular clusters have fewer cluster members. To summarize, regular clusters can be said to be in a relaxed state, whereas irregular clusters are still in the process of evolution.

6.2.3 Galaxy groups

Accumulations of galaxies that do not satisfy Abell's criteria are in most cases galaxy groups. Hence, groups are the continuation of clusters towards fewer member galaxies and are therefore presumably of lower mass, lower velocity dispersion, and smaller extent. The distinction between groups and clusters is at least partially arbitrary. It was defined by Abell mainly to be not too heavily affected by projection effects in the identification of clusters. Groups are of course more difficult to detect, since the overdensity criterion for them is more sensitive to projection effects by foreground and background galaxies than for clusters.

Table 6.2 Definition of Abell's richness classes

Richness class R	N	Number in Abell's catalog
(0)	(30–49)	($\geq$ 1000)
1	50–79	1224
2	80–129	383
3	130–199	68
4	200–299	6
5	$\geq$ 300	1

N is the number of cluster galaxies with magnitudes between m_3 and $m_3 + 2$ inside the Abell radius (6.6), where m_3 is the brightness of the third brightest cluster galaxy

Table 6.3 Definition of Abell's distance classes

Distance class	m_{10}	Estimated average redshift	Number in Abell's catalog with $R \geq 1$
1	13.3–14.0	0.0283	9
2	14.1–14.8	0.0400	2
3	14.9–15.6	0.0577	33
4	15.7–16.4	0.0787	60
5	16.5–17.2	0.131	657
6	17.3–18.0	0.198	921

m_{10} is the magnitude of the tenth brightest cluster galaxy

A special class of groups are the *compact groups*, assemblies of (in most cases, few) galaxies with very small projected separations. The best known examples for compact groups are Stephan's Quintet and Seyfert's Sextet (see Fig. 6.11). In 1982, a catalog of 100 compact groups (Hickson Compact Groups, HCGs) was published, where a group consists of four or more bright members. These were also selected on POSS photoplates, again solely by an overdensity criterion. The median redshift of the HCGs is about $z = 0.03$. Further examples of optical images of HCGs are given in Figs. 6.3 and 1.20.

Follow-up spectroscopic studies of the HCGs have verified that 92 of them have at least three galaxies with conforming redshifts, defined such that the corresponding recession velocities lie within 1000 km/s of the median velocity of group members. Of course, the similarity in redshift does not necessarily imply that these groups form a gravitationally bound and relaxed system. For instance, the galaxies could be tracers of an overdense structure which we happen to view from a direction where the galaxies are projected near each other on the sky. However, more than 40 % of the galaxies in HCGs show evidence of interactions, indicating that these galaxies have near neighbors in three-dimensional space. Furthermore, about three quarters of HCGs with four or more member galaxies show extended X-ray emission, most likely coming from intra-group hot gas, providing additional evidence for the presence of a common gravitational potential well (see Sect. 6.4). Compared to clusters, the intergalactic gas in groups has a lower temperature and, possibly, lower metallicity.

6.2.4 Modern optical cluster catalogs

The subjectivity of selecting overdensities on images by eye can of course be overcome by using digital (or digitized) astronomical images and employing algorithms to apply criteria to the data which define an overdensity, or a cluster, respectively. This approach solves one of the aforementioned problems in optical cluster searches. The other problem—namely projection effects—can be overcome if an additional distance measure for potential member galaxies can be applied.[3] There are two ways how such a distance indicator can be obtained: one either uses large spectroscopic catalogs of galaxies, such as the SDSS, or, as will be discussed next, one can employ the colors of early-type galaxies.

Color-magnitude diagram. We mentioned before that a large fraction of galaxies in clusters are early-type galaxies. Furthermore, we saw in Sect. 3.6 that early-type galaxies have rather uniform colors. Indeed, plotting the color of cluster galaxies versus their magnitude, one finds a very well-defined, nearly horizontal sequence (Fig. 6.12). This red cluster sequence (RCS) is populated by the early-type galaxies in the cluster.

The scatter of early-type galaxies around this sequence is very small, which suggests that all early-type galaxies in a cluster have nearly the same color, only weakly depending on luminosity. The small slope seen in Fig. 6.12 is mainly due to the fact that more massive ellipticals have a somewhat higher metallicity, rendering the stellar emission slightly redder. Even more surprising is the fact that the color-magnitude diagrams of different clusters at the same redshift define a very similar red cluster sequence: early-type cluster galaxies with the same redshift and luminosity have virtually the same color. Comparing the red sequences of clusters at different redshifts, one finds that the sequence of cluster galaxies is redder the higher the redshift is. This effect is caused by the redshift of the galaxies, which shift their spectral energy distribution towards longer wavelengths. Hence, by

[3] There are also other methods that have been used to construct cluster catalogs, which run under name of 'matched filter' techniques. They assume that galaxies are not only a collection of galaxies, but that the galaxy overdensity has certain properties. For example, the number density of cluster galaxies is expected to have a particular radial density profile and their distribution in luminosity should approximately follow a Schechter-type luminosity function. Applying these criteria to galaxy overdensities leads to cleaner cluster selection than a pure overdensity criterion. As a drawback, these criteria are more likely to select regular clusters than irregular ones, due to the assumed density profile.

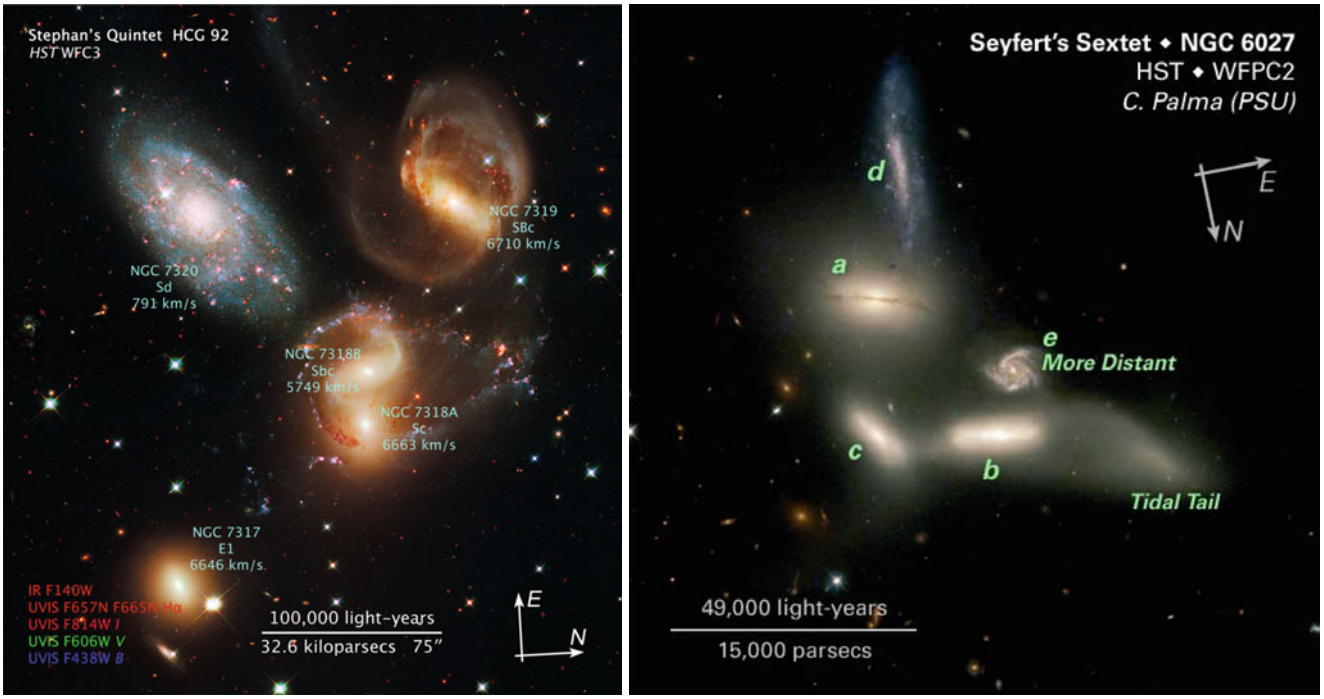

Fig. 6.11 *Left panel*: Stephan's Quintet, also known as Hickson Compact Group 92, is a very dense accumulation of galaxies with a diameter of about 80 kpc. The galaxy at the upper left (NGC 7320) is not a member of the group: its redshift indicates that it has a much smaller distance from us than the other four galaxies; in fact, it is close enough to us for HST being able to resolve individual stars. This galaxy has only $\sim 2\,\%$ of the luminosity of the other galaxies shown, i.e., it is an actively star-forming dwarf galaxy, as is also seen by its much bluer color compared to the other galaxies in the field. The remaining three spiral galaxies of the group show clear signs of interactions—distorted spiral arms and tidal tails. The strong interaction of the galaxy pair in the middle of the image gives rise to a strong burst of star formation. The elliptical galaxy at the bottom left appears to be less affected by galaxy interactions. The image is a color composite of optical and near-IR images, as well as a narrow band image at the Hα wavelength, all taken with the WFC3 instrument onboard HST. *Right panel*: Seyfert's Sextet, an apparent accumulation of six galaxies located very close together on the sphere. Only four of the galaxies (a–d) in fact belong to the group; the spiral galaxy (e) is located at significantly larger distance. Another object originally classified as a galaxy is no galaxy but instead a tidal tail that was ejected in tidal interactions of galaxies in the group. Credit: *Left*: NASA, ESA, and the Hubble SM4 ERO Team; *Right*: NASA, J. English (U. Manitoba), C. Palma, S. Hunsberger, S. Zonak, J. Charlton, S. Gallagher (PSU), and L. Frattare (STScI)

keeping the observed filter bands constant, the colors change as a function of redshift. In fact, the red cluster sequence is so precisely characterized that, from the color-magnitude diagram of a cluster alone, its redshift can be estimated with very high accuracy, provided the photometric calibration is sufficiently good. Furthermore, the accuracy of this estimated redshift strongly depends on the choice of the filters between which the color is measured. Since the most prominent spectral feature of early-type galaxies is the 4000 Å-break, the redshift is estimated best if this rest-frame wavelength, redshifted to $4000\,(1+z)$ Å, is well covered by the photometric bands employed.

This well-defined red cluster sequence is of crucial importance for our understanding of the evolution of galaxies. We know from Sect. 3.5 that the composition of a stellar population depends on the mass spectrum at its birth (the initial mass function, IMF) and on its age: the older a population is, the redder it becomes. The fact that cluster galaxies at the same redshift all have roughly the same color indicates that their stellar populations have very similar ages. However, the only age that is singled out is the age of the Universe itself. In fact, the color of cluster galaxies is compatible with their stellar populations being roughly the same age as the Universe at that particular redshift. This also provides an explanation for why the red cluster sequence is shifted towards *intrinsically* bluer colors at higher redshifts—there, the age of the Universe was smaller, and thus the stellar population was younger. This effect is of particular importance at high redshifts.

The RCS Survey. The cluster red sequence method was used in several multi-band imaging surveys for the detection of clusters. In fact, one of the large imaging surveys carried out with the CFHT was the RCS survey, with its main purpose to detect clusters out to large redshifts. It covered $100\,\mathrm{deg}^2$ in two filters, and yielded more than 1000 cluster and group candidates, out to redshifts larger than unity. As a follow-up, the RCS II survey covers $900\,\mathrm{deg}^2$ in three filters, and aims at detecting some 10^4 clusters out to $z \sim 1$.

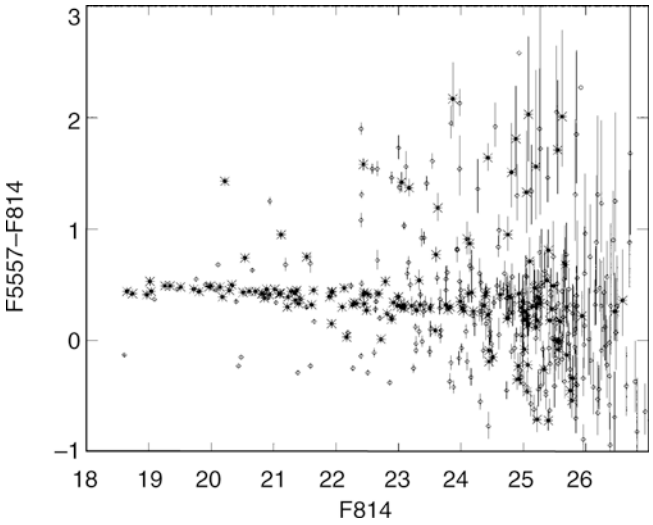

Fig. 6.12 Color-magnitude diagram of the cluster of galaxies Abell 2390, observed with the HST. *Star symbols* represent early-type galaxies, identified by their morphology, while *diamonds* denote other galaxies in the field. The red cluster sequence is clearly visible. Note that, due to projection effects, not all galaxies shown here are indeed cluster members; some of them are foreground or background galaxies. Source: M. Gladders & H. Yee 2000, *A New Method For Galaxy Cluster Detection. I. The Algorithm*, AJ 120, 2148, p. 2150, Fig. 1. ©AAS. Reproduced with permission

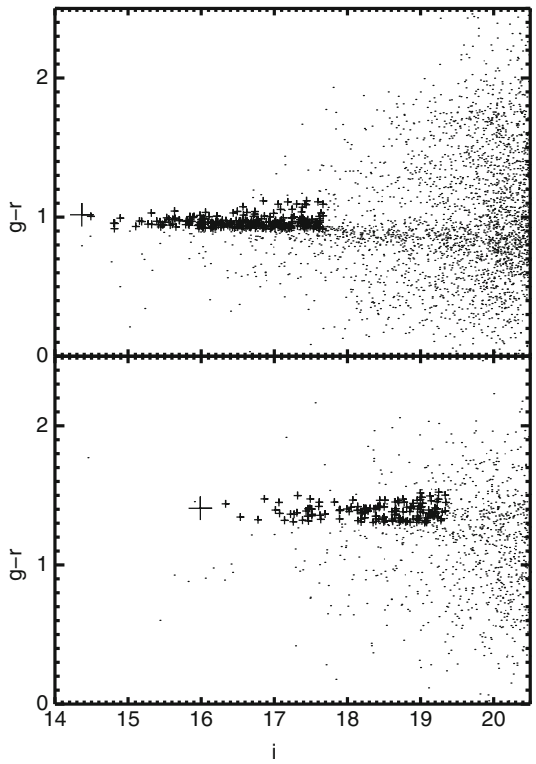

Fig. 6.13 Example of two clusters found by the maxBCG method. Shown are the color-magnitude relations for galaxies in the field of Abell 2142 at $z = 0.092$ (*top*) and Abell 1682 at $z = 0.23$ (*bottom*). In both cases, all galaxies within $2h^{-1}$ Mpc of the BCG are plotted as *small dots*. The BCG itself is denoted by a *big cross*, being the most luminous of the cluster members, whereas the smaller crosses show galaxies with $L \geq 0.4L^*$ whose colors lie within $\pm 2\sigma$ of the red sequence, which is 0.05 and 0.06 for the $g - r$ and $r - i$, respectively. If they lie closer that the estimated R_{200} from the BCG, they are considered to be cluster members. We note that the red sequence has almost zero slope in the color shown here. Although these two clusters were known before, their rediscovery provides one of the tests of the method. Source: B.P. Koester et al. 2007, *MaxBCG: A Red-Sequence Galaxy Cluster Finder*, ApJ 660, 221, p. 224, Fig. 1. ©AAS. Reproduced with permission

The maxBCG catalog. The large sky coverage of the SDSS, and the very homogeneous photometry of the five-band imaging data, makes this survey a prime resource for optical cluster finders. Whereas the SDSS is rather shallow, compared to the RCS surveys, and thus cannot find clusters at high redshifts, it enables the most complete cluster searches in the more local Universe. Therefore, several cluster catalogs have been constructed from the SDSS, one of which we want to briefly describe here.

This maxBCG cluster catalog is based on a search algorithm which makes use of three properties of massive clusters. The first is the already mentioned red cluster sequence, i.e., the homogeneous (and redshift dependent) color of early-type galaxies in clusters. Second, most massive clusters are found to have a dominant central galaxy, the brightest cluster galaxy (BCG), whose luminosity can be several times larger than the second brightest cluster member. The third property relates to the radial density profile of galaxies, which, in a first approximation, decreases roughly as $1/\theta$ from the center to the outside.

Thus, the algorithm searches for overdensities of galaxies with similar color, corresponding to the color of the red sequence within a specified redshift interval, where the brightest of the galaxies is located near the center of the overdensity, and where the radial decline of the galaxy number density is compatible with a $1/\theta$-law. More specifically, the maxBCG method searches for concentrations of luminous red galaxies in the redshift interval $0.1 \lesssim z \lesssim 0.3$, whose colors agree to within $\pm 2\sigma$ of the width of the red sequence in color and with the brightest of these galaxies near the center (Fig. 6.13). The choice of this redshift interval is motivated by the fact that the $g - r$ color of red galaxies is a simple function of redshift, as the strong 4000 Å-break of early-type galaxies moves through the g-filter in this redshift interval. The color of the overdense population yields an indication of the redshift, which then allows one to obtain the galaxy luminosity from the observed flux. Only red galaxies more luminous than $0.4L^*$ are taken into account. Given the depth of the SDSS, a red galaxy with $L \geq 0.4L^*$ at $z = 0.3$ can be detected—hence, this provides a volume-limited survey for such galaxies. Furthermore, the redshift estimate is used to obtain the physical projected radius R from the observed angular separation.

To characterize the cluster candidate, the number of red sequence galaxies with $L \geq 0.4L^*$ within $1h^{-1}$ Mpc of the BCG candidate, N_g, is calculated. For reasons that will become clear when we discuss the formation of dark matter halos in Sect. 7.5.1 (see also Problem 6.1), one defines the 'extent' of a cluster to be the radius inside of which the mean density is 200 times larger than the critical density of the Universe at this redshift. This radius is denoted by r_{200}, and the mass of the cluster within r_{200} is then denoted as $M_{200} = (4\pi/3)200\rho_{cr}(z)r_{200}^3$, often also called the virial mass of the cluster. From earlier cluster studies, it was found that there is a close relation between r_{200} (or M_{200}) and the number of galaxies within $1h^{-1}$ Mpc, roughly following $r_{200} \propto N_g$. With this estimate of the virial radius, the number of red sequence members within projected radius $R = r_{200}$ is measured and denoted by $N_{g,200}$, which is then called the richness of the cluster.

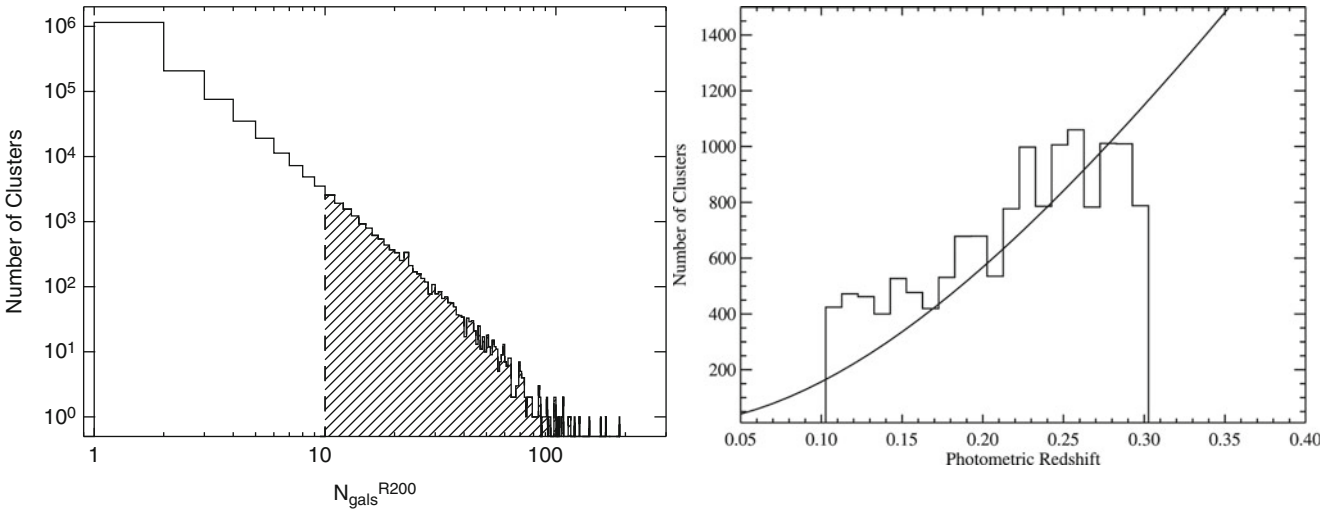

Fig. 6.14 *Left*: Histogram of the number of clusters found by the maxBCG method, as a function of cluster richness $N_{g,200}$. The maxBCG catalog consists of 13 823 clusters with $N_{g,200} \geq 10$, shown as hatched region in the histogram. The *right panel* shows the distribution of estimated redshifts, whereas the *solid curve* is the expected redshift distribution for a volume-limited survey with the sky area of the SDSS at a given mean number density of $2.3 \times 10^{-5} h^3\,\mathrm{Mpc}^{-3}$. Source: B.P. Koester et al. 2007, *A MaxBCG Catalog of 13,823 Galaxy Clusters from the Sloan Digital Sky Survey*, ApJ 660, 239, p. 243, 244, Figs. 3, 4. ©AAS. Reproduced with permission

These criteria have yielded a catalog of 13 823 clusters with $N_{g,200} \geq 10$ in the 7500 deg^2 of the SDSS. Their distribution in richness and redshift is shown in Fig. 6.14. This maxBCG catalog is one of the largest cluster catalogs available up to now and has been widely used.

The quality of the catalog can be assessed in a number of ways. Since the SDSS also has a large spectroscopic component, the spectroscopic redshifts for more than 5000 of the BCGs are known; they can be compared to the redshift estimated from the color of the red-sequence cluster members. The difference between the two redshifts has a very narrow distribution with a width of $\sigma_z \sim 0.01$—that is, the estimated cluster redshifts are very accurate.

A good catalog should be pure and complete. As mentioned before, purity measures the fraction of objects included in the catalog which are not real clusters, whereas completeness quantifies the number of real clusters which were missed by the selection algorithm. These two quantities can be estimated from simulations, in which mock cluster catalogs are generated and analyzed with the same detection algorithm as the real data. Based on such simulations, one concludes that the maxBCG catalog is $\sim$ 90 % pure and $\sim$ 85 % complete, for clusters with masses $\geq 10^{14} M_\odot$, corresponding to $N_{g,200} \approx 10$.

The available spectroscopy of the SDSS can also be used to determine the velocity dispersion σ_v for many of the clusters. The left panel of Fig. 6.15 shows a strong correlation between σ_v and richness, well fit by a power law of the form

$$\sigma_v = 500\,\mathrm{km/s} \left(\frac{N_{g,200}}{10} \right)^{0.31} . \qquad (6.7)$$

This strong correlation also shows that cluster richness is a good indicator of cluster mass, since σ_v is expected to be tightly related to the mass, according to the virial theorem; we will return to this aspect soon. The comoving number density of clusters as a function of redshift is shown in the right panel of Fig. 6.15, for different richness bins. The comoving space density is roughly constant for all bins except for the richest, which suggests that the maxBCG catalog does not suffer from serious redshift-dependent incompleteness. The slight decline with increasing redshift in the richest bin is actually expected from structure formation in the Universe, as we will discuss in Sect. 7.5.2.

For candidates with $N_{g,200} < 10$, i.e., mass below $\sim 10^{14}\,M_\odot$, the purity and completeness decrease; hence, whereas a large fraction of these candidates are probably clusters or groups at lower mass, projection effects will play an increasingly important role for decreasing richness. To reliably find groups, the selection criteria need to be sharpened, which can be done using spectroscopic redshifts. With those, one can search for galaxy overdensities on the sky which have the same redshifts within a few times the expected velocity dispersion in groups, i.e., the same radial velocity within $\sim$ 1000 km/s. This provides a much stricter redshift constraint than is possible with the red sequence method and thus substantially reduces projection effects. Such group catalogs were constructed from the Two-degree field Galaxy Redshift Survey (see Sect. 8.1.2) and the SDSS as well. The velocity dispersion in groups is significantly smaller than that in clusters; typical values for groups with only a few members are $\sigma_v \sim 300$ km/s (see Fig. 6.15).

6.3 Light distribution and cluster dynamics

6.3.1 Spatial distribution of galaxies

Most regular clusters show a centrally condensed number density distribution of cluster galaxies, i.e., the galaxy den-

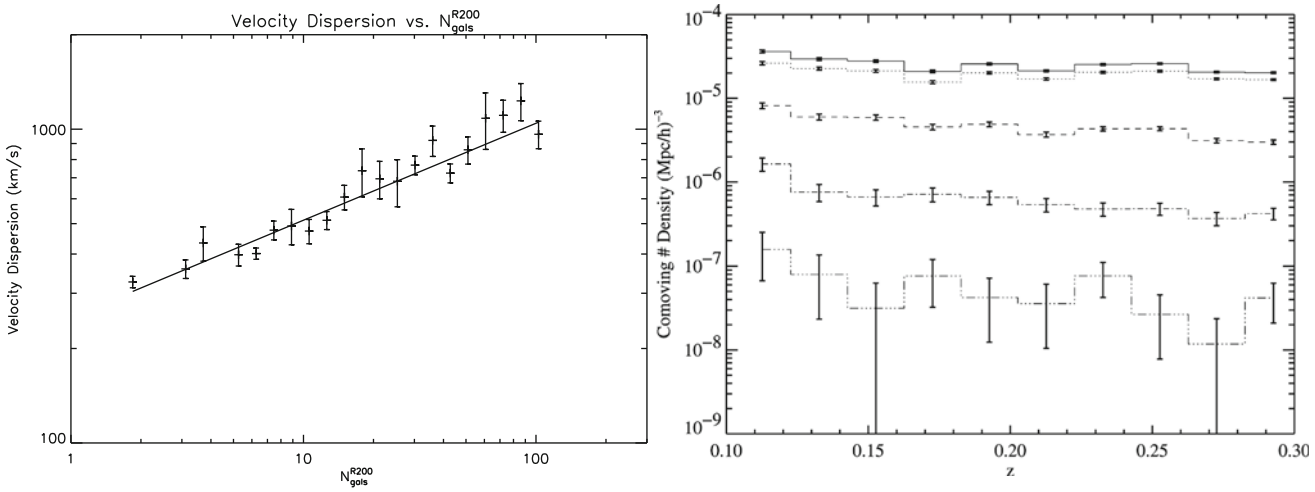

Fig. 6.15 *Left*: The velocity dispersion of maxBCG clusters, as a function of richness $N_{\mathrm{g},200}$. Note that the figure extends to richness as small as $N_{\mathrm{g},200} = 2$. At the threshold of the cluster catalog, $N_{\mathrm{g},200} = 10$, the characteristic velocity dispersion is $\sim 500\,\mathrm{km/s}$. *Right*: The comoving number density of clusters in the maxBCG catalog, as a function of redshift, for four different redshift bins (*from top to bottom*: $10 \le N_{\mathrm{g},200} < 20$, $20 \le N_{\mathrm{g},200} < 43$, $43 \le N_{\mathrm{g},200} < 91$, $91 \le N_{\mathrm{g},200} < 189$). Source: B.P. Koester et al. 2007, *A MaxBCG Catalog of 13,823 Galaxy Clusters from the Sloan Digital Sky Survey*, ApJ 660, 239, p. 251, Figs. 12, 13. ©AAS. Reproduced with permission

sity increases strongly towards the center. If the cluster is not very elongated, this density distribution can be assumed, to a first approximation, as being spherically symmetric. Only the projected density distribution $N(R)$ is observable. This is related to the three-dimensional number density $n(r)$ through

$$N(R) = \int_{-\infty}^{\infty} \mathrm{d}r_3 \, n\left(\sqrt{R^2 + r_3^2}\right) = 2\int_R^{\infty} \frac{\mathrm{d}r \; r\, n(r)}{\sqrt{r^2 - R^2}} \,, \tag{6.8}$$

where in the second step a simple transformation of the integration variable from the line-of-sight coordinate r_3 to the three-dimensional radius $r = \sqrt{R^2 + r_3^2}$ was made.

Of course, no function $N(R)$ can be observed, but only points (the positions of the galaxies) that are distributed in a certain way. If the number density of galaxies is sufficiently large, $N(R)$ is obtained by smoothing the point distribution. Alternatively, one considers parametrized forms of $N(R)$ and fits the parameters to the observed galaxy positions. In most cases, the second approach is taken because its results are more robust. A parametrized distribution needs to contain at least five parameters to be able to describe at least the basic characteristics of a cluster. Two of these parameters describe the position of the cluster center on the sky. One parameter is used to describe the amplitude of the density, for which, e.g., the central density $N_0 = N(0)$ may be used. A fourth parameter is a characteristic scale of a cluster, often taken to be the core radius r_{c}, defined such that at $R = r_{\mathrm{c}}$, the projected density has decreased to half the central value, $N(r_{\mathrm{c}}) = N_0/2$. Finally, one parameter is needed to describe 'where the cluster ends'; the Abell radius is a first approximation for such a parameter.[4]

Parametrized cluster models can be divided into those which are physically motivated, and those which are of a purely mathematical nature. One example for the latter is the family of Sérsic profiles which is not derived from dynamical models. Next, we will consider a class of distributions that are based on a dynamical model.

Isothermal distributions. These models are based on the assumption that the velocity distribution of the massive particles (this may be both galaxies in the cluster or dark matter particles) of a cluster is locally described by a Maxwell distribution, i.e., they are 'thermalized'. As shown from spectroscopic analyses of the distribution of the radial velocities of cluster galaxies, this is not a bad assumption. Assuming, in addition, that the mass profile of the cluster follows that of the galaxies (or vice versa), and that the temperature (or equivalently the velocity dispersion) of the distribution does not depend on the radius, so that one has an isothermal distribution of galaxies, then one obtains a one-parameter set of models, the so-called *isothermal spheres*. These can be described physically as follows.

In dynamical equilibrium, the pressure gradient must be equal to the gravitational acceleration, so that

$$\boxed{\frac{\mathrm{d}P}{\mathrm{d}r} = -\rho\,\frac{GM(r)}{r^2}} \,, \tag{6.9}$$

where $\rho(r)$ denotes the density of the distribution, e.g., the density of galaxies. By $\rho(r) = \langle m\rangle\, n(r)$, this mass density is related to the number density $n(r)$, where $\langle m\rangle$ is the average particle mass. $M(r) =$

[4] In principle, one might need more parameters for describing the radial profile of clusters, and thus the parameters mentioned are a bare minimum. However, as we shall see later, it appears that the mass profiles of clusters are all very similar. Cosmological simulations of structure evolution in the Universe predict that the density profiles of clusters can indeed be characterized by this minimum set.

$4\pi \int_0^r \mathrm{d}r'\, r'^2\, \rho(r')$ is the mass of the cluster enclosed within a radius r. By differentiation of (6.9), we obtain

$$\frac{\mathrm{d}}{\mathrm{d}r}\left(\frac{r^2}{\rho}\frac{\mathrm{d}P}{\mathrm{d}r}\right) + 4\pi G r^2 \rho = 0\,. \tag{6.10}$$

The relation between pressure and density is $P = nk_\mathrm{B}T$. On the other hand, the temperature is related to the velocity dispersion of the particles,

$$\frac{3}{2}k_\mathrm{B}T = \frac{\langle m\rangle}{2}\langle v^2\rangle\,, \tag{6.11}$$

where $\langle v^2\rangle$ is the mean squared velocity, i.e., the velocity dispersion, provided the average velocity vector is set to zero. The latter assumption means that the cluster does not rotate, or contract or expand. If T (or $\langle v^2\rangle$) is independent of r, then

$$\frac{\mathrm{d}P}{\mathrm{d}r} = \frac{k_\mathrm{B}T}{\langle m\rangle}\frac{\mathrm{d}\rho}{\mathrm{d}r} = \frac{\langle v^2\rangle}{3}\frac{\mathrm{d}\rho}{\mathrm{d}r} = \sigma_v^2\frac{\mathrm{d}\rho}{\mathrm{d}r}\,, \tag{6.12}$$

where σ_v^2 is the one-dimensional velocity dispersion, e.g., the velocity dispersion along the line-of-sight, which can be measured from the redshifts of the cluster galaxies. If the velocity distribution corresponds to an isotropic (Maxwell) distribution, the one-dimensional velocity dispersion is exactly 1/3 times the three-dimensional velocity dispersion, because of $\langle v^2\rangle = \sigma_x^2 + \sigma_y^2 + \sigma_z^2$, or

$$\sigma_v^2 = \frac{\langle v^2\rangle}{3}\,. \tag{6.13}$$

With (6.10), it then follows that

$$\frac{\mathrm{d}}{\mathrm{d}r}\left(\frac{\sigma_v^2 r^2}{\rho}\frac{\mathrm{d}\rho}{\mathrm{d}r}\right) + 4\pi G r^2 \rho = 0\,. \tag{6.14}$$

Singular isothermal sphere. For general boundary conditions, the differential equation (6.14) for $\rho(r)$ cannot be solved analytically. However, one particular analytical solution of the differential equation exists: By substitution, we can easily show that

$$\boxed{\rho(r) = \frac{\sigma_v^2}{2\pi G r^2}} \tag{6.15}$$

solves (6.14). This density distribution is called *singular isothermal sphere*; we have encountered it before, in the discussion of gravitational lens models in Sect. 3.11.2. This distribution has a diverging density as $r \to 0$ and an infinite total mass $M(r) \propto r$. It is remarkable that this density distribution, $\rho \propto r^{-2}$, is just what is needed to explain the flat rotation curves of galaxies at large radii.

The divergence of the density towards the center may not appear reasonable, and thus one might search solutions of (6.14) with the more physical boundary conditions $\rho(0) = \rho_0$, the central density, and $(\mathrm{d}\rho/\mathrm{d}r)_{|r=0} = 0$, for the density profile to be flat at the center. Numerical solutions of (6.14) with these boundary conditions (thus, with a flat core) reveal that the central density and the core radius are related to each other by

$$\boxed{\rho_0 = \frac{9\sigma_v^2}{4\pi G r_\mathrm{c}^2}}\,. \tag{6.16}$$

Hence, these physical solutions of (6.14) avoid the infinite density of the singular isothermal sphere. However, these solutions also decrease outwards with $\rho \propto r^{-2}$, so they have a diverging mass as well. The origin of this mass divergence is easily understood because these isothermal distributions are based on the assumption that the velocity distribution is isothermal, thus Maxwellian with a spatially constant temperature. A Maxwell distribution has wings, hence it (formally) contains particles with arbitrarily high velocities. Since the distribution is assumed stationary, such particles must not escape, so their velocity must be lower than the escape velocity from the gravitational well of the cluster. But for a Maxwell distribution this is only achievable for an infinite total mass.

King models. To remove the problem of the diverging total mass, self-gravitating dynamical models with an upper cut-off in the velocity distribution of their constituent particles are introduced. These are called *King models* and cannot be expressed analytically. However, an analytical approximation exists for the central region of these mass profiles,

$$\boxed{\rho(r) = \rho_0\left[1 + \left(\frac{r}{r_\mathrm{c}}\right)^2\right]^{-3/2}}\,. \tag{6.17}$$

Using (6.8), we obtain from this the projected surface mass density

$$\boxed{\Sigma(R) = \Sigma_0\left[1 + \left(\frac{R}{r_\mathrm{c}}\right)^2\right]^{-1} \quad \text{with} \quad \Sigma_0 = 2\rho_0 r_\mathrm{c}}\,. \tag{6.18}$$

The analytical fit (6.17) of the King profile also has a diverging total mass, but this divergence is 'only' logarithmic.

These analytical models for the density distribution of galaxies in clusters are only approximations, of course, because the galaxy distribution in clusters is often heavily structured. Furthermore, these dynamical models are applicable to a galaxy distribution only if the galaxy number density follows the matter density. However, one finds that the distribution of galaxies in a cluster often depends on the galaxy type. The fraction of early-type galaxies (Es and S0s) is often largest near the center. Therefore, one should consider the possibility that the distribution of galaxies in a cluster may be different from that of the total matter. A typical value for the core radius is about $r_\mathrm{c} \sim 0.25h^{-1}$ Mpc.

6.3.2 Dynamical mass of clusters

The above argument relates the velocity distribution of cluster galaxies to the mass profile of the cluster, and from this we obtain physical models for the density distribution. This implies the possibility of deriving the mass, or the mass profile, respectively, of a cluster from the observed velocities of cluster galaxies. We will briefly present this method of mass determination here. For this, we consider the dynamical time-scale of clusters, defined as the time a typical galaxy needs to traverse the cluster once,

$$\boxed{t_{\rm cross} \sim \frac{R_{\rm A}}{\sigma_v} \sim 1.5 h^{-1} \times 10^9 \,{\rm yr}} \,, \tag{6.19}$$

where a (one-dimensional) velocity dispersion $\sigma_v \sim 1000\,{\rm km/s}$ was assumed. The dynamical time-scale is shorter than the age of the Universe. One therefore concludes that clusters of galaxies are gravitationally bound systems. If this were not the case they would dissolve on a timescale $t_{\rm cross}$. Since $t_{\rm cross} \ll t_0$ one assumes a *virial equilibrium*, hence that the virial theorem applies, so that in a time-average sense,

$$2E_{\rm kin} + E_{\rm pot} = 0 \,, \tag{6.20}$$

where

$$E_{\rm kin} = \frac{1}{2} \sum_i m_i \, v_i^2 \quad ; \quad E_{\rm pot} = -\frac{1}{2} \sum_{i \neq j} \frac{G m_i m_j}{r_{ij}} \tag{6.21}$$

are the kinetic and the potential energy of the cluster galaxies, m_i is the mass of the i-th galaxy, v_i is the absolute value of its velocity, and r_{ij} is the spatial separation between the i-th and the j-th galaxy. The factor $1/2$ in the definition of $E_{\rm pot}$ occurs since each pair of galaxies occurs twice in the sum.

In writing (6.21) we have assumed that the total mass of the cluster is the sum of all its member galaxies,

$$M := \sum_i m_i \,. \tag{6.22}$$

This assumption is not valid, since, as we will find below, most of the cluster mass is not contained in galaxies. However, if we assume that the total mass is distributed in the same way as the galaxies are, we can associate to each galaxy a 'representative' mass, so that the superposition of all these representative masses yields the total mass distribution of the cluster. The mass m_i used in the foregoing equations and below is meant to be this representative mass.

We further define the velocity dispersion, weighted by mass,

$$\langle v^2 \rangle := \frac{1}{M} \sum_i m_i \, v_i^2 \tag{6.23}$$

and the gravitational radius,

$$r_{\rm G} := 2M^2 \left(\sum_{i \neq j} \frac{m_i \, m_j}{r_{ij}} \right)^{-1} \,. \tag{6.24}$$

With this, we obtain

$$E_{\rm kin} = \frac{M}{2} \langle v^2 \rangle \quad ; \quad E_{\rm pot} = -\frac{G \, M^2}{r_{\rm G}} \tag{6.25}$$

for the kinetic and potential energy. Applying the virial theorem (6.20) yields the mass estimate

$$\boxed{M = \frac{r_{\rm G} \langle v^2 \rangle}{G}} \,. \tag{6.26}$$

Transition to projected quantities. The above derivation uses the three-dimensional separations r_i of the galaxies from the cluster center, which are, however, not observable. To be able to apply these equations to observations, they need to be transformed to projected separations. If the galaxy positions and the directions of their velocity vectors are uncorrelated, as it is the case, e.g., for an isotropic velocity distribution, then

$$\langle v^2 \rangle = 3\sigma_v^2, \;\; r_{\rm G} = \frac{\pi}{2} R_{\rm G} \;\; \text{with} \;\; R_{\rm G} = 2M^2 \left(\sum_{i \neq j} \frac{m_i m_j}{R_{ij}} \right)^{-1} \,, \tag{6.27}$$

where R_{ij} denotes the projected separation between the galaxies i and j. The parameters σ_v and $R_{\rm G}$ are direct observables; thus, the total mass of the cluster can be determined. One obtains

$$\boxed{M = \frac{3\pi R_{\rm G} \sigma_v^2}{2G} = 1.1 \times 10^{15} M_\odot \left(\frac{\sigma_v}{1000 {\rm km/s}} \right)^2 \left(\frac{R_{\rm G}}{1 {\rm Mpc}} \right)} \,. \tag{6.28}$$

We explicitly point out that this mass estimate no longer depends on the masses m_i of the individual galaxies—rather the galaxies are now test particles in the gravitational potential. With $\sigma_v \sim 1000\,{\rm km/s}$ and $R_{\rm G} \sim 1\,{\rm Mpc}$ as typical values for rich clusters of galaxies, one obtains a characteristic mass of $\sim 10^{15} M_\odot$ for rich clusters.

The 'missing mass' problem in clusters of galaxies. With the mass M and the number N of galaxies, one can now derive a characteristic mass $m = M/N$ for the luminous galaxies. This mass is found to be very high, $m \sim 10^{13} M_\odot$. Alternatively, M can be compared with the total optical luminosity of the cluster galaxies, $L_{\rm tot} \sim 10^{12}$-$10^{13}\, L_\odot$, and

hence the mass-to-light ratio can be calculated; typically

$$\boxed{\left(\frac{M}{L_{\rm tot}}\right) \sim 300\,h\left(\frac{M_\odot}{L_\odot}\right)}\,. \tag{6.29}$$

This value exceeds the M/L-ratio of early-type galaxies by at least a factor of 10. Realizing this discrepancy, Fritz Zwicky concluded as early as 1933, from an analysis of the Coma cluster, that clusters of galaxies must contain considerably more mass than is visible in galaxies—the dawn of the *missing mass problem*. As we will see further below, this discrepancy between the observed luminosity and estimated mass has by now been firmly established, since other methods for the mass determination of clusters also yield comparable values and indicate that a major fraction of the mass in galaxy clusters consists of (non-baryonic) dark matter. *The stars visible in galaxies contribute less than about 5 % to the total mass in clusters of galaxies.*

6.3.3 Additional remarks on cluster dynamics

Given the above line of argument, the question of course arises as to whether the application of the virial theorem is still justified if the main fraction of mass is not contained in galaxies. The derivation remains valid in this form as long as the spatial distribution of galaxies follows the total mass distribution. The dynamical mass determination can be affected by an anisotropic velocity distribution of the cluster galaxies and by the possibly non-spherical cluster mass distribution. In both cases, projection effects, which are dealt with relatively easily in the spherically-symmetric case, obviously become more complicated. This is also one of the reasons for the necessity to consider alternative methods of mass determination.

Two-body collisions of galaxies in clusters are of no importance dynamically, as is easily seen from the corresponding relaxation time-scale (3.3),

$$t_{\rm relax} = t_{\rm cross}\frac{N}{\ln N}\,,$$

which is much larger than the age of the Universe. The motion of galaxies is therefore governed by the collective gravitational potential of the cluster. The velocity dispersion is approximately the same for the different types of galaxies, and also only a weak tendency exists for a dependence of σ_v on galaxy luminosity, restricted to the brightest ones (see below in Sect. 6.7.2). From this, we conclude that the galaxies in a cluster are not "thermalized" because this would mean that they all have the same mean kinetic energy, implying $\sigma_v \propto m^{-1/2}$. Furthermore, the independence of σ_v of L reconfirms that collisions of galaxies with each other are not dynamically relevant; rather, the velocity distribution of galaxies is defined by collective processes during cluster formation.

Violent relaxation. One of the most important of the aforementioned processes is known as *violent relaxation*. This process very quickly establishes a virial equilibrium in the course of the gravitational collapse of a mass concentration. The reason for it are the small-scale density inhomogeneities within the collapsing matter distribution which generate, via Poisson's equation, corresponding fluctuations in the gravitational field. These then scatter the infalling particles and, by this, the density inhomogeneities are further amplified. The fluctuations of the gravitational field act on the matter like scattering centers. In addition, these field fluctuations change over time, yielding an effective exchange of energy between the particles. In a statistical average, all galaxies obtain the same velocity distribution by this process. As confirmed by numerical simulations, this process takes place on a time-scale of $t_{\rm cross}$, i.e., roughly as quickly as the collapse itself.

Dynamical friction. Another important process for the dynamics of galaxies in a cluster is *dynamical friction*. The simplest picture of dynamical friction is obtained by considering the following. If a massive particle of mass m moves through a statistically homogeneous distribution of massive particles, the gravitational force on this particle vanishes due to homogeneity. But since the particle itself has a mass, it will attract other massive particles and thus cause the distribution to become inhomogeneous. As the particle moves, the surrounding 'background' particles will react to its gravitational field and slowly start moving towards the direction of the particle trajectory. Due to the inertia of matter, the resulting density inhomogeneity will be such that an overdensity of mass will be established along the track of the particle, where the density will be higher on the side opposite to the direction of motion (thus, behind the particle) than in the forward direction (see Fig. 6.16). By this process, a gravitational field will form that causes an acceleration of the particle against the direction of motion, so that the particle will be slowed down. Because this 'polarization' of the medium is caused by the gravity of the particle, which is proportional to its mass, the deceleration will also be proportional to m. Furthermore, a fast-moving particle will cause less polarization in the medium than a slowly moving one because each mass element in the medium is experiencing the gravitational attraction of the particle for a shorter time, thus the medium becomes less polarized. In addition, the particle is on average farther away from the density accumulation on its backward track, and thus will experience a smaller acceleration if it is faster. Combining these arguments, one obtains for the dependence of this dynamical friction

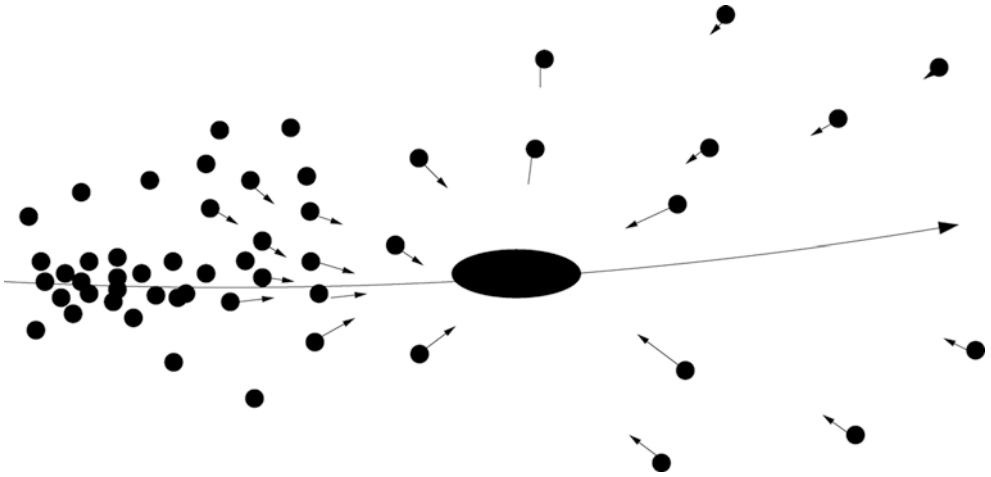

Fig. 6.16 The principle of dynamical friction. The gravitational field of a massive particle (here indicated by the *large symbol*) accelerates the surrounding matter towards its track. Through this, an overdensity establishes on the backward side of its orbit, the gravitational force of which decelerates the particle

$$\frac{\mathrm{d}\boldsymbol{v}}{\mathrm{d}t} \propto -\frac{m\,\rho\,\boldsymbol{v}}{|\boldsymbol{v}|^3}\ , \tag{6.30}$$

where ρ is the mass density in the medium. Applied to clusters of galaxies, this means that the most massive galaxies will experience the strongest dynamical friction, so that they are subject to a significant deceleration through which they move deeper into the potential well. The most massive cluster galaxies should therefore be concentrated around the cluster center, so that a spatial separation of galaxy populations with respect to their masses occurs (mass segregation). If dynamical friction acts over a sufficiently long time, the massive cluster galaxies in the center may merge into a single one. This is one possible explanation for the formation of cD galaxies. Furthermore, as the most massive (and thus presumably also the most luminous) galaxies are affected strongest by dynamical friction, and are thus the prime candidates for merging with the central galaxy, this may explain the observed gap of $\sim$ 2 mag between the brightest and second brightest cluster galaxy.

Dynamical friction also plays an important role in other dynamical processes in astrophysics. For example, the Magellanic Clouds experience dynamical friction on their orbit around the Milky Way and thereby lose kinetic energy. Consequently, their orbit will become smaller over the course of time and, in a distant future, these two satellite galaxies will merge with our Galaxy. In fact, dynamical friction is of vital importance in galaxy merger processes which occur in the evolution of the galaxy population, a subject we will return to in Chap. 10.

Compact groups have a lifetime which is much shorter than the age of the Universe. The dynamical time-scale is $t_{\mathrm{dyn}} \sim R/\sigma_v \sim 0.02\,H_0^{-1}$, thus small compared to $t_0 \sim H_0^{-1}$. By dynamical friction, galaxies in groups lose kinetic (orbital) energy and move closer to the dynamical center where interactions and mergers with other group galaxies take place, as also seen by the high fraction of member galaxies with morphological signs of interactions. Since the lifetime of compact groups is shorter than the age of the Universe, they must have formed not too long ago. If we do not happen to live in a special epoch of cosmic history, such groups must therefore still be forming today. From dynamical studies, one estimates that—as in clusters—the total mass of groups is significantly larger than the sum of the mass visible in galaxies; a typical mass-to-light ratio is $M/L \sim 50h$ (in Solar units), which is comparable to that of the Local Group.

6.3.4 Intergalactic stars in clusters of galaxies

The space between the galaxies in a cluster is filled with hot gas, as visible from X-ray observations. Besides this hot gas there are also stars in between the galaxies. This *intracluster light (ICL)* is the most recently discovered component in clusters. The detection of such an intergalactic stellar population comes as a surprise at first sight, because our understanding of star formation implies that they can only form in the dense centers of molecular clouds. Hence, one expects that stars cannot form in intergalactic space. This is not necessarily implied by the presence of intergalactic stars, however, since they can also be stripped from galaxies in the course of gravitational interactions between galaxies in the cluster, or the stripping of stars from the outer parts of galaxies in the tidal gravitational field (in the central region) of the cluster, and so form an intergalactic population. The fate of these stars is thus somewhat similar to that of the interstellar medium, which is metal-enriched by the processes of stellar evolution in galaxies before it is removed from these galaxies and becomes part of the intergalactic medium in clusters; otherwise, the substantial metallicity of the ICM could not be explained.[5] This interpretation is strengthened by the fact that a diffuse optical light component is also

[5] Of course, stars in galaxies are not subject to ram pressure stripping as is their gas.

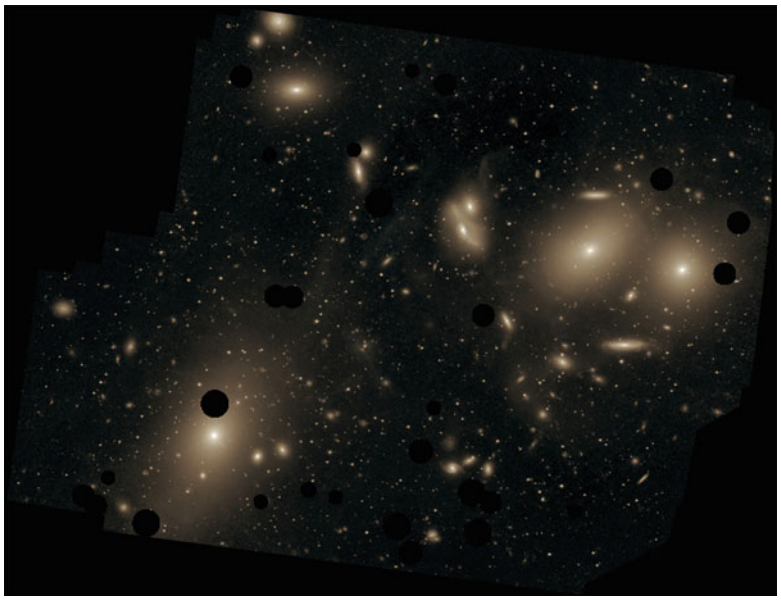

Fig. 6.17 This image shows the central part of the Virgo cluster, with its central galaxy M87 located in the *lower left corner*. The size of the image is about 1.5°; it shows the diffuse light in the cluster between the cluster galaxies. *Dark spots* indicate regions that were masked, e.g. because of bright foreground stars. The brightest parts before saturation have a surface brightness of $\mu_V \sim 26.5\,\mathrm{mag/arcsec^2}$, the faintest visible features have $\mu_V \sim 28.5\,\mathrm{mag/arcsec^2}$. Credit: Chris Mihos (Case Western Reserve University)/European Southern Observatory

seen in (compact) galaxy groups where the strength of tidal interactions is stronger than in clusters.

Observation of intracluster light. The observation of diffuse optical light in clusters of galaxies and, related to this, the detection of the intracluster stellar population, is extremely difficult. Although first indications were already found with photographic plate measurements, the surface brightness of this cluster component is so low that even with CCD detectors the observation is extraordinarily challenging. To quantify this, we note that the surface brightness of this diffuse light component is about $30\,\mathrm{mag\,arcsec^{-2}}$ at a distance of several hundred kpc from the cluster center. This value needs to be compared with the brightness of the night sky, which is about $21\,\mathrm{mag\,arcsec^{-2}}$ in the V-band. One therefore needs to correct for the effects of the night sky to better than a tenth of a percent for the intergalactic stellar component to become visible in a cluster. Furthermore, cluster galaxies and objects in the foreground and background need to be masked out in the images, in order to measure the radial profile of this diffuse component. This is possible only up to a certain limiting magnitude, of course, up to which individual objects can be identified. The existence of weaker sources has to be accounted for with statistical methods, which in turn use the luminosity function of galaxies. An example of this ICL is shown in Fig. 6.17.

The identification of this diffuse optical light as truly intergalactic origin is hampered by the fact that many clusters host a central cD galaxy. As we mentioned in Sect. 3.2.2 (see also Fig. 3.11), such galaxies have an extended brightness profile with a surface brightness substantially higher than the extrapolation of a de Vaucouleurs profile at large radii. Thus the natural question arises whether the diffuse component is just part of the cD envelope or a separate entity. If the ICL belongs to the central galaxy, it should be gravitationally bound to it; otherwise, it is a genuine intracluster component. This issue can be investigated by kinematical observations of individual stars in the ICL. One finds that the velocity dispersion of the stars in the ICL strongly increases away from the central galaxy, suggesting that they are unbound to it. One of the best individual tracers of the ICL are planetary nebulae which are formed in the final stages of Solar-mass stars. Since they emit a large fraction of their energy in a single emission line, they are ideal targets for spectroscopy. The kinematic study of intergalactic planetary nebulae show that they are not part of the central cluster galaxy. Related studies were carried out also with red giant stars and globular clusters. Also, Type Ia supernovae were found in clusters, but outside any cluster galaxy.

The diffuse light component was investigated in a statistical superposition of the images of several galaxy clusters. Statistical fluctuations in the sky background and uncertainties in the flatfield[6] determination are in this case averaged out. In this analysis an $r^{-1/4}$-law is found for the light distribution in the inner region of clusters, i.e., the (de Vaucouleurs) brightness profile of the central galaxy is measured (see Fig. 6.18). For radii larger than about $\sim 50\,\mathrm{kpc}$, the brightness profile exceeds the extrapolation of the de Vaucouleurs profile, and is detected out to very large distances from the cluster center.

[6]The flatfield of an image (or, more precisely, of the system consisting of telescope, filter, and detector) is defined as the image of a uniformly illuminated field, so that in the ideal case each pixel of the detector produces the same output signal. This is not the case in reality, however, as the sensitivity differs for individual pixels. For this reason, the flatfield measures the sensitivity distribution of the pixels, which is then accounted for in the image analysis.

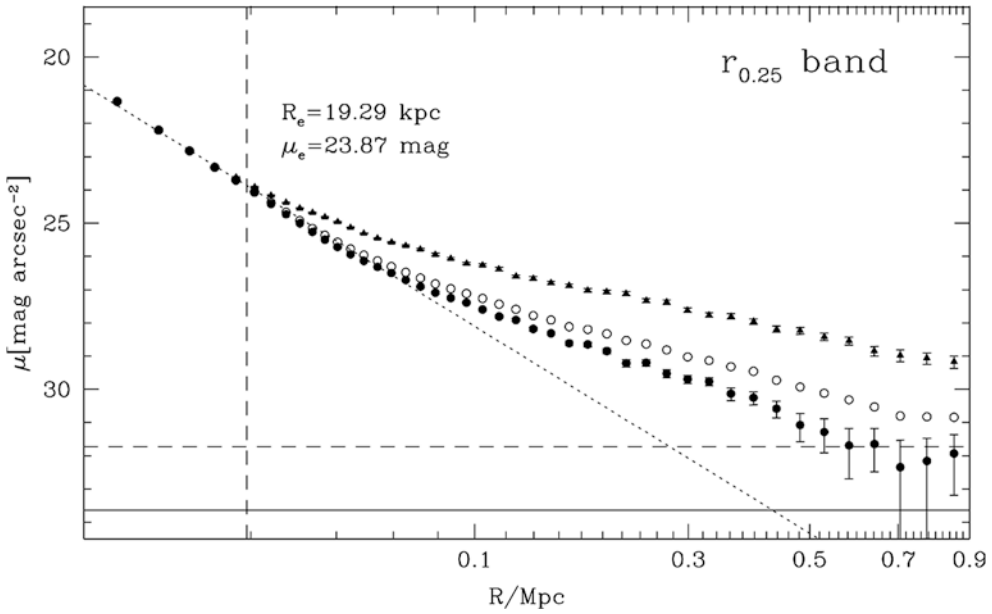

Fig. 6.18 The average light profile of 683 galaxy clusters from the maxBCG catalog (Sect. 6.2.4) with $0.2 \leq z \leq 0.3$. The *upper row of symbols* (*triangles*) show the total light profile, the *open circles* show the light profile after masking out identified galaxies (except the central BCG). Since these are detectable only up to some brightness limit, one can correct for this incompleteness by statistically subtracting fainter galaxies, based on an assumed luminosity function. This corrected brightness profile is shown as *filled circles* with error bars, which thus indicates the sum of the BCG light profile plus the intracluster light. In the inner part, this follows a de Vaucouleurs profile, indicated by the *dotted line*, but beyond ~ 60 kpc there is clear excess of light, detected out to almost 1 Mpc. Source: S. Zibetti et al. 2005, *Intergalactic stars in $z \sim 0.25$ galaxy clusters: systematic properties from stacking of Sloan Digital Sky Survey imaging data*, MNRAS 358, 949, p. 957, Fig. 5. Reproduced by permission of Oxford University Press on behalf of the Royal Astronomical Society

The ICL is best studied in nearby groups and clusters; only for them can individual objects be detected to a low luminosity level. Furthermore, the cosmological surface brightness dimming $\propto (1+z)^{-4}$ (see problem 6.2) renders the detection of ICL increasingly more difficult when turning to higher redshift. Nevertheless, an ICL component was discovered out to redshift $z \sim 0.5$, perhaps even as far out as $z \sim 1$. The diffuse cluster component accounts for about 10 % of the total optical light in a cluster; in some clusters this fraction can be even higher. Therefore, models of galaxy evolution in clusters should provide an explanation for these observations.

6.4 Hot gas in galaxy clusters

One of the most important discoveries of the UHURU X-ray satellite, launched in 1970, was the detection of X-ray radiation from massive clusters of galaxies. With the later Einstein X-ray satellite and more recently ROSAT, X-ray emission was also detected from lower-mass clusters and groups. Three examples for the X-ray emission of galaxy clusters are displayed in Figs. 6.19, 6.20, and 6.21. Figure 6.19 shows the Coma cluster of galaxies, observed with two different X-ray observatories. Although Coma was considered to be a fully relaxed cluster, distinct substructure is visible in its X-ray radiation. The cluster RXJ 1347−1145 (Fig. 6.20) is the most X-ray luminous cluster in the ROSAT All-Sky Survey (Sect. 6.4.5). A large mass estimate of this cluster also follows from the analysis of the gravitationally lensed arcs (see Sect. 6.6) that are visible in Fig. 6.20; the cover of this book shows a more recent image of this cluster, taken with the ACS camera on-board HST, where a large number of arcs can be readily detected. Finally, Fig. 6.21 shows a superposition of the X-ray emission and an optical image of the cluster MS 1054−03, which is situated at $z = 0.83$ and was for many years the highest redshift cluster known.

6.4.1 General properties of the X-ray radiation

Clusters of galaxies are the brightest extragalactic X-ray sources besides AGNs. If an X-ray telescope is pointed away from the Galactic disk, about 85 % of the detected sources are AGNs, the remaining ~ 15 % are clusters. In contrast to AGNs, for which the X-ray emission is essentially point-like, the X-ray emission of clusters is extended. Their characteristic luminosity is $L_X \sim 10^{43}$ erg/s up to $\sim 10^{45}$ erg/s for the most massive systems. The fact that this X-ray emission is spatially extended implies that it does not originate from individual galaxies. The spatial region from which we can

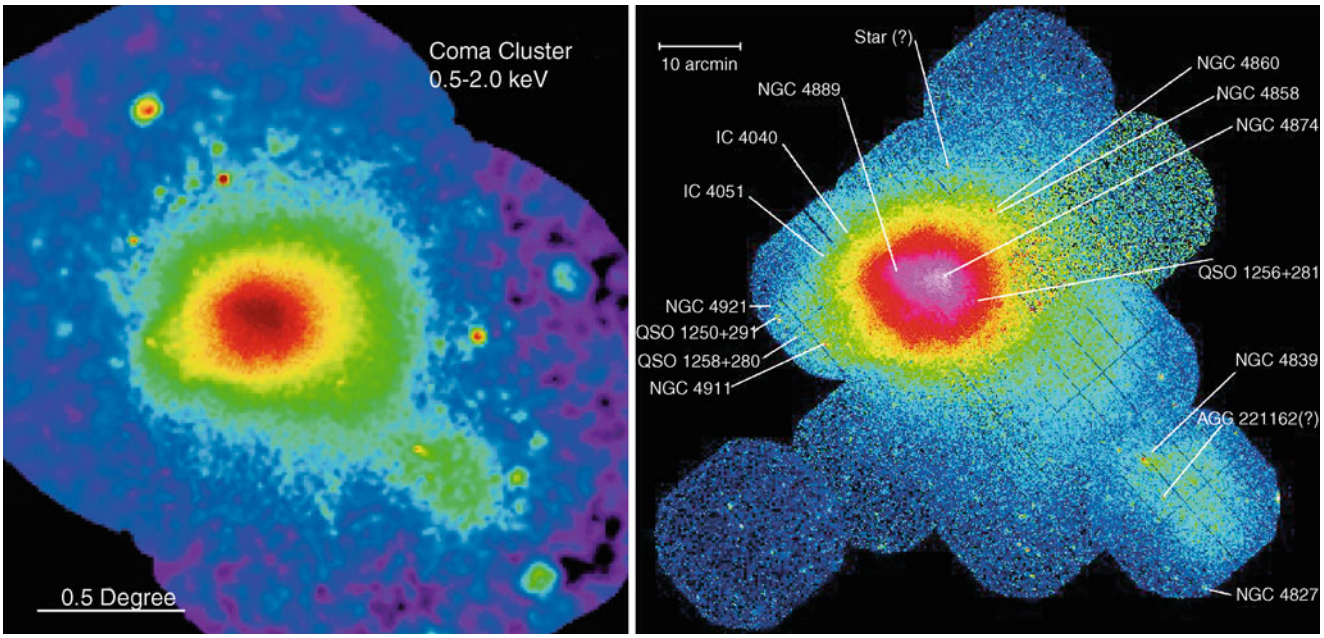

Fig. 6.19 X-ray images of the Coma cluster, taken with the ROSAT-PSPC (*left*) and XMM-EPIC (*right*). The image size in the *left panel* is $2.7° \times 2.5°$, much larger than the optical image shown in Fig. 1.17. A remarkable feature is the secondary maximum in the X-ray emission at the lower right of the cluster center which shows that even Coma, long considered to be a regular cluster, is not completely in an equilibrium state, but is dynamically evolving, presumably by the accretion of a galaxy group. Credit: *left*: S.L. Snowden, NASA, GSFC; *right*: U. Briel et al. 2001, *A mosaic of the Coma cluster of galaxies with XMM-Newton*, A&A 365, L60, p. L62, Fig. 1. ©ESO. Reproduced with permission

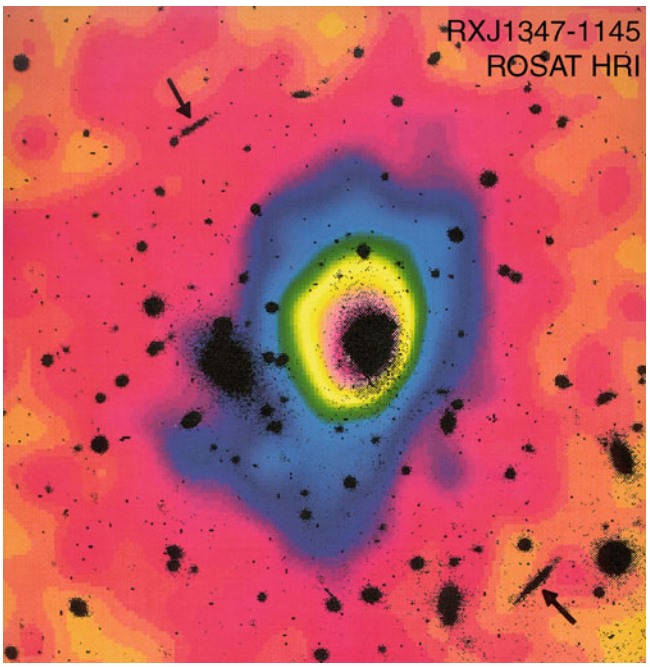

Fig. 6.20 RXJ 1347−1145 is one of the most luminous galaxy clusters in the X-ray domain. A color-coded ROSAT/HRI image of this cluster, which shows the distribution of the intergalactic gas, is superposed on an optical image of the cluster with redshift $z = 0.45$. The *two arrows* indicate giant arcs, images of background galaxies which are strongly distorted by the gravitational lens effect. Credit: Max-Planck-Institut für extraterrestrische Physik

detect this radiation can have a size of 1 Mpc or even larger. In accordance with the extended nature of the X-ray source, no variability of its X-ray flux has been detected.

Continuum radiation. The spectral energy distribution of the X-rays leads to the conclusion that the emission process is optically thin thermal bremsstrahlung (free-free radiation) from a hot gas which is collisionally ionized. This radiation is produced by the acceleration of electrons in the Coulomb field of protons and atomic nuclei. Since an accelerated electrically charged particle emits radiation, such scattering processes between electrons and protons in an ionized gas yields emission of photons. From the spectral properties of this radiation, the gas temperature in galaxy clusters can be determined, which is, for clusters with mass between $\sim 3 \times 10^{13} M_\odot$ and $\sim 10^{15} M_\odot$, in the range of 10^7 K to 10^8 K, or 1 to 10 keV, respectively.

The emissivity of bremsstrahlung is described by

$$\epsilon_\nu^{\mathrm{ff}} = \frac{32\pi Z^2 e^6 n_\mathrm{e} n_\mathrm{i}}{3 m_\mathrm{e} c^3} \sqrt{\frac{2\pi}{3 k_\mathrm{B} T m_\mathrm{e}}}\, \mathrm{e}^{-h_\mathrm{P}\nu/k_\mathrm{B}T}\, g_\mathrm{ff}(T,\nu)\ , \tag{6.31}$$

where e denotes the elementary charge, n_e and n_i the number density of electrons and ions, respectively, Ze the charge of the ions, and m_e the electron mass. The dimensionless func-

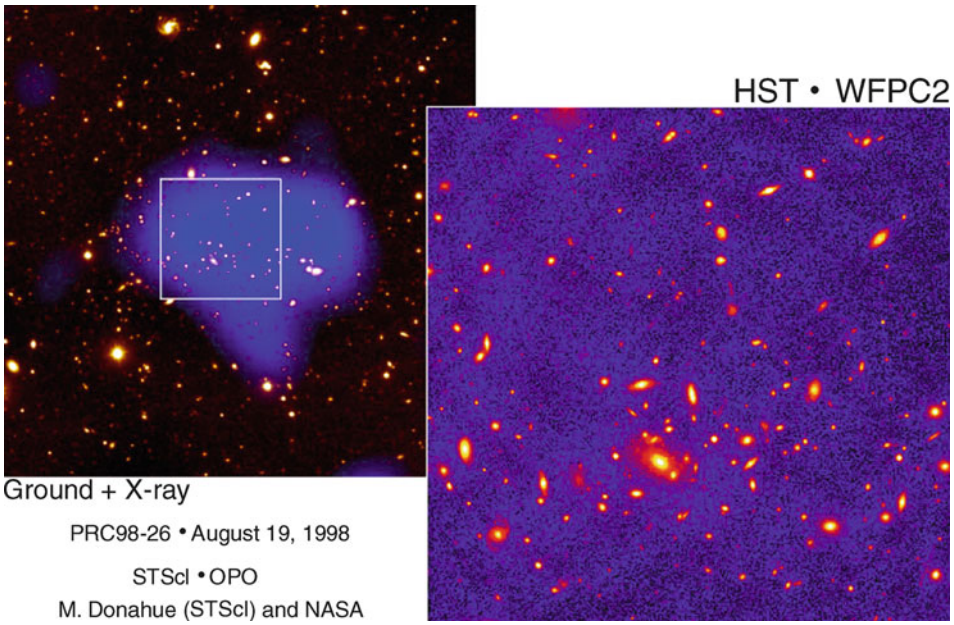

Fig. 6.21 The cluster of galaxies MS 1054−03 is, at $z = 0.83$, the highest-redshift cluster in the Einstein Medium Sensitivity Survey, which was compiled from observations with the Einstein satellite (see Sect. 6.4.5). *On the right*, an HST image of the cluster is shown, while *on the left* is an optical image, obtained with the 2.2-m telescope of the University of Hawaii, superposed (in *blue*) with the X-ray emission of the cluster measured with the ROSAT-HRI. Credit: Megan Donahue/STSCI, Isabella Gioia/Univ. of Hawaii and NASA

tion $g_{\rm ff}$ is called Gaunt-factor; it is a quantum mechanical correction factor of order 1, or, more precisely,

$$g_{\rm ff} \approx \frac{3}{\sqrt{\pi}} \ln\left(\frac{9k_{\rm B}T}{4h_{\rm P}\nu}\right) .$$

Hence, the spectrum described by (6.31) is flat for $h_{\rm P}\nu \ll k_{\rm B}T$, and exponentially decreasing for $h_{\rm P}\nu \gtrsim k_{\rm B}T$, as is displayed in Fig. 6.22.

The temperature of the gas in massive clusters is typically $T \sim 5 \times 10^7\,{\rm K}$, or $k_{\rm B}T \sim 5\,{\rm keV}$—X-ray astronomers usually specify temperatures and frequencies in keV (see Appendix C). For a thermal plasma with Solar abundances, the total bremsstrahlung emission is

$$\epsilon^{\rm ff} = \int_0^\infty {\rm d}\nu \epsilon_\nu^{\rm ff} \approx 3.0 \times 10^{-27} \sqrt{\frac{T}{1\,{\rm K}}} \left(\frac{n_{\rm e}}{1\,{\rm cm}^{-3}}\right)^2 {\rm erg\,cm^{-3}s^{-1}} . \tag{6.32}$$

Line emission. The assumption that the X-ray emission originates from a hot, diffuse gas (intracluster medium, ICM) was confirmed by the discovery of line emission in the X-ray spectrum of clusters. One of the most prominent lines in massive clusters is located at energies just below 7 keV: it is the Lyman-α ("Kα") line of 25-fold ionized iron (thus, of an iron nucleus with only a single electron). Slightly less ionized iron has a strong transition at somewhat lower energies of $E \sim 6.4\,{\rm keV}$. Later, other lines were also discovered in the X-ray spectrum of clusters. As a rule, the hotter the gas is, thus the more completely ionized it is, the weaker the line emission. The X-ray emission of clusters with relatively low temperatures, $k_{\rm B}T \lesssim 2\,{\rm keV}$, is sometimes dominated by line emission from highly ionized atoms (C, N, O, Ne, Mg, Si, S, Ar, Ca, and a strong line complex of iron at $E \sim 1\,{\rm keV}$—see Fig. 6.22). The emissivity of a thermal plasma with Solar abundance and temperatures in the range $10^5\,{\rm K} \lesssim T \lesssim 4 \times 10^7\,{\rm K}$ can roughly be approximated by

$$\epsilon \approx 6.2 \times 10^{-19} \left(\frac{T}{1\,{\rm K}}\right)^{-0.6} \left(\frac{n_{\rm e}}{1\,{\rm cm}^{-3}}\right)^2 {\rm erg\,cm^{-3}\,s^{-1}} . \tag{6.33}$$

Equation (6.33) accounts for free-free emission as well as line emission. Compared to (6.32), one finds a different dependence on temperature: while the total emissivity for bremsstrahlung is $\propto T^{1/2}$, it increases again towards lower temperatures where the line emission becomes more important (see also Fig. 10.3 for the temperature dependence of the emissivity of a gas). It should be noted in particular that the emissivity depends quadratically on the density of the plasma, since both bremsstrahlung and the collisional excitation responsible for line emission are two-body processes. Thus in order to estimate the mass of the hot gas from its X-ray luminosity, the spatial distribution of the gas needs to be known. For example, if the gas in a cluster is locally inhomogeneous, the value of $\langle n_{\rm e}^2 \rangle$ which determines the X-ray emissivity may deviate significantly from $\langle n_{\rm e} \rangle^2$. As we will see later, clusters of galaxies satisfy a number of scaling relations, and one relation between the gas mass and the X-ray luminosity is found empirically, from which the gas mass can be estimated. One finds that the mass in the intracluster gas is about five to ten times larger than the mass of the stars in the galaxies, where this ratio slightly increases with increasing cluster mass.

Morphology of the X-ray emission. From the morphology of their X-ray emission, one can roughly distinguish between

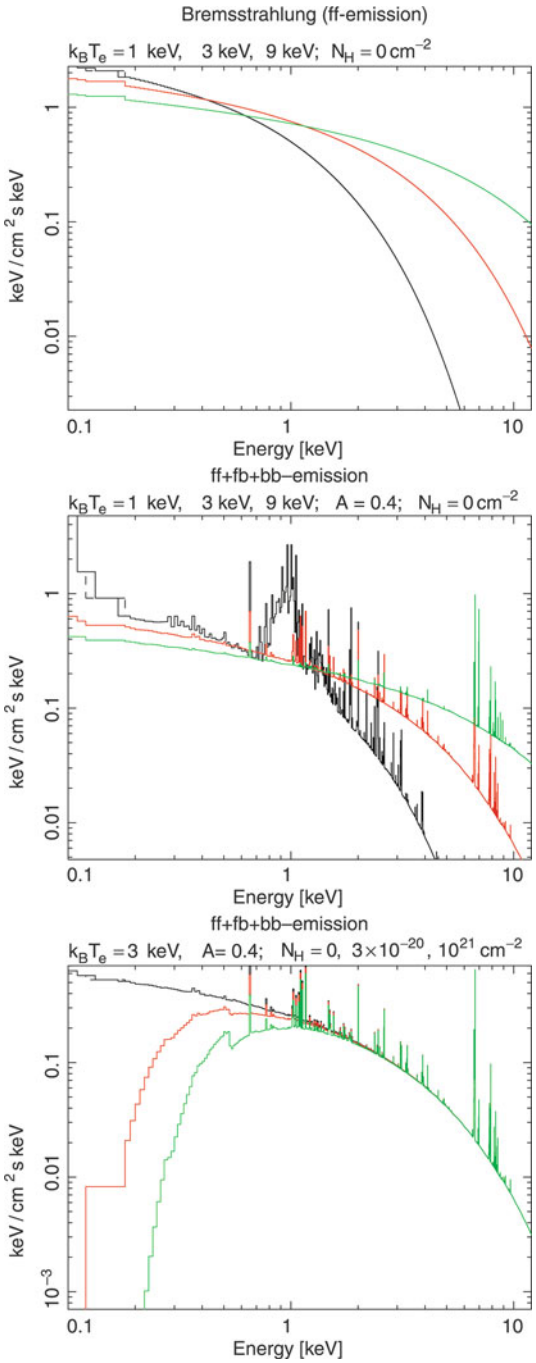

Fig. 6.22 X-ray emission of an optically thin hot plasma. In the *top panel*, the bremsstrahlung spectrum is shown, for three different gas temperatures; the radiation of hotter gas extends to higher photon energies, and above $E \sim k_B T$ the spectrum is exponentially cut off. In the central panel, atomic transitions and recombination radiation in the hot gas are also taken into account, where a metallicity of 40 % of the Solar value is assumed. These additional radiation mechanisms become more important towards lower T, as can be seen from the $T = 1$ keV curve. In the *bottom panel*, photo-electric absorption by the Galactic interstellar medium is included, with different column densities in hydrogen; for this gas, Solar metallicity is assumed. The Galactic absorption produces a cut-off in the spectrum towards lower energies. Credit: T. Reiprich, Argelander-Institut für Astronomie, Universität Bonn

regular and irregular clusters, as is also done in the classification of the galaxy distribution. In Fig. 6.23, X-ray surface brightness contours are superposed on optical images of four galaxy clusters or groups, covering a wide range of cluster mass and X-ray temperature. Regular clusters show a smooth brightness distribution, centered on the optical center of the cluster, and an outwardly decreasing surface brightness. In contrast, irregular clusters may have several brightness maxima, often centered on cluster galaxies or subgroups of cluster galaxies.

Typically, regular clusters have an X-ray luminosity L_X and temperature that smoothly increases with cluster mass. In contrast, irregular clusters at a given mass can be either hotter or cooler than regular clusters. Irregular clusters are the result of a recent merging event, and their temperature depends on the stage of the merging process. In the initial phases of the merger, the kinetic energy is not yet thermalized, and thus the gas remains at approximately the same temperature it had before the merging event. Later on, the gas is heated by shock fronts in which the kinetic energy is transformed into internal energy of the gas—i.e., heat. In this phase, the gas temperature can be higher than that of a regular cluster of the same mass. Finally, the cluster settles into an equilibrium state. Indications of past merger events can be seen in substructures of the X-ray emitting gas; even for the Coma cluster, which is frequently considered a typical example of a relaxed cluster, signs of previous merger events can be detected, as shown in Fig. 6.24.

The trend emerges that in clusters with a larger fraction of spiral galaxies, L_X and T are lower. Irregular clusters typically also have a lower central density of galaxies and gas compared to regular clusters. Clusters of galaxies with a dominant central galaxy often show a strong central peak in X-ray emission. The X-ray emission often deviates from axial symmetry, so that the assumption of clusters being roughly spherically symmetric is not well founded in these cases.

6.4.2 Models of the X-ray emission

Hydrostatic assumption. To draw conclusions about the properties of the intergalactic (intra-cluster) medium from the observed X-ray radiation and about the distribution of mass in the cluster, the gas distribution needs to be modeled. In fact, as we shall see below, assuming the geometry of the cluster (e.g., spherical symmetry), the radial dependence of the gas density can be directly reconstructed. For this, we first consider the speed of sound in the cluster gas,

$$c_s \approx \sqrt{\frac{P}{\rho_g}} = \sqrt{\frac{nk_BT}{\rho_g}} = \sqrt{\frac{k_BT}{\mu m_p}} \sim 1000\,\mathrm{km\,s^{-1}}\,,$$

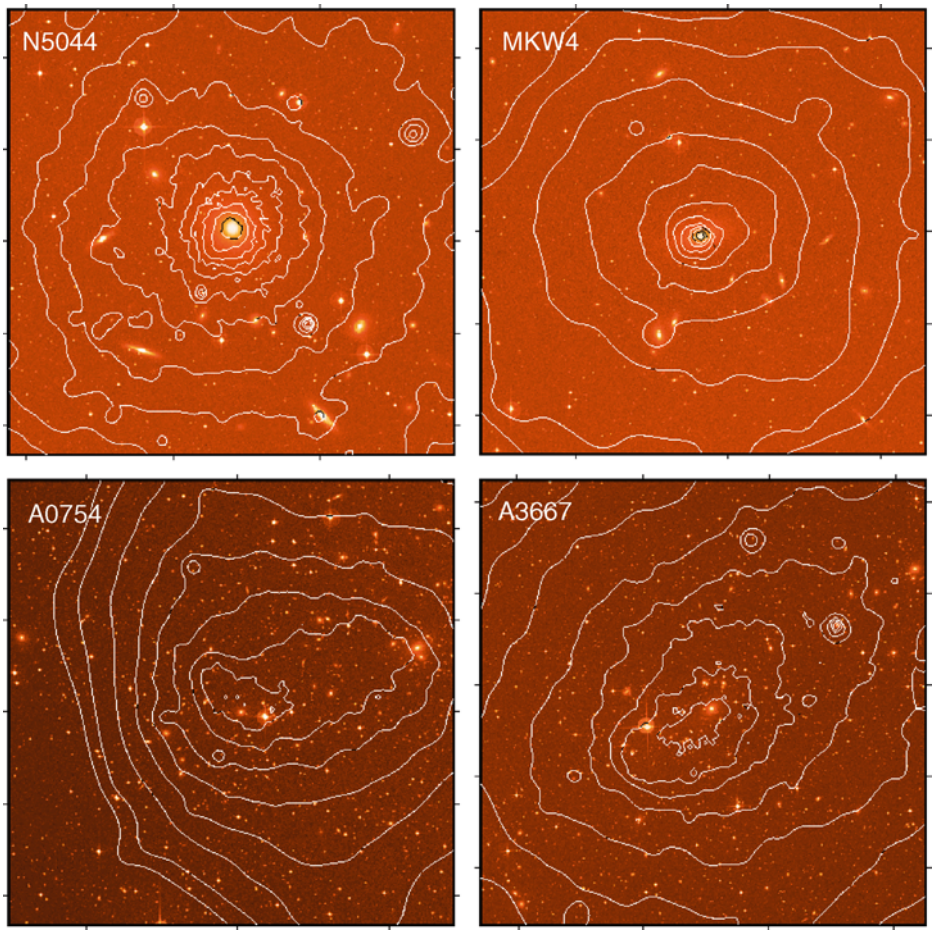

Fig. 6.23 Surface brightness contours of the X-ray emission for four different groups or clusters of galaxies. Each image is about 30′ on a side. *Upper left*: the galaxy group NGC 5044, at redshift $z = 0.009$, with an X-ray temperature of $T \approx 1.07\,\mathrm{keV}$ and a virial mass of $M_{200} \approx 0.32h^{-1} \times 10^{14} M_\odot$. *Upper right*: the group MKW4, at $z = 0.02$, with $T \approx 1.71\,\mathrm{keV}$ and $M_{200} \approx 0.5h^{-1} \times 10^{14} M_\odot$. *Lower left*: the cluster of galaxies A 0754, at $z = 0.053$, with $T \approx 9.5\,\mathrm{keV}$ and $M_{200} \approx 13.1h^{-1} \times 10^{14} M_\odot$. *Lower right*: the cluster of galaxies A 3667, at $z = 0.056$, with $T \approx 7.0\,\mathrm{keV}$ and $M_{200} \approx 5.6h^{-1} \times 10^{14} M_\odot$. The X-ray data were obtained by ROSAT, and the optical images were taken from the Digitized Sky Survey. These clusters are part of the HIFLUGCS survey, which we will discuss more thoroughly in Sect. 6.4.5. Credit: T. Reiprich, Argelander-Institut für Astronomie, Universität Bonn

where P denotes the gas pressure, ρ_g the gas density, and n the number density of gas particles. Then, the *average molecular mass* is defined as the average mass of a gas particle in units of the proton mass,

$$\mu := \frac{\langle m \rangle}{m_\mathrm{p}} \,, \tag{6.34}$$

so that $\rho_\mathrm{g} = n \langle m \rangle = n\mu m_\mathrm{p}$. For a gas of fully ionized hydrogen, one gets $\mu = 1/2$ because in this case one has one proton and one electron per ∼proton mass. The cluster gas also contains helium and heavier elements; accounting for them yields $\mu \sim 0.60$. The sound-crossing time for the cluster is

$$t_\mathrm{sc} \approx \frac{2R_\mathrm{A}}{c_\mathrm{s}} \sim 7 \times 10^8\,\mathrm{yr} \,,$$

and is thus, for a cluster with $T \sim 10^8\,\mathrm{K}$, significantly shorter than the lifetime of the cluster, which can be approximated roughly by the age of the Universe. Since the sound-crossing time defines the time-scale on which deviations from the pressure equilibrium are evened out, the gas can be in hydrostatic equilibrium, provided that the last major merging event happened longer ago than the sound-crossing time. In this case, the equation

$$\boxed{\nabla P = -\rho_\mathrm{g} \nabla \Phi} \tag{6.35}$$

applies, with Φ denoting the gravitational potential. Equation (6.35) describes how the gravitational force is balanced by the pressure force. In the spherically symmetric case in which all quantities depend only on the radius r, we obtain

$$\frac{1}{\rho_\mathrm{g}} \frac{\mathrm{d}P}{\mathrm{d}r} = -\frac{\mathrm{d}\Phi}{\mathrm{d}r} = -\frac{GM(r)}{r^2} \,, \tag{6.36}$$

where $M(r)$ is the mass enclosed within radius r. Here, $M(r)$ is the total enclosed mass, i.e., not just the gas mass, because the potential Φ is determined by the total mass. Note the similarity of this equation with (6.9), except that there P described the dynamical pressure of the galaxies or dark matter particles. By inserting $P = nk_\mathrm{B}T = \rho_\mathrm{g} k_\mathrm{B} T/(\mu m_\mathrm{p})$ into (6.36), we obtain

$$\boxed{M(r) = -\frac{k_\mathrm{B} T r^2}{G\mu m_\mathrm{p}} \left(\frac{\mathrm{d} \ln \rho_\mathrm{g}}{\mathrm{d}r} + \frac{\mathrm{d} \ln T}{\mathrm{d}r} \right)} \,. \tag{6.37}$$

Fig. 6.24 In *white*, on optical image of the Coma cluster is shown. Superposed on this SDSS image is the X-ray emission, shown in *pink*, where the smooth component of the X-ray image was subtracted to highlight the filamentary structure of the hot gas. These filaments are most likely due to a past merger events, when smaller groups fall into the main cluster; their gas was stripped by ram-pressure during infall, leaving trails of gas. The sidelength of the image is 23′, corresponding to about 600 kpc. Credit: X-ray: NASA/CXC/MPE/J. Sanders et al., Optical: SDSS

This equation is of central importance for the X-ray astronomy of galaxy clusters because it shows that we can derive the mass profile $M(r)$ from the radial profiles of ρ_g and T. Thus, if one can measure the density and temperature profiles, the mass of the cluster, and hence the total density, can be determined as a function of radius.

However, these measurements are not without difficulties. $\rho_\mathrm{g}(r)$ and $T(r)$ need to be determined from the X-ray luminosity and the spectral temperature, using the bremsstrahlung emissivity (6.31). Obviously, they can be observed only in projection in the form of the surface brightness

$$I_\nu(R) = 2\int_R^\infty \mathrm{d}r\ \frac{\epsilon_\nu(r)\,r}{\sqrt{r^2-R^2}}\,, \tag{6.38}$$

from which the emissivity, and thus density and temperature, need to be derived by de-projection, i.e., the inversion of (6.38) to obtain $\epsilon_\nu(r)$ in terms of $I_\nu(R)$. Furthermore, the angular and energy resolution of X-ray telescopes prior to XMM-Newton and Chandra were not high enough to measure both $\rho_\mathrm{g}(r)$ and $T(r)$ with sufficient accuracy, except for the nearest clusters. For this reason, the mass determination was often performed by employing additional, simplifying assumptions.

Isothermal gas distribution. From the radial profile of $I(R)$, $\epsilon(r)$ can be derived by inversion of (6.38). Since the spectral bremsstrahlung emissivity depends only weakly on T for $h_\mathrm{P}\nu \ll k_\mathrm{B}T$—see (6.31)—the radial profile of the gas density ρ_g can be derived from $\epsilon(r)$. The X-ray satellite ROSAT was sensitive to radiation of $0.1\,\mathrm{keV} \lesssim E \lesssim 2.4\,\mathrm{keV}$, so that the X-ray photons detected by it are typically from the regime where $h_\mathrm{P}\nu \ll k_\mathrm{B}T$.

Assuming that the gas temperature is spatially constant, $T(r) = T_\mathrm{g}$, (6.37) simplifies, and the mass profile of the cluster can be determined from the density profile of the gas.

The β-model. A commonly used method consists of fitting the X-ray data by a so-called β-model. This model is based on the assumption that the density profile of the total matter (dark and luminous) is described by an isothermal distribution, i.e., it is assumed that the temperature of the gas is independent of radius, and at the same time that the mass distribution in the cluster is described by the isothermal model that was discussed in Sect. 6.3.1. With (6.9) and (6.12), we then obtain for the total density $\rho(r)$

$$\frac{\mathrm{d}\ln\rho}{\mathrm{d}r} = -\frac{1}{\sigma_v^2}\,\frac{GM(r)}{r^2}\,. \tag{6.39}$$

On the other hand, in the isothermal case (6.37) reduces to

$$\frac{\mathrm{d}\ln\rho_\mathrm{g}}{\mathrm{d}r} = -\frac{\mu m_\mathrm{p}}{k_\mathrm{B}T_\mathrm{g}}\,\frac{GM(r)}{r^2}\,. \tag{6.40}$$

The comparison of (6.39) and (6.40) then shows that $\mathrm{d}\ln\rho_\mathrm{g}/\mathrm{d}r \propto \mathrm{d}\ln\rho/\mathrm{d}r$, or

$$\rho_\mathrm{g}(r) \propto [\rho(r)]^\beta \quad \text{with} \quad \boxed{\beta := \frac{\mu m_\mathrm{p}\sigma_v^2}{k_\mathrm{B}T_\mathrm{g}}} \tag{6.41}$$

must apply; thus the gas density follows the total density to some power. Here, the index β depends on the ratio of the dynamical temperature, measured by σ_v, and the gas temperature. Now, using the King approximation for an isothermal mass distribution—see (6.17)—as a model for the mass distribution, we obtain

$$\boxed{\rho_\mathrm{g}(r) = \rho_{\mathrm{g}0}\left[1+\left(\frac{r}{r_\mathrm{c}}\right)^2\right]^{-3\beta/2}}\,, \tag{6.42}$$

where $\rho_{\mathrm{g}0}$ is the central gas density. The brightness profile of the X-ray emission in this model is then, according to (6.38),

$$\boxed{I(R) \propto \left[1+\left(\frac{R}{r_\mathrm{c}}\right)^2\right]^{-3\beta+1/2}}\,. \tag{6.43}$$

The X-ray emission of many clusters is well described by this profile,[7] yielding values for r_c of 0.1 to $0.3h^{-1}$ Mpc and a value for the index $\beta = \beta_{\rm fit} \approx 0.65$. Alternatively, β can be measured, with the definition given in (6.41), from the gas temperature T_g and the velocity dispersion of the galaxies σ_v, which yields typical values of $\beta = \beta_{\rm spec} \approx 1$. Such a value would also be expected if the mass and gas distributions were both isothermal. In this case, they should have the same temperature, which was presumably determined by the formation of the cluster.

The β-discrepancy. The fact that the two values for β determined above differ from each other (the so-called β-discrepancy) is almost certainly due to the fact that the β-model is too simple. We can see, e.g., from Fig. 6.25 that the gas distribution, at least in the inner part of clusters, does not follow a smooth distribution, nor is its temperature constant. The latter is also reflected by the fact that the measured values for $\beta_{\rm fit}$ often depend on the angular range over which the brightness profile is fitted: the larger this range, the larger $\beta_{\rm fit}$ becomes, and thus the smaller the discrepancy. This behavior can be understood if the central region of the clusters have a lower temperature than at larger radii. Furthermore, temperature measurements of clusters are often not very accurate because it is the emission-weighted temperature which is measured, which is, due to the quadratic dependence of the emissivity on ρ_g, dominated by the regions with the highest gas density. The fact that the innermost regions of clusters where the gas density is highest tend to have a temperature below the bulk temperature of the cluster (see Fig. 6.26) may lead to an underestimation of 'the' cluster temperature. In addition, the near independence of the spectral form of $\epsilon_\nu^{\rm ff}$ from T for $h_{\rm P}\nu \ll k_{\rm B}T$ renders the measurement of T difficult. Chandra and XMM-Newton can measure the X-ray emission at energies of up to $E \lesssim 10\,$keV, which resulted in considerably improved temperature determinations.

Such investigations have revealed that the temperature behavior shown in Fig. 6.26 is typical for many clusters: The temperature decreases towards the center and towards the edge, while it is rather constant over a larger range at intermediate radii. Many clusters are found, however, in which the temperature distribution is by no means radially symmetric, but shows distinct substructure. Finally, as another possible explanation for the β-discrepancy, it should be mentioned that the velocity distribution of those galaxies from which σ_v is measured may be anisotropic.

[7] We point out that the pair of (6.42) and (6.43) is valid independently of the validity of the assumptions from which (6.42) was obtained. If the observed X-ray emission is very well described by (6.43), the gas density profile (6.42) can be obtained from it, independently of the validity of the assumptions made before.

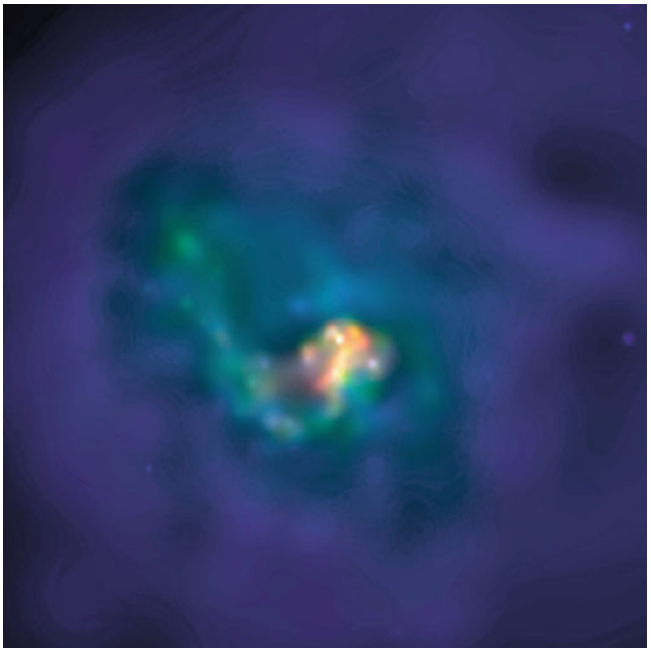

Fig. 6.25 Chandra image of the Centaurus cluster; the size of the field is $3' \times 3'$. Owing to the excellent angular resolution of the Chandra satellite, the complexity of the morphology in the X-ray emission of clusters can be analyzed. *Colors* indicate photon energies, from low to high in *red*, *yellow*, *green*, and *blue*. The gas in the center of the cluster is significantly cooler than that at larger radii. Credit: NASA/IoA/J. Sanders & A. Fabian

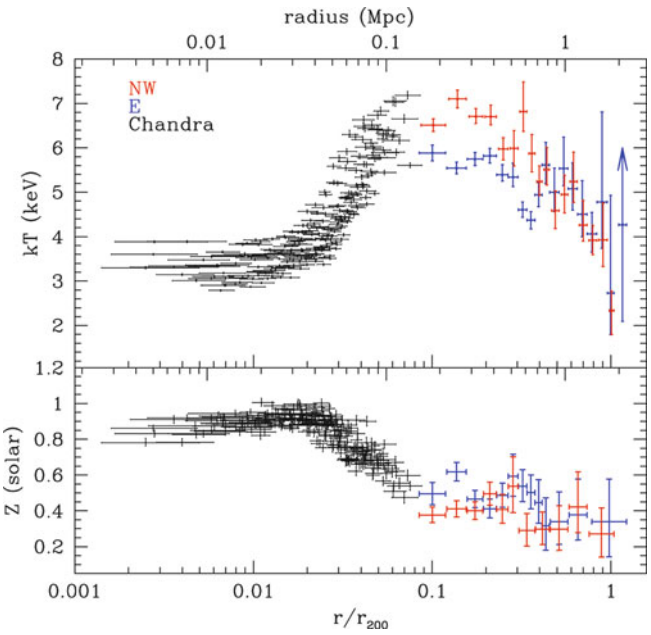

Fig. 6.26 Temperature (*top*) and metallicity (*bottom*) profile of the Perseus cluster, measured along two different directions from the cluster center outwards. *Black symbols* show measurements in the inner region, obtained with Chandra. The *colored points* are obtained from Suzaku data, with each color corresponding to one radial direction. Source: A. Simionescu et al. 2011, *Baryons at the Edge of the X-ray-Brightest Galaxy Cluster*, Science 331, 1576, Fig. 2. Reprinted with permission from AAAS

Besides all the uncertainty as to the validity of the β-model, we also need to mention that numerical simulations of galaxy clusters, which take dark matter and gas into account, have repeatedly come to the conclusion that the mass determination of clusters, utilizing the β-model, should achieve an accuracy of better than $\sim 20\,\%$, although different gas dynamical simulations have arrived at distinctly different results.

Dark matter in clusters from X-ray observations. Based on measurements of their X-ray emission, a mass estimate can be performed for galaxy clusters. It is found, in agreement with the dynamical method, that clusters contain much more mass than is visible in galaxies. The total mass of the intergalactic medium is clearly too low to account for the missing mass; its gas mass is only $\sim 15\,\%$ of the total mass of a cluster.

Only $\sim 3\,\%$ of the mass in clusters of galaxies is due to stars in galaxies, and about 15% is contributed by the intergalactic gas, whereas the remaining $\sim 80\,\%$ consists of dark matter which therefore dominates the mass of the clusters.

6.4.3 Cooling "flows"

Expected consequences of gas cooling. In examining the intergalactic medium, we assumed hydrostatic equilibrium, but we disregarded the fact that the gas cools by its emission and by that loses internal energy. For this reason, once established, a hydrostatic equilibrium in principle cannot be maintained over arbitrarily long times. To decide whether this gas cooling is important for the dynamics of the system, the cooling time-scale needs to be considered. This cooling time turns out to be very long,

$$t_{\rm cool} := \frac{u}{\epsilon^{\rm ff}} \approx 8.5 \times 10^{10}\,{\rm yr} \left(\frac{n_{\rm e}}{10^{-3}\,{\rm cm}^{-3}}\right)^{-1} \left(\frac{T_{\rm g}}{10^8\,{\rm K}}\right)^{1/2} , \tag{6.44}$$

where $u = (3/2) n k_{\rm B} T_{\rm g}$ is the energy density of the gas and $n_{\rm e}$ the electron density. Hence, the cooling time is longer than the Hubble time nearly everywhere in the cluster, which allows a hydro*static* equilibrium to be established to a very good approximation. In the centers of clusters, however, the density may be sufficiently large to yield $t_{\rm cool} \lesssim t_0 \sim H_0^{-1}$. Here, the gas can cool quite efficiently, by which its pressure decreases. This then implies that, at least close to the center, the hydrostatic equilibrium can no longer be maintained. To re-establish pressure equilibrium, gas needs to flow inwards and is thus compressed. Hence, an inward-directed mass flow should establish itself. The corresponding density increase will further accelerate the cooling process. Since, in addition, the emissivity (6.33) of a relatively cool gas increases with decreasing temperature, this process should then very quickly lead to a strong compression and cooling of the gas in the centers of dense clusters. It is a process which, once started, will accelerate and quickly lead to the cooling down to very low temperatures. In parallel to this increase in density, the X-ray emission should strongly increase, because $\epsilon^{\rm ff} \propto n_{\rm e}^2$. As a result of this process, a radial density and temperature distribution should be established with a nearly unchanged pressure distribution. In Fig. 6.25, the cooler gas in the center of the Centaurus cluster is clearly visible.

Some predictions of this so-called *cooling flow* model have indeed been verified observationally. In the centers of many massive clusters, one observes a sharp central peak in the surface brightness $I(R)$. However, we need to stress that, as yet, no inwards *flows* have been measured. Such a measurement would be very difficult, though, due to the small expected velocities. The amount of cooling gas can be considerable. We can estimate the mass rate $\dot{M}$ at which the gas should cool and flow inwards due to this cooling. The internal energy U of the gas is related to its mass M by $U = M\,u/\rho$, with u as given above. The loss of this energy due to cooling is the luminosity, $L = \dot{U}$, so that

$$\dot{M} \sim \frac{L\,\rho}{u} \sim \frac{L \mu m_{\rm p}}{k_{\rm B} T_{\rm g}} . \tag{6.45}$$

For some massive clusters, this estimate lead to cooling rates of tens or even hundreds of Solar masses per year. However, after spectroscopic observations by XMM-Newton became available, we have learned that these very high cooling rates implied by the models were *significantly* overestimated.

The fate of the cooling gas. The gas cooling in this way will accumulate in the center of the cluster, but despite the expected high mass of cold gas, no clear evidence has been found for it. In clusters harboring a cD galaxy, the cooled gas may, over a Hubble time, contribute a considerable fraction of the mass of this galaxy. Hence, the question arises whether cD galaxies may have formed by accretion in cooling flows. In this scenario, the gas would be transformed into stars in the cD galaxy. However, the star-formation rate in these central galaxies is much lower than the rate by which cluster gas cools, according to the 'old' cooling flow models sketched above.

The absence of massive cooling flows. The sensitivity and spectral resolution achieved with XMM-Newton have strongly modified our view of cooling flows. In the standard model of cooling flows, the gas cools from the cluster temperature down to temperatures significantly below 1 keV.

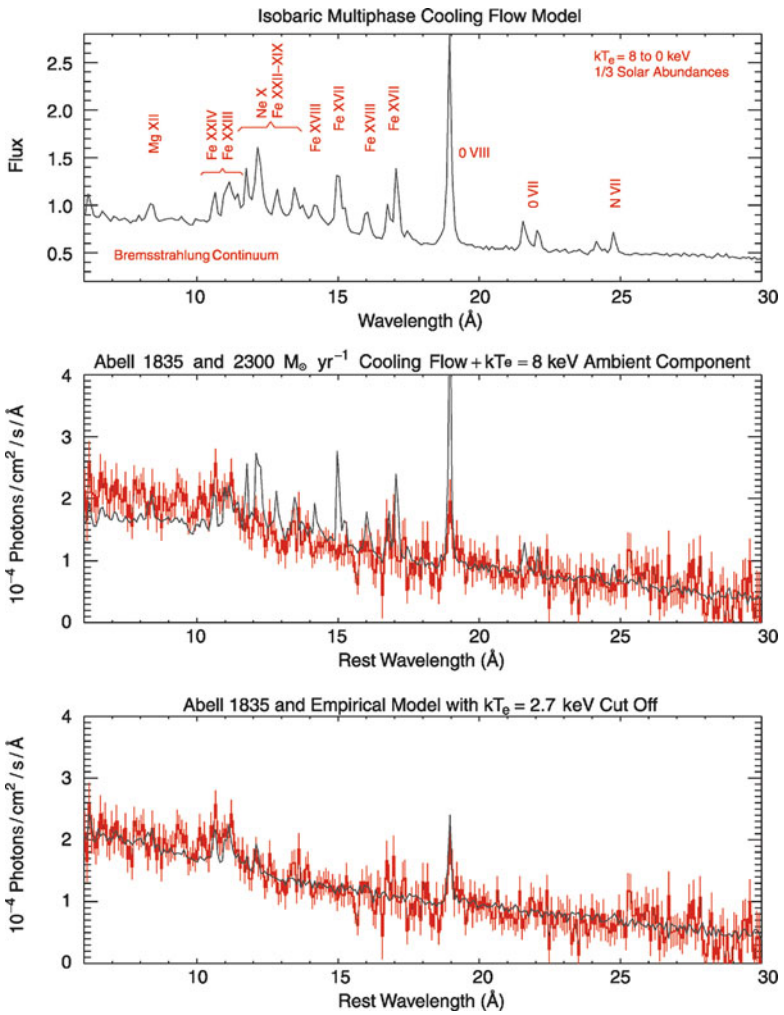

Fig. 6.27 In the *top panel*, a model spectrum of a cooling flow is shown, in which the gas cools down from 8 keV to $T_g = 0$. The strong lines of FeXVII can be seen. In the *central panel*, the spectrum of Abell 1835 is superposed on the model spectrum; clear discrepancies are visible, especially the absence of strong emission lines from FeXVII. If the gas is not allowed to cool down to temperatures below 3 keV (*bottom panel*), the agreement with observation improves visibly. Source: J.R. Peterson et al. 2003, *High Resolution X-ray Spectroscopic Constraints on Cooling-Flow Models*, astro-ph/0310008, Fig. 2. Reproduced by permission of the author

In this process many atomic lines are emitted, produced by various ionization stages, e.g., of iron, which strongly depend on temperature. Figure 6.27 (top panel) shows the expected spectrum of a cooling flow in which the gas cools down from the cluster temperature of $T_g \approx 8$ keV to essentially $T_g = 0$, where a chemical composition of 1/3 Solar abundance is assumed. In the central panel, this theoretical spectrum is compared with the spectrum of the cluster Abell 1835, where very distinct discrepancies become visible. In the bottom panel, the model was modified such that the gas cools down only to $T_g = 3$ keV; this model clearly matches the observed spectrum better.

Hence, cooler gas in the inner regions of clusters is directly detected spectroscopically. However, the temperature measurements from X-ray spectroscopy are significantly different from the prediction of the cooling flow model according to which drastic cooling should take place in the gas, because the process of compression and cooling will accelerate for ever decreasing T_g. Therefore, one expects to find gas at all temperatures lower than the temperature of the cluster. But this seems not to be the case: whereas the central temperature can be considerably smaller than that at larger radii (see, e.g., Fig. 6.26), no gas seems to be present at very small temperatures, although the cooling flow model predicts the existence of such gas. A minimum temperature seems to exist, below which the gas cannot cool, or the amount of gas that cools to $T_g \sim 0$ is considerably smaller than expected from the cooling flow model. This lower mass rate of gas that cools down completely would then also be compatible with the observed low star-formation rates in the central galaxies of clusters. In fact, a correlation between the cooling rate of gas as determined from XMM observations and the regions of star formation in clusters has been found (see Fig. 6.28). About 50 % of X-ray luminous clusters show an infrared excess of the BCG, indicating ongoing star formation; furthermore, whereas the BCG in clusters with long cooling time rarely show optical emission lines, most of those in cooling flow clusters do. All these are clear indications that a few percent of the cooling mass rate (6.45) as estimated from the cooling flow model indeed arrive at the central cluster galaxy.

There may be exceptional cases where a larger fraction of the cooling gas can reach the gravitational center of the cluster and cool down to low temperatures. Recently,

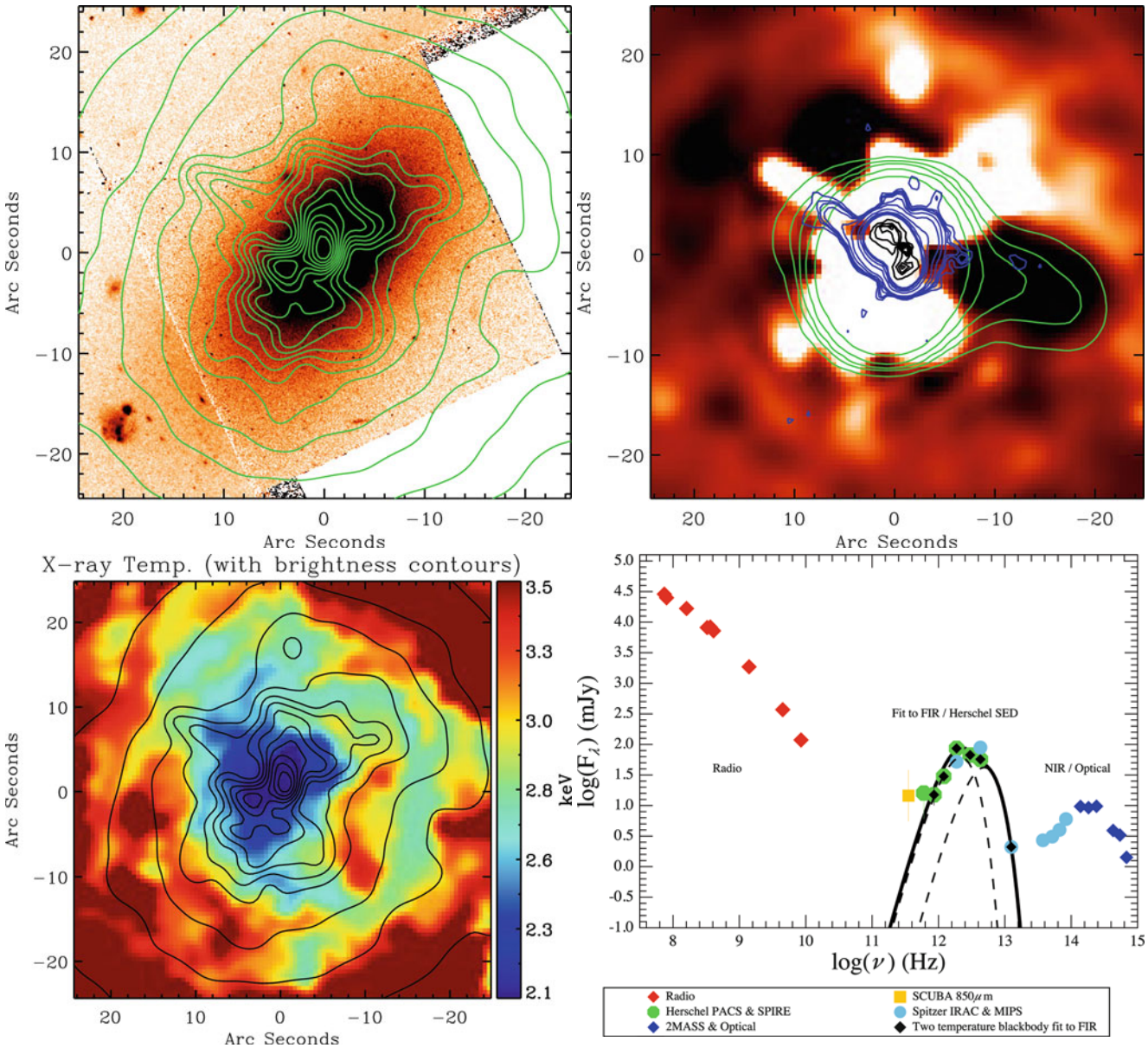

Fig. 6.28 The cool-core cluster Abell 2597 at $z = 0.082$. The *upper left panel* shows the Chandra X-ray map as green contours, superposed on an optical image of the brightest cluster galaxy (BCG) of this cluster. Note that the overall orientation of the X-ray emission follows that of the light in the BCG. *Upper right*: The color map is obtained from subtracting a smoothed version of the X-ray emission from the one shown in the *left panel*; this so-called 'unsharp mask' image highlights the small-scale brightness variations. Superposed on this are radio contours at three different frequencies, increasing *from green to blue to black*. Clearly, the BCG contains an active nucleus, and the radio jet apparently causes an X-ray cavity on the right of the galaxy center. The *lower left panel* shows the temperature map, as obtained from resolved X-ray spectroscopy, with the total X-ray emission superposed. The temperature in the inner part is markedly smaller than at larger radii, a clear sign of a cool core. Note also the small-scale structure in the temperature map. The spectral energy distribution of the core, shown at the *lower right*, yields a clear indication of ongoing star formation, seen from the far-IR radiation due to warm dust. Further indications for ongoing star formation is obtained from the UV-radiation, as well as emission lines of the object (not shown). Source: *Upper* and *lower right panels*: G.R. Tremblay et al. 2012, *Residual cooling and persistent star formation amid active galactic nucleus feedback in Abell 2597*, MNRAS 424, 1042, p. 1046, 1053, Figs. 1, 4. Lower left panel: G.R. Tremblay et al. 2012, *Multiphase signatures of active galactic nucleus feedback in Abell 2597*, MNRAS 424, 1026, p. 1036, Fig. 7. Reproduced by permission of Oxford University Press on behalf of the Royal Astronomical Society

a cluster at $z \sim 0.6$ was discovered with an extremely large cooling mass rate $\dot{M} \sim 4000 M_\odot/\mathrm{yr}$ where the BCG shows signs of massive star formation, estimated to be $\sim 700 M_\odot/\mathrm{yr}$. Such cases are rare, however, and may be a transitional state in the cluster evolution.

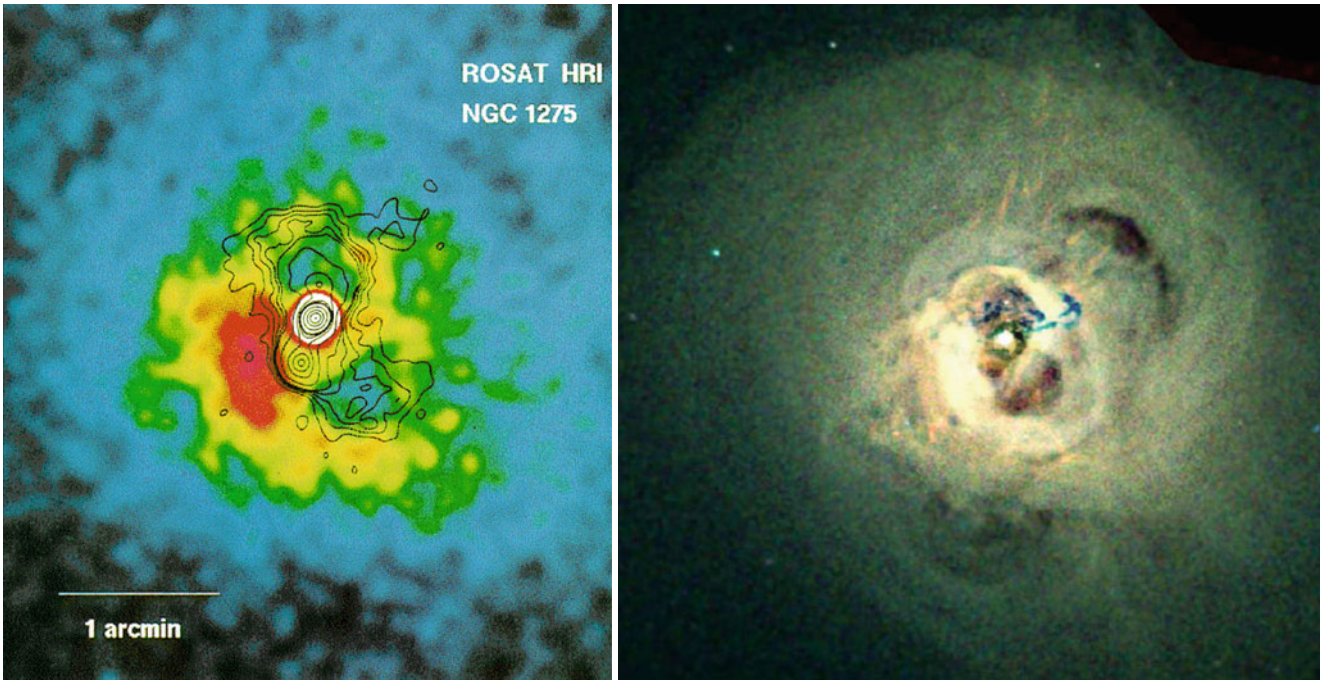

Fig. 6.29 The central region of the Perseus cluster. The *left panel* shows a color-coded X-ray image, taken with ROSAT, with radio contours superposed. The radio emission stems from the central galaxy of the cluster, the radio galaxy NGC 1275 (also called Perseus A). Clearly identifiable is the effect of the radio jets on the X-ray emission—at the location of the radio lobes the X-ray emission is strongly suppressed. The *right panel* shows a slightly larger region in X-rays, taken with the considerably better resolution of Chandra. The fine structure of the X-ray gas is much better recognized here. In addition to the two cavities overlapping with the radio emission, another pair of bubbles at larger distance from the center is seen. The high X-ray luminosity and small distance from us allows a very detailed analysis of this cluster. In particular, sound waves in the X-ray gas can be identified which probably are due to earlier activity of the central black hole. The blue filaments near the center indicates hard X-ray emission; the hardening of the observed spectrum is due to an infalling galaxy at high velocity, whose interstellar medium absorbs the low-energy X-ray photons. Credit: *Left*: H. Böhringer, MPE. *Right*: NASA/CXC/IoA/A. Fabian et al.

Cool-core clusters. Not all clusters show indications for a cool inner region with a strongly peaked X-ray emission. If clusters are far from an equilibrium state, for example due to a recent merger or infall of a group, the gas will be far from a quasi-steady state, and the foregoing consideration will not apply, not even approximately. Strong mixing of the gas by turbulent motions, or shock fronts which develop when the intracluster medium of two colliding or merging clusters intersect, will prevent the development of a cool, condensed central region. One thus distinguishes between *cool-core clusters* and non-cool-core clusters. The former ones are expected to be close to hydrostatic equilibrium, whereas the latter ones may deviate from it strongly.

What prevents massive cooling flows? One way to explain the clearly suppressed cooling rates in cooling flows is by noting that many clusters of galaxies harbor an active galaxy in their center. In most cases, this AGN is not a luminous quasar, but radio galaxies are the most common type of AGNs in the BCG of clusters, the activity of which, e.g., in the form of (radio-)jets, may affect the ICM. For instance, energy could be transferred from the jet to the ICM, by which the ICM is heated. This heating might then prevent the temperature from dropping to arbitrarily small values. This hypothesis is supported by the fact that many clusters are known in which the ICM is clearly affected by the central AGN—see Fig. 6.29 for one of the first examples where this effect was seen, and Fig. 6.30 where two active nuclei are detected. In the cluster Abell 2597 shown in Fig. 6.28 the interaction of the radio source with the intracluster gas is also clearly seen. Plasma from the jet seems to locally displace the X-ray emitting gas. By friction and mixing in the interface region between the jet and the ICM, the latter is certainly heated. It is unclear, though, whether this explanation is valid for every cluster, because not every cluster in which a very cool ICM is expected also contains an observed AGN. On the other hand, this is not necessarily an argument against the hypothesis of AGNs as heating sources, since AGNs often have a limited time of activity and may be switching on and off, depending on the accretion rate. Thus, the gas in a cluster may very well be heated by an AGN even if it is currently (at the time of observation) inactive. Evidence for the occurrence of this effect also in galaxy groups is shown in Fig. 6.31.

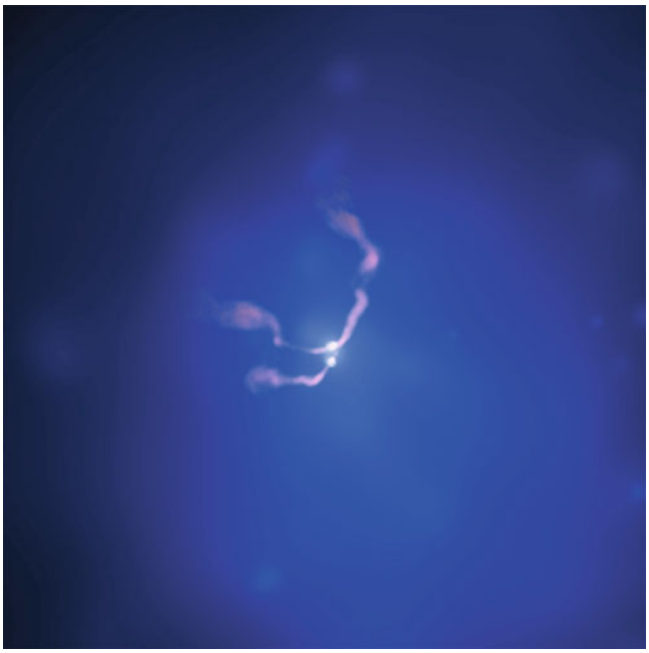

Fig. 6.30 A composite X-ray (*blue*, taken by Chandra) and radio (*pink*, VLA) image of the galaxy cluster Abell 400. The radio jets are launched by a binary supermassive black hole in the center of the galaxy NGC 1128, also known as 3C 75, a wide angle tailed radio source. The energy of the jets is partly transferred to the hot intracluster medium, which is thereby heated. The strong curvature of the jets is caused by the relative motion of the galaxy through the ICM, i.e., the jets are 'pushed back' by ram pressure. With a (projected) separation of about 8 kpc, this is one of the closest supermassive black hole binary system known. Credit: X-ray: NASA/CXC/AIfA/D. Hudson & T. Reiprich et al.; Radio: NRAO/VLA/NRL

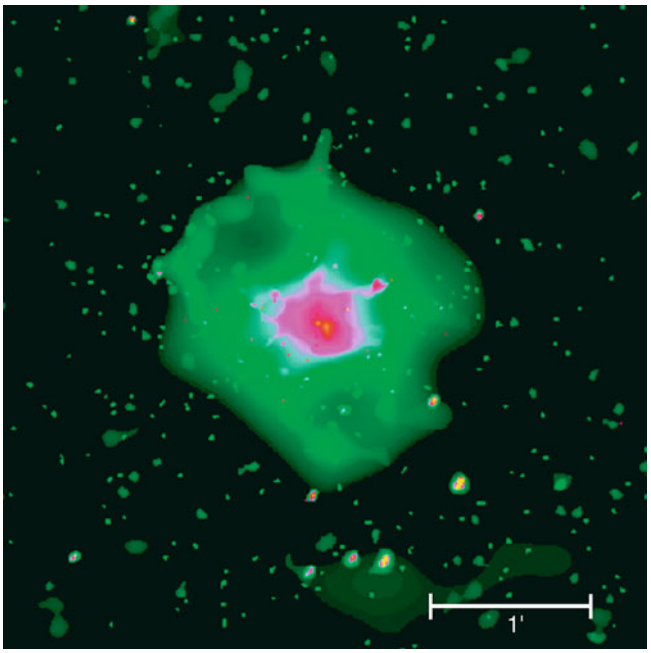

Fig. 6.31 Galaxy groups are also X-ray emitters, albeit weaker than clusters of galaxies. Moreover, the temperature of the ICM is lower than in clusters. This $4' \times 4'$ Chandra image shows HCG 62. Note the complexity of the X-ray emission and the two symmetrically aligned regions that seem to be virtually devoid of hot ICM—possibly holes blown free by jets from the central galaxy of this group (NGC 4761). Credit: NASA/CfA/J. Vrtilek et al.

Two more examples of the impact of a central AGN on the cluster gas are shown in Fig. 6.32. The energetics of this interaction can be enormous, as can be seen in the cluster MS 0735.6+7421 shown in the right panel of Fig. 6.32. The large size of the cavities in the X-ray emitting gas implies that a huge amount of energy was needed to push the gas away. From the cavity size and the gas density, one estimates that about $10^{12} M_\odot$ of gas has been displaced, requiring an energy of about 10^{62} erg. If this energy was generated by accretion onto the supermassive black hole located in the central galaxy of the cluster, with a mass-to-energy conversion of 10 %, the mass of the SMBH has grown by $\sim 6 \times 10^8 M_\odot$. Assuming that the gas was removed with about the sound speed of the ICM, this energy was released in the past $\sim 10^8$ yr, implying a mean luminosity of the central AGN of $\sim 3 \times 10^{46}$ erg/s of mechanical energy. Hence, by all accounts, this is a very energetic event which strongly impacts on the ICM of this cluster.

Feedback. The heating of the intracluster medium by a central radio source in clusters is the most visible example of *feedback*. We will encounter other examples lateron when we discuss the evolution of galaxies. As the gas cools and sinks towards the center, the central supermassive black hole can get fresh fuel and starts producing energy. The corresponding energy output in form of kinetic power in the radio jets or in radiation then heats the gas again, preventing efficient cooling and thus limits the mass accretion rate—and thus the fueling of the AGN. Hence, one might have a feedback loop, which does not need to have a stable equilibrium. The mass accretion rate may vary in time, as well as the AGN power output. Most likely, the feedback loop is somewhat more complicated than depicted here, but there is no doubt that AGN feedback is essential for understanding the gas in galaxy clusters.

Wide angle tail radio galaxies. Radio galaxies in clusters often have a different radio morphology than isolated ones. The radio jets necessarily interact with the intracluster gas and will be affected by it. Correspondingly, if the radio galaxy has a significant velocity relative to the ICM, the shape of the jets will get bend by ram pressure. A typical example for such *wide angle tail radio source* is shown in Fig. 6.33. Radio sources with such strong bended jets essentially only occur in clusters. Therefore, such sources can be used to search for clusters, and indeed these cluster searches have been successful—up to redshifts of order unity.

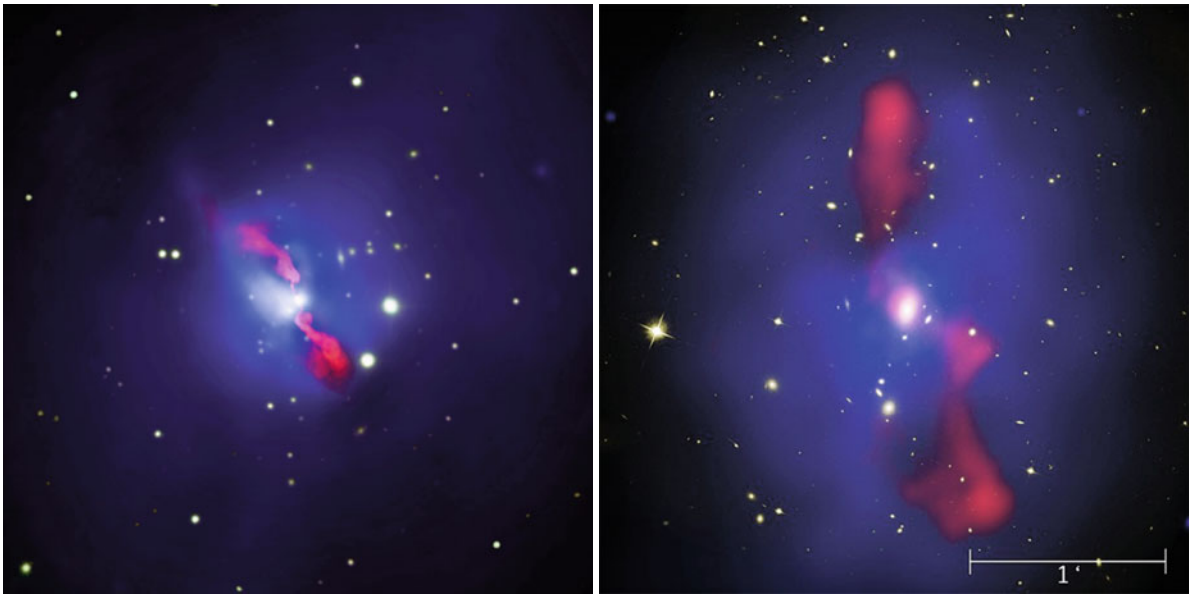

Fig. 6.32 The *left panel* shows the galaxy cluster Hydra A at redshift $z = 0.054$. This composite image is 4′.8 on the side and shows the X-ray emission (*blue*) and radio emission (*red*) superposed on the optical image. Clearly seen is the impact of the radio jets on the intracluster gas—at the location of the jets, the X-ray emission is strongly suppressed, whereas around the radio jets, overdensities are visible. Here, the gas, which has been pushed away from the jet, is accumulated. The *right panel* shows a composite image of the galaxy cluster MS 0735.6+7421 with redshift $z = 0.216$, showing the inner 700 kpc (corresponding to 200″) of the cluster. The Chandra X-ray image is shown in *blue*, and the radio emission as seen by the VLA shown in *red*, both superposed on an optical HST image of the cluster. The X-ray emission displays large cavities, located right at the position where the radio jets pass through the intracluster medium. This cluster contains presumably the most energetic interaction of the central AGN with the intracluster medium. Credit: *Left*: X-ray: NASA/CXC/U.Waterloo/C. Kirkpatrick et al.; Radio: NSF/NRAO/VLA; Optical: Canada-France-Hawaii-Telescope/DSS. *Right*: NASA, ESA, CXC, STScI, and B. McNamara (University of Waterloo), NRAO, and L. Birzan and team (Ohio University); journal article: B.R. McNamara et al. 2009, *An Energetic AGN Outburst Powered by a Rapidly Spinning Supermassive Black Hole or an Accreting Ultramassive Black Hole*, ApJ 698, 594, p. 595, Fig. 1 ©AAS. Reproduced with permission

The Bullet cluster. Clusters of galaxies are indeed excellent laboratories for hydrodynamical and plasma-physics processes on large scales. Shock fronts, for instance in merging clusters, cooling fronts (which are also called 'contact discontinuities' in hydrodynamics), and the propagation of sound waves can be observed in their intracluster medium. A particularly good example is the galaxy cluster 1E 0657−56 displayed in Fig. 6.34, also called the 'Bullet cluster'. To the right of the cluster center, strong and relatively compact X-ray emission (the 'bullet') is visible, while further to the right of it one sees an arc-shaped discontinuity in surface brightness. From the temperature distribution on both sides of the discontinuity one infers that it is a shock front—in fact, the shape of the gas distribution on the right resembles that of the air around a supersonic plane or bullet. The strength of the shock implies that the 'bullet' is moving at about $v \sim 3500\,\mathrm{km/s}$ through the intergalactic medium of the cluster. The interpretation of this observation is that we are witnessing the collision of two clusters, where one less massive cluster has passed, from left to right in Fig. 6.34, through a more massive one. The 'bullet' in this picture is understood to be gas from the central region of the less massive cluster, which is still rather

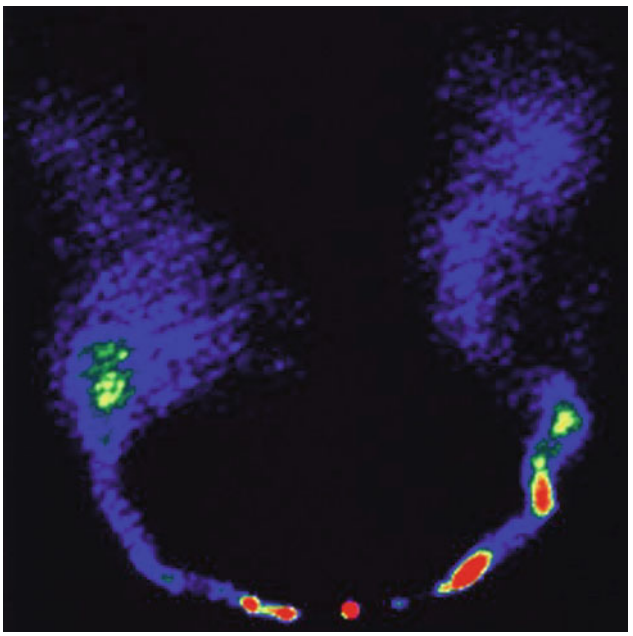

Fig. 6.33 NGC 1265, a radio galaxy in the Perseus cluster. Owing to its motion through the intracluster gas, with an estimated velocity of $\sim 2000\,\mathrm{km/s}$, its radio jets get bend by ram pressure. Credit: Image courtesy of NRAO/AUI and C. O'Dea & F. Owen

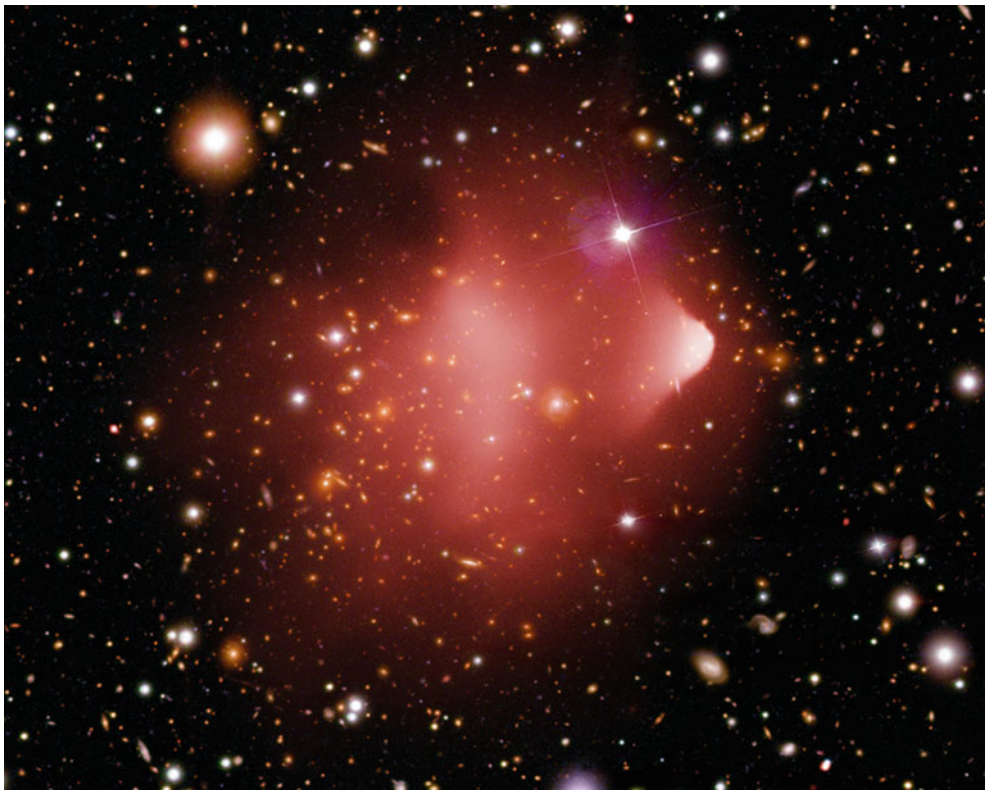

Fig. 6.34 The cluster of galaxies 1E 0657−56 is a perfect example of a merging cluster. The X-ray emission of this cluster as observed by Chandra, shown in *red*, is superposed on an optical HST image. The most remarkable feature in the X-ray map is the compact region to the right (westwards) of the cluster center (from which the cluster derives its name the 'Bullet cluster'), and the sharp transition in the surface brightness further at its right edge. An analysis of the brightness profile and of the X-ray temperature distribution shows that this must be a shock front moving at about 2.5 times the speed of sound, or $v \sim 3500\,\mathrm{km/s}$, through the gas. To the right of this shock front, a group of galaxies is visible. Credit: X-ray: NASA/CXC/CfA/M. Markevitch et al.; Optical: NASA/STScI; Magellan/U.Arizona/D. Clowe et al.

compact. This interpretation is impressively supported by the group of galaxies to the right of the shock front, which are probably the former member galaxies of the less massive cluster. As this cluster crosses through the more massive one, its galaxies and dark matter are moving collisionlessly, whereas the gas is decelerated by friction with the gas in the massive cluster: the galaxies and the dark matter are thus able to move faster through the cluster than the gas, which is lagging behind (and whose momentum transferred to the gas of the more massive cluster displaces the latter from its original location, centered on the corresponding galaxy distribution). We will see below that this interpretation is verified by a gravitational lens investigation of this double cluster.

6.4.4 The Sunyaev–Zeldovich effect

Electrons in the hot gas of the intracluster medium can scatter photons of the cosmic microwave background. The optical depth and thus the scattering probability for this Compton scattering is relatively low, but the effect is nevertheless observable and, in addition, is of great importance for the analysis of clusters, as we will now see.

Spectral signature. A photon moving through a cluster of galaxies towards us will change its direction through scattering and thus will not reach us. But since the cosmic background radiation is isotropic, for any CMB photon that is scattered out of the line-of-sight, another photon exists—statistically—that is scattered into it, so that the total number of photons reaching us is preserved. However, the energy of the photons changes slightly through scattering by the hot electrons, in a way that they have an (on average) higher frequency after scattering. Hence, by this inverse Compton scattering (Sect. 5.4.4), energy is on average transferred from the electrons to the photons, as can be seen in Fig. 6.35.

As a consequence, this scattering leads to a reduced number of photons at lower energies, relative to the Planck spectrum, which are shifted to higher energy. There is one photon energy where the intensity is unchanged, corresponding to a frequency of 218 GHz; below that frequency, the intensity is lower than that of the CMB, for higher frequencies, the intensity is increased. This effect is called the *Sunyaev–Zeldovich effect* (SZ-effect). It was predicted in 1970 and has now been observed in a large number of clusters. One example is presented in Fig. 6.36, where the frequency dependence of the effect is clearly seen.

> The CMB spectrum, measured in the direction of a galaxy cluster, deviates from a Planck spectrum; the degree of this deviation depends on the temperature of the cluster gas and on its density, and is independent of the cluster redshift.

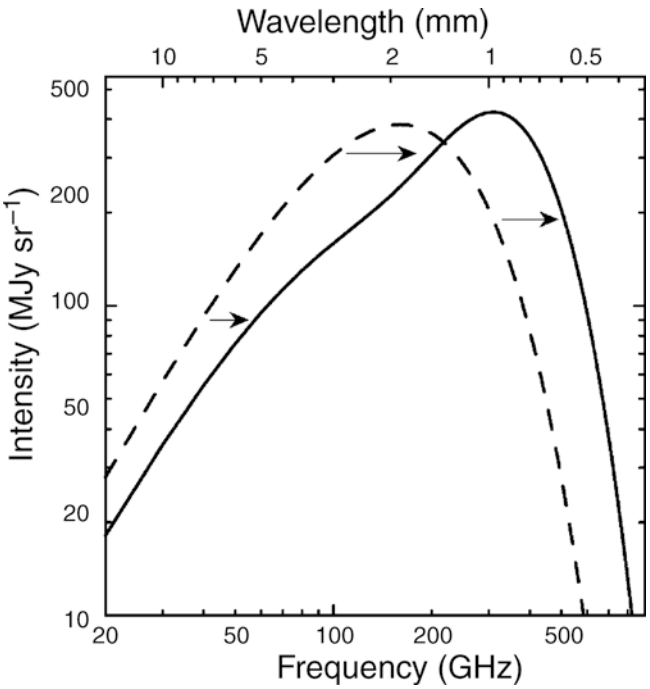

Fig. 6.35 The influence of the Sunyaev–Zeldovich effect on the cosmic background radiation. The *dashed curve* represents the Planck distribution of the unperturbed CMB spectrum, the *solid curve* shows the spectrum after the radiation has passed through a cloud of hot electrons. The magnitude of this effect, for clarity, has been very much exaggerated in this sketch. Source: J. Carlstrom et al. 2002, ARA&A 40, 643, Fig. 1, p. 646. Reprinted, with permission, from the *Annual Review of Astronomy & Astrophysics*, Volume 40 ©2002 by Annual Reviews www.annualreviews.org

In the Rayleigh–Jeans domain of the CMB spectrum, at wavelengths larger than about 2 mm, the intensity of the CMB is decreased by the SZ-effect. For the change in specific intensity in the RJ part, one obtains

$$\boxed{\frac{\Delta I_\nu^{\mathrm{RJ}}}{I_\nu^{\mathrm{RJ}}} = -2y} \,, \tag{6.46}$$

where

$$\boxed{y = \int \mathrm{d}l \, \frac{k_\mathrm{B} T_\mathrm{g}}{m_\mathrm{e} c^2} \, \sigma_\mathrm{T} \, n_\mathrm{e}} \quad \text{with} \quad \sigma_\mathrm{T} = \frac{8\pi}{3} \left(\frac{e^2}{m_\mathrm{e} c^2} \right)^2 \tag{6.47}$$

is the *Compton-y parameter* and σ_T the Thomson cross section for electron scattering. Obviously, y is proportional to the optical depth with respect to Compton scattering, given as an integral over $n_\mathrm{e}\,\sigma_\mathrm{T}$ along the line-of-sight. Furthermore, y is proportional to the gas temperature, because that defines the average energy transfer per scattering event [see (5.35)]. Overall, y is proportional to the integral over the gas pressure $P = n k_\mathrm{B} T_\mathrm{g}$ along the line-of-sight through the cluster.

The fact that the SZ-signal $\Delta I_\nu / I_\nu$ is independent of cluster redshift allows the investigation of clusters at high redshifts, provided the SZ-signal is spatially resolved. As we will see below, the SZ-effect can also be used to detect clusters in the first place, and this selection is much less biased to low redshifts than for flux-limited optical or X-ray surveys. As an example, the right-hand panel of Fig. 6.37 shows a very massive, high-redshift cluster that was selected by an SZ-survey.

Observations of the SZ-effect provide another possibility for analyzing the gas in clusters. For instance, if one can spatially resolve the SZ-effect, which is possible today with interferometric methods (see Fig. 6.38), one obtains information about the spatial density and temperature distribution. Here it is of crucial importance that the dependence on temperature and gas density is different from that in X-ray emission. Because of the quadratic dependence of the X-ray emissivity on n_e, the X-ray luminosity depends not only on the total gas mass, but also on its spatial distribution. Small-scale clumps in the gas, for instance, would strongly affect the X-ray emission. In contrast, the SZ-effect is linear in gas density and therefore considerably less sensitive to small-scale inhomogeneities in the ICM.

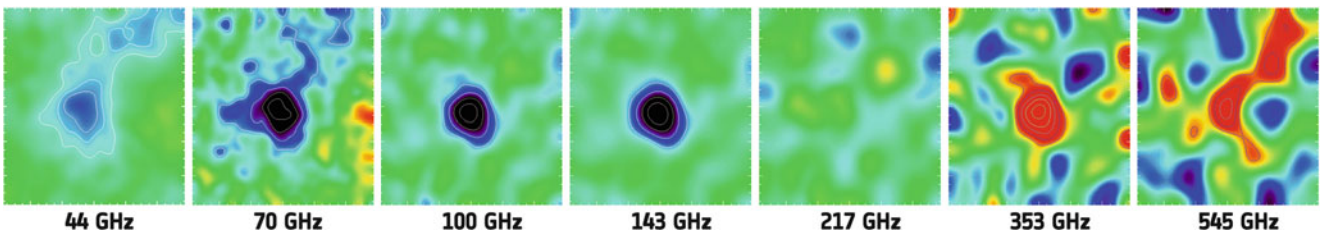

Fig. 6.36 Maps of the nearby cluster Abell 2319 in seven frequencies, obtained by the Planck satellite. These maps (with about 2° sidelength) clearly indicate the Sunyaev–Zeldovich effect caused by the hot gas in this cluster. At low frequencies, the SZ-effect causes a decrease of the surface brightness, whereas at high frequencies, the intensity is increased. The transition between these two regimes occurs at 218 GHz, as shown in Fig. 6.35; indeed, in the map of this frequency, no signal is seen. Credit and Copyright: ESA/LFI & HFI Consortia

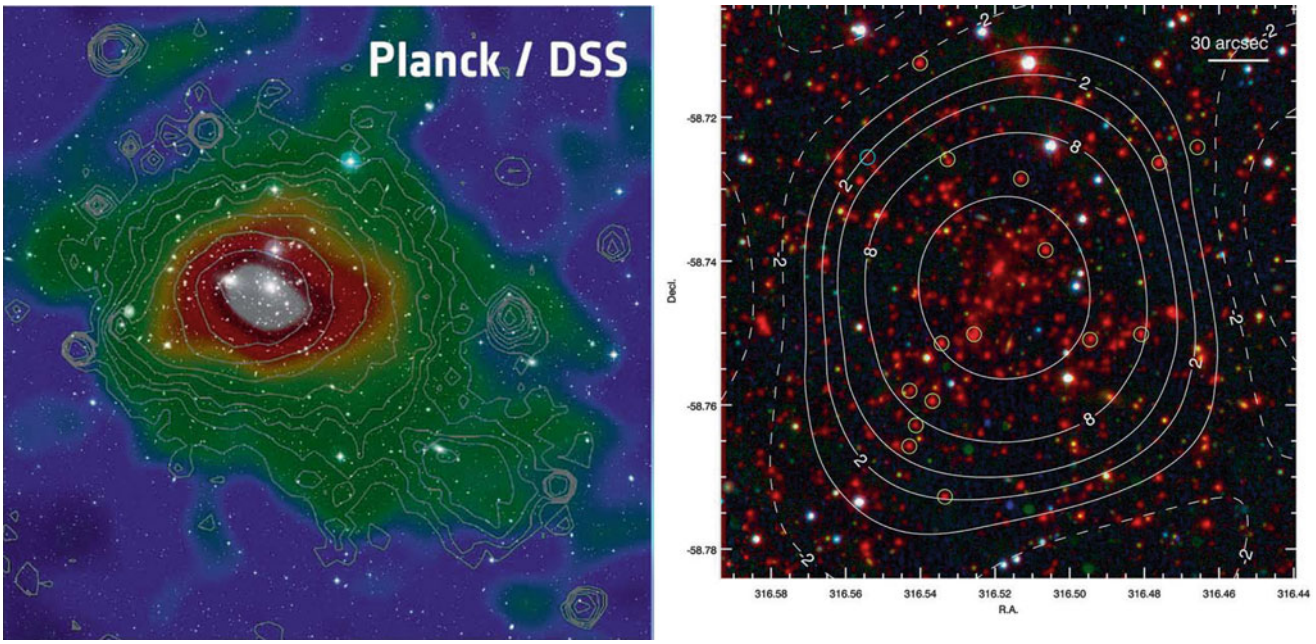

Fig. 6.37 *Left*: The Sunyaev–Zeldovich effect of the Coma cluster, as seen by the Planck satellite. The microwave temperature depletion is color coded, whereas the white contours display the X-ray emission of the cluster as measured by ROSAT. Both maps are superposed on the optical image from the Digitized Sky Survey 2. Note the very close correspondence between the SZ-signal and the X-ray emission. *Right*: The cluster SPT-CL J2106−5844 was detected by its SZ-signal, which is shown here as contour lines, superposed on a composite optical and mid-IR image, taken with the Magellan telescope and the Spitzer observatory, respectively. The cluster has a redshift of $z = 1.13$, and is (one of) the most massive clusters at redshift $z > 1$, with an estimated virial mass of $M_{200} \sim 1.3 \times 10^{15} M_\odot$. The cluster is also detected in X-rays, showing a very high temperature of $T \sim 11$ keV, and an X-ray luminosity of $L_X \sim 1.4 \times 10^{45}$ erg/s. The image is 4′8 on the side. Encircled galaxies have their cluster membership spectroscopically confirmed. Credit and Copyright: *Left*: Planck image: ESA/LFI & HFI Consortia; ROSAT image: Max-Planck-Institut für extraterrestrische Physik; DSS image: NASA, ESA, and the Digitized Sky Survey. Acknowledgment: Davide De Martin (ESA/Hubble). *Right*: R.J. Foley et al. 2011, *Discovery and Cosmological Implications of SPT-CL J2106−5844, the Most Massive Known Cluster at* $z > 1$, ApJ 731, 86, p. 3, Fig. 1. ©AAS. Reproduced with permission

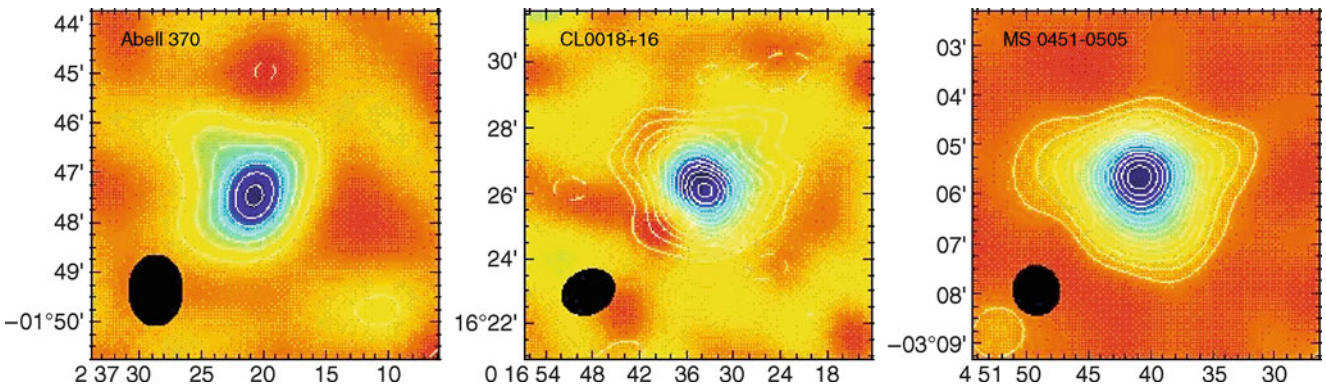

Fig. 6.38 Sunyaev–Zeldovich maps of three clusters of galaxies at $0.37 < z < 0.55$. Plotted is the temperature difference of the measured CMB relative to the average CMB temperature (or, at fixed frequency, the difference in radiation intensities). The black ellipse in each image specifies the instrument's beam size. For each of the clusters shown here, the spatial dependence of the SZ-effect is clearly visible. Since the SZ-effect is proportional to the electron density, the mass fraction of baryons in clusters can be measured if one additionally knows the total mass of the cluster from dynamical methods or from the X-ray temperature. The analysis of the clusters shown here yields for the mass fraction of the intergalactic gas $f_g \approx 0.08\, h^{-1}$. Source: L. Grego et al. 2001, *Galaxy Cluster Gas Mass Fractions from Sunyaev-Zeldovich Effect Measurements: Constraints on* Ω_m, ApJ 552, 2, p. 7, Fig. 1. ©AAS. Reproduced with permission

The integrated *y*-parameter. The amplitude of the spectral distortion caused by the SZ-effect is given by y, and SZ-maps essentially provide a map of y as a function of angular position in the cluster. When integrating y across the cluster, we get the total SZ-signal,

$$\int \mathrm{d}^2\theta\; y = \frac{1}{D_A^2} \int \mathrm{d}^2 R\; y \propto \frac{1}{D_A^2} \int \mathrm{d}V\; n_e\, T_g\;; \qquad (6.48)$$

hence, the integrated SZ-effect is proportional to the integrated SZ-parameter

$$Y = M_{\rm g}\, T_{\rm g}\ . \tag{6.49}$$

We see that Y is a measure of the product of gas mass and temperature. Both of these quantities can also be determined from X-ray observations, so that an independent estimate of Y can be obtained. In order to distinguish between the two, one usually denotes the result from SZ-observations by $Y_{\rm SZ}$, in contrast to $Y_{\rm X}$ when it is determined from X-ray studies. These two can be different in general, due to the quadratic dependence of the X-ray emission on local gas density or through the temperature variation inside clusters.

Kinetic SZ-effect. Beside the thermal SZ-effect just described, there is a related effect, called the kinetic SZ-effect. This is due to the fact that clusters may have a peculiar velocity. Suppose the peculiar velocity of a cluster is directed towards us, then the photons scattering in its intracluster gas and reaching us will be scattered by electrons which have an average velocity towards us. These scattered photons thus experience on average a blueshift, which is visible in the CMB spectrum in the direction of this cluster. The kinetic SZ-effect has a different spectral signature than the thermal SZ-effect and can thus in principle be distinguished from it. A robust measurement of the kinetic SZ-effect would allow a direct measurement of the line-of-sight component of the peculiar velocities of clusters. However, the expected amplitude of the kinetic SZ-effect is smaller than that of the thermal SZ-effect by a factor of ~ 10 and thus much harder to detect. First detections have recently been reported in the literature.

Distance determination. For a long time, the SZ-effect was mainly considered a tool for measuring distances to clusters of galaxies, and from this to determine the Hubble constant. We will now schematically show how the SZ-effect, in combination with the X-ray emission, allows us to determine the distance to a cluster. The change in the CMB intensity has the dependence

$$\frac{\left|\Delta I_\nu^{\rm RJ}\right|}{I_\nu^{\rm RJ}} \propto n_{\rm e}\, L\, T_{\rm g}\ ,$$

where L is the extent of the cluster along the line-of-sight. To obtain this relation, we replace the l-integration in (6.47) by a multiplication with L, which yields the correct functional dependence. On the other hand, the surface brightness of the X-ray radiation behaves as

$$I_{\rm X} \propto L n_{\rm e}^2\ .$$

Combining these two relations, we are now able to eliminate $n_{\rm e}$. Since $T_{\rm g}$ is measurable from the X-ray spectrum, the dependence

$$\frac{\left|\Delta I_\nu^{\rm RJ}\right|}{I_\nu^{\rm RJ}} \propto \sqrt{L\, I_{\rm X}}$$

remains. Now assuming that the cluster is spherical, its extent L along the line-of-sight equals its transverse extent $R = \theta D_{\rm A}$, where θ denotes its angular extent and $D_{\rm A}$ the angular-diameter distance (4.49) to the cluster. With this assumption, we obtain

$$D_{\rm A} = \frac{R}{\theta} \sim \frac{L}{\theta} \propto \left(\frac{\Delta I_\nu^{\rm RJ}}{I_\nu^{\rm RJ}}\right)^2 \frac{1}{I_{\rm X}}\ . \tag{6.50}$$

Hence, the angular-diameter distance can be determined from the measured SZ-effect, the X-ray temperature of the ICM, and the surface brightness in the X-ray domain. Of course, this method is more complicated in practice than sketched here, but it is applied to the distance determination of clusters. In particular, the assumption of the same extent of the cluster along the line-of-sight as its transverse size is not well justified for any individual cluster due to triaxiality, but one expects this assumption to be valid on average for a sample of clusters. Hence, the SZ-effect is another method of distance determination, independent of the redshift of the cluster, and therefore suitable for determining the Hubble constant.

Discussion. The natural question arises whether this method, in view of the assumptions it is based on, can compete with the determination of the Hubble constant via the distance ladder and Cepheids, as described in Sect. 3.9, or from the CMB, to be discussed in Sect. 8.7. The same question also needs to be asked for the determination of H_0 by means of the time delay in gravitational lens systems, which we discussed in Sect. 3.11.4. In both cases, the answer is the same: presumably neither of the two methods will provide a determination of the Hubble constant with an accuracy comparable to that achieved by the local methods and from the angular fluctuations in the CMB. Nevertheless, both methods are of great value for cosmology: first, the distance ladder has quite a number of rungs. If only one of these contains an as yet undetected severe systematic error, it could affect the resulting value for H_0. Second, the Hubble Key Project measured the expansion rate in the local Universe, typically within ~ 100 Mpc (the distance to the Coma cluster). As we will see later, the Universe contains inhomogeneities on these length scales. Thus, it may well be that we live in a slightly overdense or underdense region of the Universe, where the Hubble constant deviates from the global value. In contrast to this, both the SZ-effect and the lensing method measure the Hubble constant on truly cosmic scales, and both methods do so in only a single step—there is no distance ladder involved. For these reasons, these two methods are of considerable interest in additionally confirming our H_0 measurements. Another aspect adds to this, which must not be underestimated: even if the same or a similar value results from these measurements as the one from the Hubble Key Project, we still have learned an important fact, namely that the local Hubble constant agrees with the one measured on cosmological scales—as predicted by our cosmological model, which can thus be tested. Indeed, both methods have been applied to quite a number of lens systems and luminous clusters showing an SZ effect, respectively, and they yield values for H_0 which are compatible within the error bars with the value of H_0 obtained from the Hubble Key Project.

6.4.5 X-ray and SZ catalogs of clusters

As we have seen, projection effects may play a crucial role in the selection of galaxy clusters through searching for an overdensity of galaxies on the sphere using optical methods. A more reliable way of selecting clusters is by their X-ray emission, since the hot X-ray gas signifies a deep potential well, thus a real three-dimensional overdensity of matter, so that projection effects become virtually negligible. The X-ray emission is $\propto n_{\rm e}^2$, which again renders projection effects improbable. In addition, the X-ray emission, its temperature

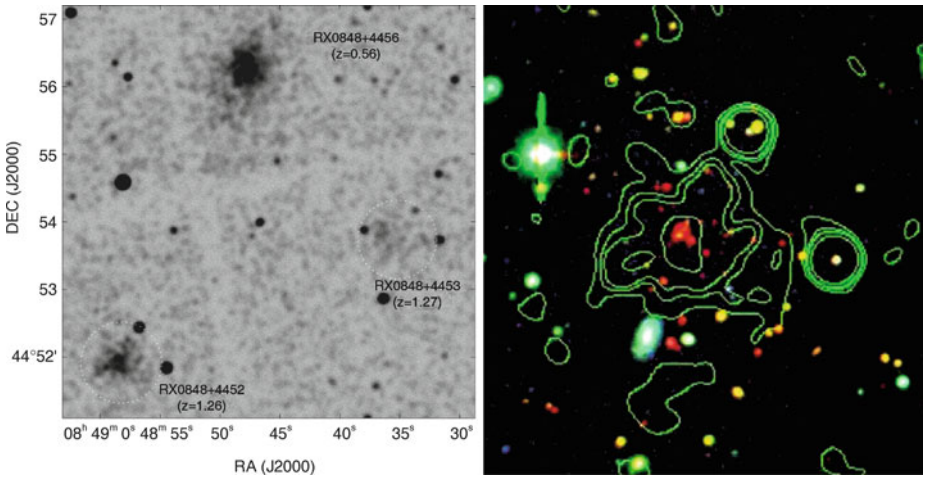

Fig. 6.39 *On the left*: Chandra image of a $6' \times 6'$-field with two clusters of galaxies at high redshift. *On the right*: a $2' \times 2'$-field centered on one of the clusters presented on the left (RX J0849+4452), in B, I, and K, overlaid with the X-ray brightness contours. Source: S.A. Stanford et al. 2001, *The Intracluster Medium in $z > 1$ Galaxy Clusters*, ApJ 552, 504, p. 505, 507, Figs. 1, 3. ©AAS. Reproduced with permission

in particular, seems to be a very good measure for the cluster mass, as we will discuss further below. Whereas the selection of clusters is not based on their temperature, but on the X-ray luminosity, we shall see that L_X is also a good indicator for the mass of a cluster (see Sect. 6.5).

The first cosmologically interesting X-ray catalog of galaxy clusters was the EMSS (Extended Medium Sensitivity Survey) catalog. It was constructed from archival images taken by the *Einstein observatory* which were scrutinized for X-ray sources other than the primary target in the field-of-view of the respective observation. These were compiled and then further investigated using optical methods, i.e., photometry and spectroscopy. The EMSS catalog contains 835 sources, most of them AGNs, but it also contains 104 clusters of galaxies. Among these are six clusters at redshift ≥ 0.5; the most distant is MS 1054−03 at $z = 0.83$ (see Fig. 6.21). Since the Einstein images all have different exposure times, the EMSS is not a strictly flux-limited catalog. But with the flux limit known for each exposure, the luminosity function of clusters can be derived from this.

The same method as was used to compile the EMSS was applied to ROSAT archival images by various groups, leading to several catalogs of X-ray-selected clusters. The selection criteria of the different catalogs vary. Since ROSAT was more sensitive than the Einstein observatory, these catalogs contain a larger number of clusters, and also ones at higher redshift (Fig. 6.39). Furthermore, ROSAT performed a survey of the full sky, the ROSAT All-Sky Survey (RASS). The RASS contains about 10^5 sources distributed over the whole sky. The identification of extended sources in the RASS (in contrast to non-extended sources—about five times more AGNs than clusters are expected) yielded a catalog of clusters which, owing to the relatively short exposure times in the RASS, contains the brightest clusters. The exposure time in the RASS is not uniform over the sky since the applied observing strategy led to particularly long exposures for the regions around the Northern and Southern ecliptic pole (see Fig. 6.40).

From the luminosity function of X-ray clusters, a mass function can be constructed, using the relation between L_X and the cluster mass that will be discussed in the following section. Furthermore, as we will explain in more detail in Sect. 8.2, this cluster mass function is an important probe for cosmological parameters.

More recently, the sensitivity and throughput of SZ telescopes and instruments became sufficiently large to not only study the SZ-effect of known clusters, but to survey the sky for SZ sources. In 2009 the first SZ-selected clusters were found, and at the time of writing, at least three telescopes are used for constructing cluster catalogs through SZ-selection. The South Pole Telescope (SPT), the Atacama Cosmology Telescope, and the Planck satellite, together have found more than 1000 clusters. The selection criteria for SZ clusters is quite different from those of X-ray (or optical) cluster samples, since we have seen that the strength of the SZ-signal is redshift-independent, as long as the cluster is spatially resolved. If, however, the angular resolution of the observations is not high enough to resolve the SZ-signal from a cluster, distant clusters are more difficult to find, since the signal gets diluted. On the other hand, the SZ-signal is weak, so that only the more massive clusters can be readily discovered. The different selection effects are clearly visible in the redshift and mass distribution of the resulting cluster catalogs, shown in Fig. 6.41. The fact that Planck finds the more massive clusters at redshifts $z \lesssim 0.5$ originates from its all-sky survey, in which the rare objects are found, whereas the SPT clusters in Fig. 6.41 were selected from a region of 720 deg^2.

6.4.6 Radio relics

In some galaxy clusters, one finds extended, diffuse radio sources at large cluster-centric radii, the so-called radio relics. These radio sources do not coincide with member galaxies in the cluster, and thus have an intracluster origin. Their shapes are often very elongated or irregular, as can

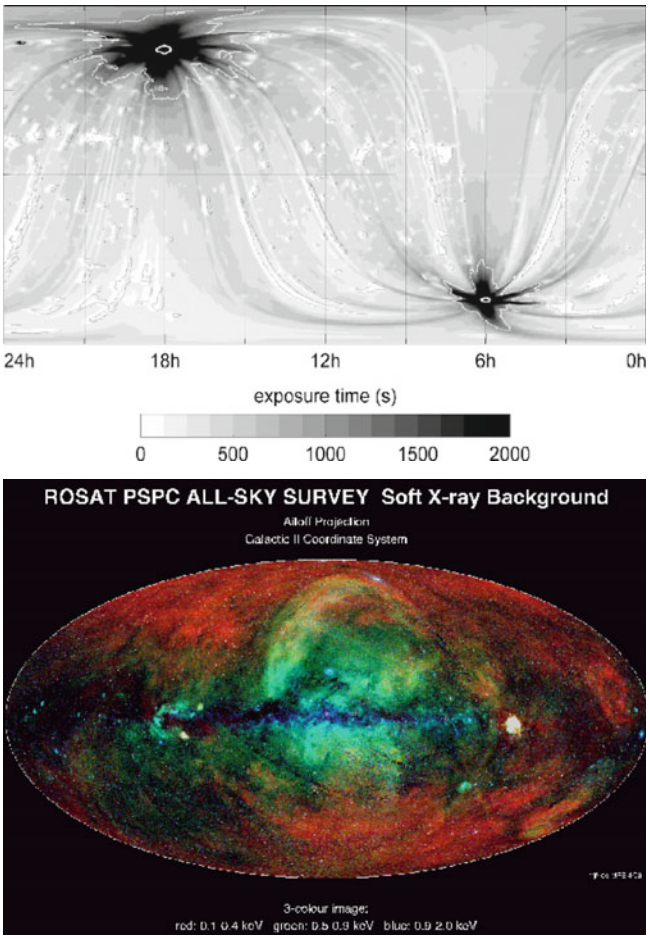

Fig. 6.40 The *top panel* shows the total exposure time in the ROSAT All-Sky Survey as a function of sky position. Near the ecliptic poles the exposure time is longest, as a consequence of the applied observing strategy. Because of the "South Atlantic Anomaly" (a region of enhanced cosmic ray flux over the South Atlantic Ocean, off the coast of Brazil, caused by the shape of the Earth's magnetosphere), the exposure time is generally higher in the North than in the South. The X-ray sky, as observed in the RASS, is shown in the *lower panel*. The colors indicate the shape of the spectral energy distribution, where *blue* indicates sources with a harder spectrum. Credit: Max-Planck-Institut für Extraterrestrische Forschung, Garching; journal article: S.L. Snowden et al. 1997, *ROSAT Survey Diffuse X-Ray Background Maps. II.*, ApJ 485, 125

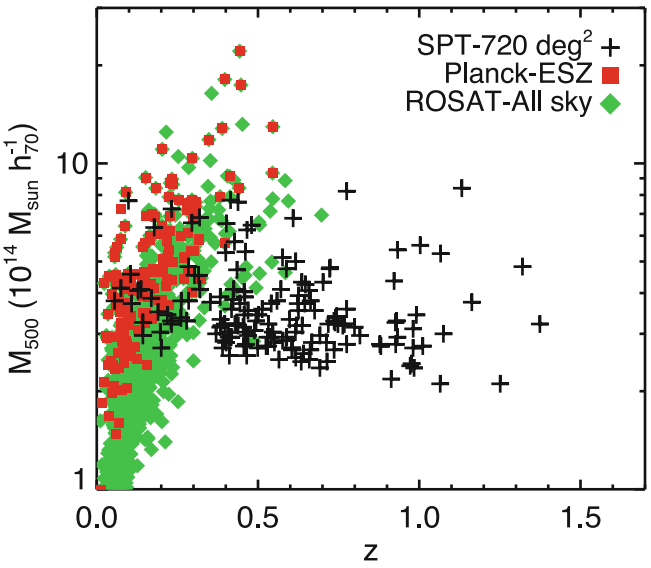

Fig. 6.41 Distribution of clusters in redshift and mass, as obtained from three different surveys. *Green* points show clusters selected through their X-ray emission, here from the ROSAT All-Sky Survey (see Fig. 6.40). The *crosses* show clusters selected by their SZ-signal, as obtained from the South Pole Telescope; its high angular resolution resolves the SZ-signal even for very distant clusters. Correspondingly, the mass distribution of the selected cluster does not show any marked redshift dependence, at least out to $z \sim 1$. *Red* points show clusters selected by Planck, also through their SZ-signal. Due to the lower angular resolution of Planck, the signal from higher-redshift clusters, which are smaller than the telescope beam, is diluted. Source: C.L. Reichardt et al. 2013, *Galaxy Clusters Discovered via the Sunyaev-Zel'dovich Effect in the First 720 Square Degrees of the South Pole Telescope Survey*, ApJ 763, 127, Fig. 4. ©AAS. Reproduced with permission

be seen by the example shown in Fig. 6.42. The strong polarization of the radio emission shows that the origin of the radiation is synchrotron emission. Therefore, these radio relics must contain relativistic electrons. About 50 radio relics have been found to date.

As we discussed in Sect. 5.1.3, relativistic particles are accelerated in shock fronts, such as occur in supernova remnants. Shock fronts are formed in plasmas with supersonic flow velocities. A natural way of explaining the occurrence of a shock in the outskirts of a cluster is to assume that the cluster has been subject to a recent merger event. If the intracluster gas of the two clusters run into each other, a shock front is formed. For the radio relic shown in Fig. 6.42, the predictions of the shock hypothesis were tested in quite some detail. The radio spectral index α varies strongly across the relic, from $\alpha \approx 0.6$ to about 2.0, indicating that the electron distribution closest to the shock has the flattest spectrum, whereas it continuously steepens away from the shock, due to energy losses. The high degree of polarization ($\sim 50\,\%$) shows the presence of a very well-ordered magnetic field in the emission region.

The merging hypothesis for the example shown in Fig. 6.42 is further supported by the strongly disturbed morphology of the intracluster gas, as shown by the X-ray contours, as well as by the indication of a second relic on the opposite side of the cluster center; such counter relics are predicted from numerical simulations of cluster mergers.

6.5 Scaling relations for clusters of galaxies

Our examination of galaxies revealed the existence of various scaling relations, for example the Tully–Fisher relation.

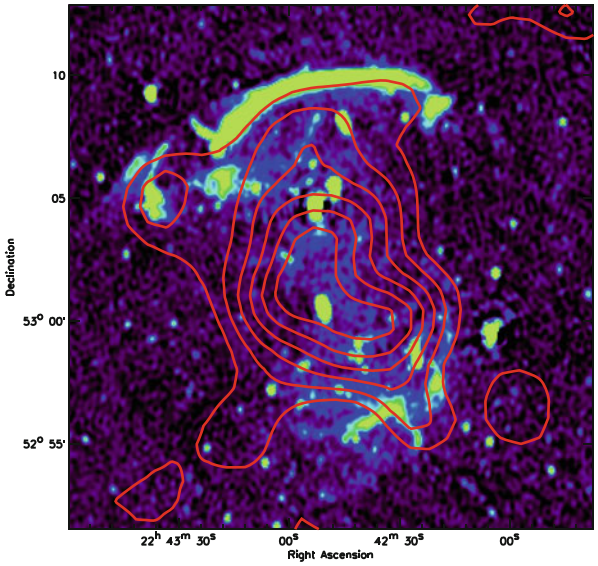

Fig. 6.42 1.4 GHz map of the galaxy cluster CIZA J2242.8+5301 at redshift $z = 0.1921$, taken with the Westerbork Synthesis Radio Telescope (WSRT), on which the X-ray contours (shown in *red*) are superposed. The most prominent radio source is the large elongated feature some 1.5 Mpc to the North of the cluster center, whose length is ~ 2 Mpc. Source: R.J. van Weeren et al. 2010, arXiv:1010.4306, Fig. 1. Reproduced by permission of the author

These have proven to be very useful not only for the distance determination of galaxies, but also because any successful model of galaxy evolution needs to be able to explain these empirical scaling relations—they must contain information about the formation of galaxies. Therefore, it is of great interest to examine whether clusters of galaxies also fulfill any such scaling relation. As we will see, the X-ray properties of clusters play a central role in this.

6.5.1 Mass-temperature relation

It is expected that the larger the spatial extent, velocity dispersion of galaxies, temperature of the X-ray gas, and luminosity of a cluster are, the more massive it is. In fact, from theoretical considerations one can deduce the existence of relations between these parameters. The X-ray temperature T specifies the thermal energy per gas particle, which should be proportional to the binding energy for a cluster in virial equilibrium,

$$T \propto \frac{M}{r} \,.$$

Since this relation is based on the virial theorem, r should be chosen to be the radius within which the matter of the cluster is virialized. This value for r is called the *virial radius* $r_{\rm vir}$. From theoretical considerations of cluster formation (see Chap. 7), one finds that the virial radius is defined such that within a sphere of radius $r_{\rm vir}$, the average mass density of the cluster is about $\Delta_{\rm c} \approx 200$ times as high as the critical density $\rho_{\rm cr}$ of the Universe (see also Problem 6.1). The mass within $r_{\rm vir}$ is called the *virial mass* $M_{\rm vir}$ which is, according to this definition,

$$\boxed{M_{\rm vir} = \frac{4\pi}{3}\,\Delta_{\rm c}\,\rho_{\rm cr}\,r_{\rm vir}^3} \,. \tag{6.51}$$

Combining the two above relations, one obtains

$$\boxed{T \propto \frac{M_{\rm vir}}{r_{\rm vir}} \propto r_{\rm vir}^2 \propto M_{\rm vir}^{2/3}} \,. \tag{6.52}$$

This relation can now be observationally tested by using a sample of galaxy clusters with known temperature and with mass determined by the methods discussed in Sect. 6.4.2. An example of this is displayed in Fig. 6.43, in which the mass is plotted versus temperature for clusters from the extended HIFLUGCS sample.[8] Since it is easier to determine the mass inside a smaller radius than the virial mass itself, the mass M_{500} within the radius r_{500}, the radius within which the average density is 500 times the critical density, is plotted here. The measured values clearly show a very strong correlation, and best-fit straight lines describing power laws of the form $M = AT^{\alpha}$ are also shown in the figure. The exact values of the two fit parameters depend on the choice of the cluster sample; the right-hand panel of Fig. 6.43 shows in particular that galaxy groups (thus, 'clusters' of low mass and temperature) are located below the power-law fit that is obtained from higher mass clusters. If one confines the sample to clusters with $M \geq 5 \times 10^{13} M_{\odot}$, the best fit is described by

$$M_{500} = 3.57 \times 10^{13} M_{\odot} \left(\frac{k_{\rm B} T}{1\,{\rm keV}}\right)^{1.58} \,, \tag{6.53}$$

with an uncertainty in the parameters of slightly more than 10 %. This relation is very similar to the one deduced from our theoretical consideration, $M \propto T^{1.5}$. With only small variations in the parameters, the relation (6.53) is obtained both from a cluster sample in which the mass was determined

[8] One of the cluster catalogs that were extracted from the RASS data is the HIFLUGCS catalog. It consists of the 63 X-ray-brightest clusters and is a strictly flux-limited survey, with $f_{\rm X}(0.1\text{-}2.4\,{\rm keV}) \geq 2.0 \times 10^{-11}\,{\rm erg\,s^{-1}\,cm^{-2}}$; it excludes the Galactic plane, $|b| \leq 20°$, as well as other regions around the Magellanic clouds and the Virgo cluster of galaxies in order to avoid large column densities of Galactic gas which lead to absorption, as well as Galactic and other nearby X-ray sources. The extended HIFLUGCS survey contains, in addition, several other clusters for which good measurements of the brightness profile and the X-ray temperature are available.

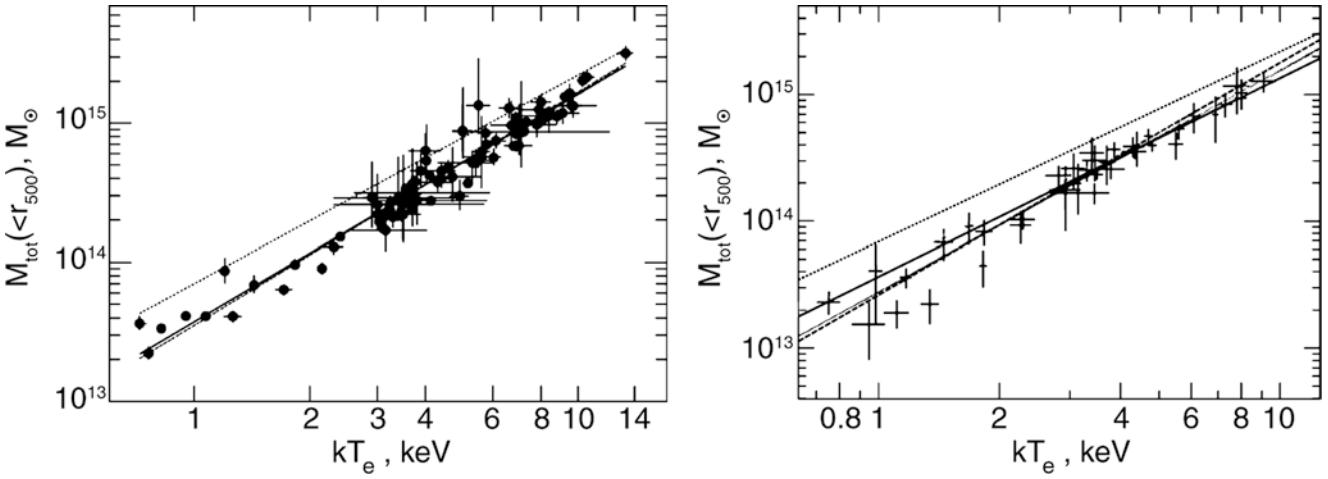

Fig. 6.43 For the clusters of galaxies from the extended HIFLUGCS sample, the mass within a mean overdensity of 500 is plotted as a function of X-ray temperature, where a dimensionless Hubble constant of $h = 0.5$ was assumed. In the *left-hand panel*, the mass was determined by applying an isothermal β-model, while in the *right-hand panel*, the radial temperature profile $T(r)$ was used to determine the mass, by means of (6.37). Most of the temperature measurements are from observations by the ASCA satellite. The *solid* and *dash-dotted curves* in the *left-hand panel* show the best fit to the data, where for the latter only the clusters from the original HIFLUGCS sample were used. In the *right-hand panel*, the *dashed line* is a fit to all the data in the plot, while the *solid line* takes into account only clusters with a mass $\geq 5 \times 10^{13} M_\odot$. In both panels, the *upper dotted line* shows the mass-temperature relation that was obtained from a simulation using simplified gas dynamics—the slope agrees with that found from the observations, but the amplitude is significantly too high. Source: A. Finoguenov et al. 2001, *Details of the mass-temperature relation for clusters of galaxies*, A&A 368, 749, p. 752, Figs. 1, 2. ©ESO. Reproduced with permission

based on an isothermal β-model, and from a cluster sample in which the measured radial temperature profile $T(r)$ was utilized in the mass determination [see (6.37)]. Constraining the sample to clusters with temperatures above 3 keV, one obtains a slope of 1.48 ± 0.1, in excellent agreement with theoretical expectations. Considerably steeper mass-temperature relations result from the inclusion of galaxy groups into the sample, from which we conclude that they do not follow in detail the scaling argument sketched above.

The X-ray temperature of galaxy clusters apparently provides a very accurate measure for their virial mass, better than the velocity dispersion (see below).

6.5.2 Mass-velocity dispersion relation

The velocity dispersion of the galaxies in a cluster also can be related to the mass: from (6.26) we find

$$M_{\rm vir} = \frac{3 r_{\rm vir} \sigma_v^2}{G} \,. \tag{6.54}$$

Together with $T \propto \sigma_v^2$ and $T \propto r_{\rm vir}^2$, it then follows that

$$\boxed{M_{\rm vir} \propto \sigma_v^3} \,. \tag{6.55}$$

This relation can now be tested using clusters for which the mass was determined using the X-ray method, and for which measurements of the velocity dispersion of the cluster galaxies are available. Alternatively, the relation $T \propto \sigma_v^2$ can be tested. One finds that these relations are essentially satisfied for the observed clusters. However, the relation between σ_v and M is not as tight as the M-T relation. Furthermore, numerous clusters exist which strongly deviate from this relation. These are clusters of galaxies that are not relaxed, as can be deduced from the velocity distribution of the cluster galaxies (which strongly deviates from a Maxwell distribution in these cases) or from a bimodal or even more complex galaxy distribution in the cluster. These outliers need to be identified, and removed, if one intends to apply the scaling relation between mass and velocity dispersion.

6.5.3 Mass-luminosity relation

The total X-ray luminosity that is emitted via bremsstrahlung is proportional to the squared gas density and the gas volume, hence it should behave as

$$L_{\rm X} \propto \rho_{\rm g}^2 \, T^{1/2} \, r_{\rm vir}^3 \propto \rho_{\rm g}^2 \, T^{1/2} \, M_{\rm vir} \,. \tag{6.56}$$

Estimating the gas density through $\rho_{\rm g} \sim M_{\rm g} \, r_{\rm vir}^{-3} = f_{\rm g} \, M_{\rm vir} \, r_{\rm vir}^{-3}$, where $f_{\rm g} = M_{\rm g}/M_{\rm vir}$ denotes the gas fraction

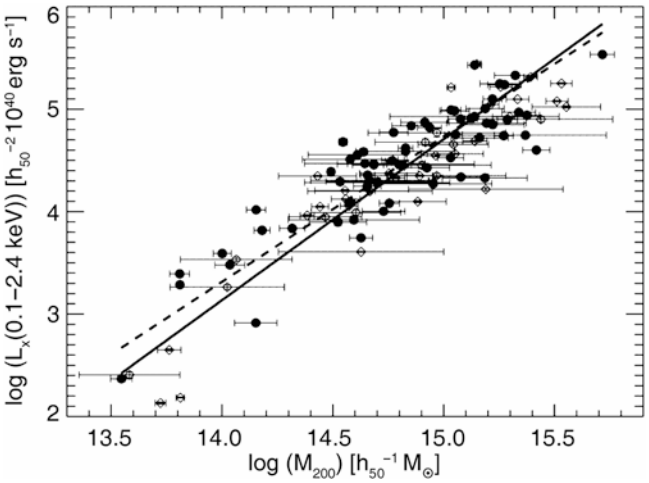

Fig. 6.44 For the galaxy clusters in the extended HIFLUGCS sample, the X-ray luminosity in the energy range of the ROSAT satellite is plotted versus the mass of the cluster. The solid points show the clusters of the HIFLUGCS sample proper. For the full sample and for the main HIFLUGCS sample, a best-fit power law is indicated by the *solid line* and *dashed line*, respectively. Source: T. Reiprich & H. Böhringer 2002, *The Mass Function of an X-Ray Flux-limited Sample of Galaxy Clusters*, ApJ 567, 716, p. 726, Fig. 6. ©AAS. Reproduced with permission

with respect to the total mass of the cluster, and using (6.52), we obtain

$$L_{\rm X} \propto f_{\rm g}^2 \, M_{\rm vir}^{4/3} \; . \tag{6.57}$$

This relation needs to be modified if the X-ray luminosity is measured within a fixed energy interval. Particularly for observations with ROSAT, which could only measure low-energy photons (below 2.4 keV), the received photons from massive clusters typically had $E_\gamma < k_{\rm B} T$, so that the measured X-ray luminosity becomes independent of T. Hence, one expects a modified scaling relation between the X-ray luminosity measured by ROSAT $L_{<2.4\,\rm keV}$ and the mass of the cluster,

$$L_{<2.4\,\rm keV} \propto f_{\rm g}^2 \, M_{\rm vir} \; . \tag{6.58}$$

This scaling relation can also be tested empirically, as shown in Fig. 6.44, where the X-ray luminosity in the energy range of the ROSAT satellite is plotted against the virial mass. One can immediately see that clusters of galaxies indeed show a strong correlation between luminosity and mass, but with a clearly larger scatter than in the mass-temperature relation.[9] Therefore, the temperature of the intergalactic gas is a better mass indicator than the X-ray luminosity or the velocity dispersion of the cluster galaxies.

[9]It should be noted, though, that the determination of $L_{\rm X}$ and M are independent of each other, whereas in the mass determination the temperature is an explicit parameter so that the measurements of these two parameters are correlated.

However, determining the slope of the relation from the data approximately yields $L_{<2.4\,\rm keV} \propto M^{1.5}$, instead of the expected behavior ($L_{<2.4\,\rm keV} \propto M^{1.0}$). Obviously, the above scaling arguments are not valid with the assumption of a constant gas fraction. This discrepancy between theoretical expectations and observations has been found in several samples of galaxy clusters and is considered well established. An explanation is found in models where the intergalactic gas has been heated not only by gravitational infall into the potential well of the cluster. Other sources of heating may have been present or still are. For cooler, less massive clusters, this additional heating should have a larger effect than for the very massive ones, which could also explain the deviation of low-M clusters from the mass-luminosity relation of massive clusters visible in Fig. 6.44. As already argued in the discussion of cooling flows in Sect. 6.4.3, an AGN in the inner regions of the cluster may provide such a heating. The kinetic energy provided by supernovae in cluster galaxies is also considered a potential source of additional heating of the intergalactic gas. Furthermore, the normalization of the luminosity-mass relation appears to be significantly different for cool-core clusters than for others, which supports the idea that heating affects this relation. It is obvious that solving this mystery will provide us with better insights into the formation and evolution of the gas component in clusters of galaxies.

Despite this discrepancy between the simple models and the observations, Fig. 6.44 shows a clear correlation between mass and luminosity, which can thus be used empirically after having been calibrated. Although the temperature is the preferred measure for a cluster's mass, one will in many cases resort to the relation between mass and X-ray luminosity because determining the luminosity (in a fixed energy range) is considerably simpler than measuring the temperature, for which significantly better photon statistics, i.e., longer exposure times are required.

6.5.4 The Y-parameter

The foregoing scaling relations connect the cluster mass with an observable. We have seen that the relation between cluster mass and gas temperature yields the smallest dispersion; hence, the X-ray temperature provides the best mass proxy of those that we considered above.

More recently, an alternative quantity for estimating the cluster mass was introduced. We saw in Sect. 6.4.4 above that the integrated SZ-effect is proportional to $Y = M_{\rm g} T_{\rm g}$, where is case of non-isothermal temperature distribution $T_{\rm g}$ needs to be interpreted as density-weighted temperature. In analogy, one considers

$$Y_{\rm X} := T_{\rm X} \, M_{\rm g} \; , \tag{6.59}$$

which is related to the thermal energy of gas in the cluster. The gas mass is related to the total mass by $M_g = f_g M$, where f_g is the gas-mass fraction. Assuming this to be constant, and using (6.52), we expect a scaling relation of the form

$$Y_X \propto M^{5/3} \,. \tag{6.60}$$

Numerical simulations including hydrodynamics first suggested that clusters should have a smaller scatter around the Y_X-M relation than for the other scaling relations. From X-ray observations, one indeed finds that clusters obey a relation very close to (6.60), with a slightly different slope, $M \propto Y^{0.55}$ (instead of 0.6). Furthermore, the scatter around the Y_X-M relation is smaller than that around the T_X-M relation, and in particular, at least for relaxed clusters, it is well described by a power-law behavior. Hence, Y_X provides a very useful mass proxy.

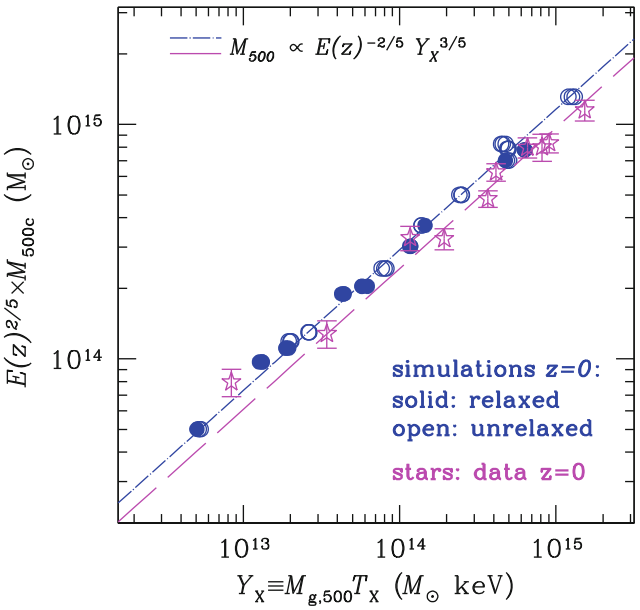

Fig. 6.45 The relation between the cluster mass M_{500} and the Y_X parameter. For this figure, the central region of the clusters has been cut out; specifically, the X-ray temperature was measured in the annulus $0.15 r_{500} \le r \le r_{500}$. The *blue* points show results from simulated clusters, where *filled dots* correspond to relaxed (cool-core) clusters, *open symbols* to non-relaxed clusters. It can be seen that both types of simulated clusters follow the same power law between M and Y_X. A sample of observed relaxed cluster is shown as *star symbols*; since these clusters are not at redshift zero, as the simulated ones, a redshift correction was applied to their masses (see Sect. 6.5.5 below). The observed clusters follow a very similar power law, though with a $\sim$ 15 % smaller normalization. Source: A.V. Kravtsov et al. 2006, *A New Robust Low-Scatter X-Ray Mass Indicator for Clusters of Galaxies*, ApJ 650, 128, p. 135, Fig. 7. ©AAS. Reproduced with permission

Center-excised scaling relations. We have seen that one can roughly divide clusters into cool-core clusters, which show a strong peak in the X-ray emission towards the center, and non-cool core clusters, which are presumably dynamically disturbed. At first sight, one would not expect that both types of clusters follow the same scaling relations. Indeed, not only the temperature profile of non-cool core clusters is different from that of cool-core clusters, but as a consequence also their pressure profiles, which is the relevant quantity for the SZ effect [see (6.47)]. Furthermore, we have seen that feedback processes from a central AGN affect the intracluster medium, causing (strong) deviations from spherical symmetry and locally varying temperature. Hence, we would expect that the central regions of clusters do not follow approximately some 'universal' behavior or a corresponding scaling relation.

However, if this central region is excised, the shape of the pressure profiles of clusters closely follow a universal profile, out to a radius of r_{500} (see Fig. 6.45); for larger radii, observations are difficult with the current X-ray observatories, due to the high background and the fact that the X-ray surface brightness decreases steeply for large radii. Hence, once the central region is cut out in the analysis, clusters seem to form a relatively homogeneous class of objects, despite all potential complications of hydrodynamic effects. It is for this reason why clusters can be used for cosmological studies, as we shall describe in Sect. 8.2.

6.5.5 Redshift dependence of scaling relations

The foregoing relations between the quantities of clusters were all obtained for very low-redshift objects. When considering clusters at higher redshift, one might expect that these scaling relations will evolve.

As mentioned before, the virial radius of a cluster is defined by the mean density inside of it being larger than the critical density by about a factor of $\Delta_c \sim 200$. The critical density is a function of redshift, $\rho_{cr}(z) = 3H^2(z)/(8\pi G) = E^2(z)\,\rho_{cr,0}$, where $\rho_{cr,0}$ is the critical density of the current universe [see (4.15)], and $E(z) = H(z)/H_0$. Since ρ_{cr} is larger at higher redshifts, the mean mass density inside clusters also increases, $\langle\rho\rangle = \Delta_c \rho_{cr}(z) \propto E^2(z)$. This affects also the scaling of the characteristic temperature of the cluster,

$$T \propto \frac{M_{vir}}{r_{vir}} = M_{vir}^{2/3} \left(\frac{M_{vir}}{r_{vir}^3}\right)^{1/3} \propto M_{vir}^{2/3} \langle\rho\rangle^{1/3} \propto [M_{vir} E(z)]^{2/3} \,. \tag{6.61}$$

The bolometric X-ray luminosity, assumed to be due to bremsstrahlung only, is the volume integral over the

emissivity (6.32), and so scales like

$$L_{\rm bol} \propto r_{\rm vir}^3 \left\langle n_{\rm e}^2 \right\rangle T^{1/2} \ ,$$

where we assumed a constant temperature of the intracluster gas. If the gas fraction of clusters is a constant, i.e., independent of mass and redshift, then we expect $r_{\rm vir}^3 \left\langle n_{\rm e}^2 \right\rangle \propto M_{\rm vir} \left\langle n_{\rm e}^2 \right\rangle / \langle \rho \rangle \propto M_{\rm vir} \left(\left\langle \rho^2 \right\rangle / \langle \rho \rangle^2 \right) \langle \rho \rangle \propto M_{\rm vir} E^2$, assuming the clumping factor $\left\langle \rho^2 \right\rangle / \langle \rho \rangle^2$ to stay constant. Together with (6.61), we then obtain the expected scaling of the luminosity,

$$\frac{L_{\rm bol}}{E(z)} \propto \left[M_{\rm vir} \, E(z) \right]^{4/3} \ . \tag{6.62}$$

Finally, for the Y-parameter, we have $Y = M_{\rm gas} T \propto M_{\rm vir} \left[M_{\rm vir} \, E(z) \right]^{2/3}$, where we again assumed a constant gas fraction and used (6.61); thus,

$$Y \, E(z) \propto \left[M_{\rm vir} \, E(z) \right]^{5/3} \ . \tag{6.63}$$

These relation generalize (6.52), (6.57) and (6.60) to higher redshifts (note that this redshift dependence was included in Fig. 6.45). If we assume that the profiles of clusters are self-similar, i.e., their density and temperature profiles all have the same shape, but different amplitude and scale length, then these relation do not only apply to the virial radius, but also for regions with different density thresholds.

In detail, these scaling relations are observed to be somewhat different. Whereas the redshift scaling in the mass-temperature relation (6.61) seems to apply to high-redshift clusters, the redshift scaling in the mass-luminosity relation (6.62) is not supported by observations; instead, the redshift evolution is observed to be slower than predicted by the self-similar model. Finally, Fig. 6.46 shows the mass-luminosity relation, where the mass determination was done via weak lensing analysis. Whereas there is a very tight correlation between luminosity and mass, the slope of the best-fitting power law is flatter than predicted by the self-similar behavior (6.62), which probably indicates that clusters are not truly self-similar.

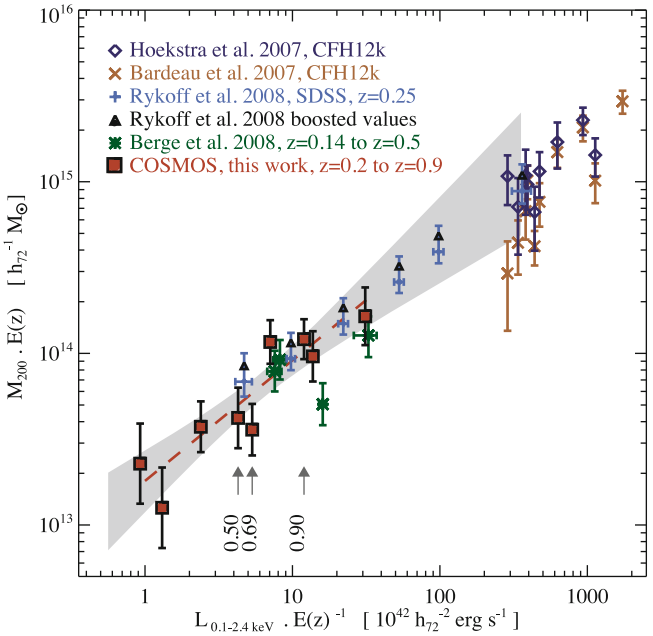

Fig. 6.46 The cluster mass-X-ray luminosity relation, where the mass was determined with weak gravitational lensing methods. *Dark blue diamonds* and *sienna crosses* indicate mass measurements of individual clusters. This is feasible only for high-mass objects. The other data points indicate mean masses of sets of clusters within given L-bins. In particular, the *red squares* were obtained from a weak lensing analysis of X-ray clusters in the COSMOS field, for which the three highest redshift bins are explicitly indicated. The *shaded region* indicates the range which power-law fits within the 1-σ range to the data would cover. Source: A. Leauthaud et al. 2010, *A Weak Lensing Study of X-ray Groups in the Cosmos Survey: Form and Evolution of the Mass-Luminosity Relation*, ApJ 709, 97, p. 109, Fig. 6. ©AAS. Reproduced with permission

6.5.6 Near-infrared luminosity as mass indicator

Whereas the optical luminosity of galaxies depends not only on the mass of the stars but also on the star formation history, the NIR light is much less dependent on the latter. As we have discussed before, the NIR luminosity is thus quite a reliable measure of the total mass in stars. For this reason, we would expect that the NIR luminosity of a cluster is tightly correlated with its total stellar mass. Furthermore, if the latter is closely related to the total cluster mass, as would be the case if the stellar mass is a fixed fraction of the cluster's total mass, the NIR luminosity can be used to estimate the masses of clusters.

The Two Micron All Sky Survey (2MASS) provides the first opportunity to perform such an analysis on a large sample of galaxy clusters. One selects clusters of galaxies for which masses were determined by X-ray methods, and then measures the K-band luminosities of the galaxies within the cluster. Figure 6.47 presents the resulting mass-luminosity diagram within r_{500} for 93 galaxy clusters and groups, where the mass was derived from the clusters' X-ray temperatures (plotted on the top axis) by means of (6.53). A surprisingly close relation between these two parameters is seen, which can be described by a power law of the form

$$\frac{L_{500}}{10^{12} L_\odot} = 3.95 \left(\frac{M_{500}}{2 \times 10^{14} M_\odot} \right)^{0.69} \ , \tag{6.64}$$

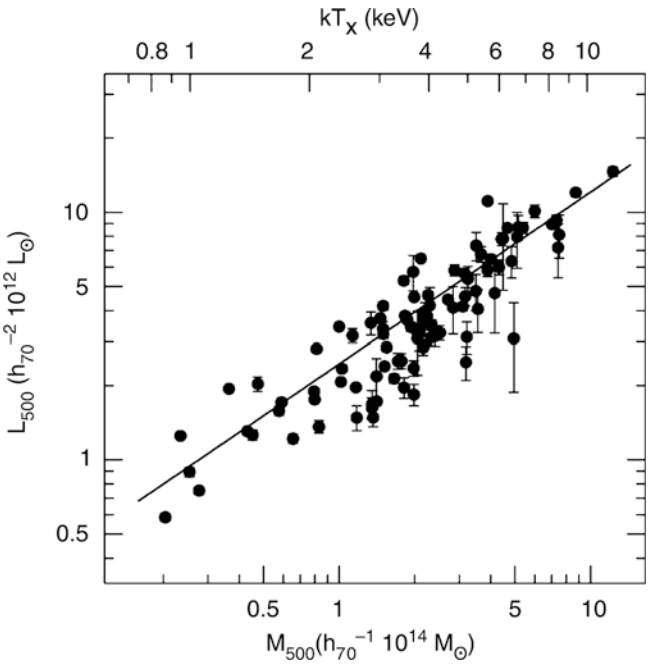

Fig. 6.47 The correlation between K-band luminosity and the mass of galaxy clusters, measured within the radius inside of which the mean density is 500 times the critical density of the Universe. The cluster mass was determined by the relation (6.53) between mass and temperature. Source: Y.-T. Lin et al. 2004, *K-Band Properties of Galaxy Clusters and Groups: Luminosity Function, Radial Distribution, and Halo Occupation Number*, ApJ 610, 745, p. 753, Fig. 3. ©AAS. Reproduced with permission

where a Hubble constant of $h = 0.7$ is assumed. The dispersion of individual clusters around this power law is about 32 %, where at least part of this scatter originates in uncertainties in the mass determination—thus, the intrinsic scatter is even smaller. This result is of great potential importance for future studies of galaxy clusters, and it renders the NIR luminosity a competitive method for the determination of cluster masses, which is of considerable interest in view of the current and future generation of NIR wide-field instruments (like VISTA on Paranal, for instance).

6.6 Clusters of galaxies as gravitational lenses

6.6.1 Luminous arcs

In 1986, two groups independently discovered unusually stretched, arc-shaped sources in two clusters of galaxies at high redshift (see Figs. 6.48 and 6.49). The nature of these sources was unknown at first; they were named *arcs*, or *giant luminous arcs*, which did not imply any interpretation originally. Different hypotheses for the origin of these arcs were formulated, like for instance emission by shock fronts in the ICM, originating from explosive events. All these scenarios were disproven when the spectroscopy of the arc in the cluster Abell 370 showed that the source is at a much higher redshift than the cluster itself. Thus, the arc is a background source, subject to the gravitational lens effect (see Sect. 3.11) of the cluster. By differential light deflection, the light beam of the source can be distorted in such a way that highly elongated arc-shaped images are produced.

The discovery that clusters of galaxies may act as strong gravitational lenses came as a surprise at that time. Based on the knowledge about the mass distribution of clusters, derived from X-ray observations before ROSAT, it was estimated that the central surface mass density of clusters is not sufficiently high for strong effects of gravitational light deflection to occur. This incorrect estimate of the central surface mass density in clusters originated from analyses utilizing the β-model which, as briefly discussed above, starts with some heavily simplifying assumptions.[10]

Hence, arcs are strongly distorted and highly magnified images of galaxies at high redshift. In some massive clusters several arcs were discovered and the unique angular resolution of the HST played a crucial role in such observations. Some of these arcs are so thin that their width is unresolved even by the HST, indicating an extreme length-to-width ratio. For many arcs, additional images of the same source were discovered, sometimes called 'counter arcs'. The identification of multiple images is performed either by optical spectroscopy (which is difficult in general, because one arc is highly magnified while the other images of the same source are considerably less strongly magnified and therefore much fainter in general, together with the fact that spectroscopy of faint sources is very time-consuming), by multi-color photometry (all images of the same source should have the same color), or by common morphological properties.

Lens models. Once again, the simplest mass model for a galaxy cluster as a lens is the singular isothermal sphere (SIS). This lens model was discussed previously in Sect. 3.11.2. Its characteristic angular scale is specified by

[10] Another lesson that can be learned from the discovery of the arcs is one regarding the psychology of researchers. After the first observations of arcs were published, several astronomers took a second look at their own images of these two clusters and clearly detected the arcs in them. The reason why this phenomenon, which had been observed much earlier, was not published before can be explained by the fact that researchers were not completely sure about whether these sources were real. A certain tendency prevails in not recognizing phenomena that occur unexpectedly in data as readily as results which are expected. However, there are also researchers who behave in exactly the opposite manner and even interpret phenomena expected from theory in some unusual way.

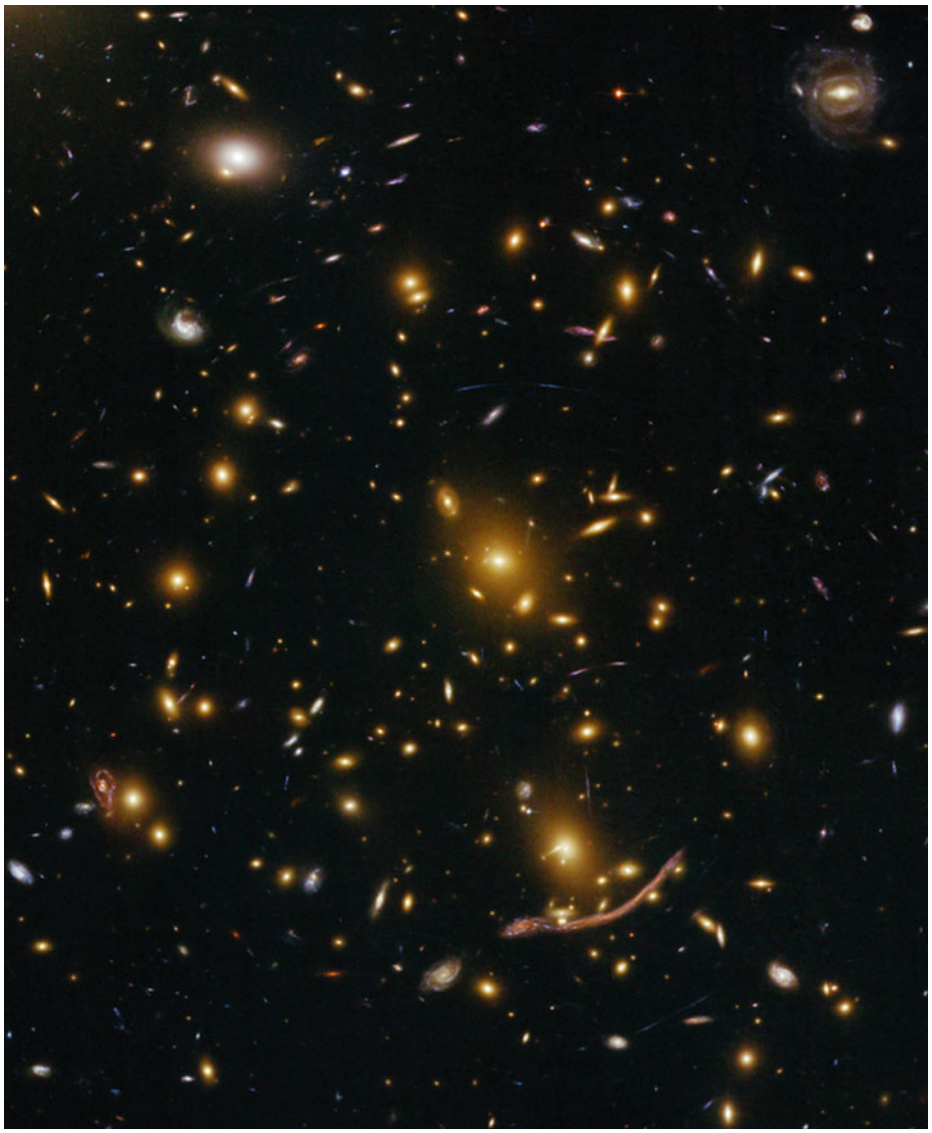

Fig. 6.48 The cluster of galaxies A 370 at redshift $z = 0.375$ is one of the first two clusters in which giant luminous arcs were found in 1986. In this HST image, the arc is clearly visible; it is about 20″ long, tangentially oriented with respect to the center of the cluster which is located roughly halfway between the two brightest cluster galaxies, and curved towards the center of the cluster. The arc is the image of a galaxy at $z_s = 0.724$. Several other very thin arcs are clearly seen, many of which appear in close pairs; in these cases, they are multiple images of the same source galaxy. Only with HST images was it realized how thin these arcs are. One also notes the presence of a 'radial arc', not far from the bright galaxy closest to the major arc. Credit: NASA, ESA, the Hubble SM4 ERO Team, and ST-ECF

the Einstein radius (3.75), or

$$\theta_E = 28''.8 \left(\frac{\sigma_v}{1000\,\mathrm{km/s}} \right)^2 \left(\frac{D_{ds}}{D_s} \right) . \qquad (6.65)$$

Very high magnifications and distortions of images can occur only very close to the Einstein radius. This immediately yields an initial mass estimate of a cluster, by assuming that the Einstein radius is about the same as the angular separation of the arc from the center of the cluster. The projected mass within the Einstein radius can then be derived, using (3.81). Since clusters of galaxies are, in general, not spherically symmetric and may show significant substructure, so that the separation of the arc from the cluster center may deviate significantly from the Einstein radius, this mass estimate is not very accurate in general; the uncertainty is presumably $\sim 30\,\%$. Models with asymmetric mass distributions predict a variety of possible morphologies for the arcs and the positions of multiple images, as is demonstrated in Fig. 6.50 for an elliptical lens. If several arcs are discovered in a cluster, or several images of the source of an arc, we can investigate detailed mass models for such a cluster. The accuracy of these models depends on the number and positions of the observed lensed images; e.g., on how many arcs and how many multiple image systems are available for modeling. The resulting mass models are not unambiguous, but they are robust. Clusters that contain many lensed images have very well-determined mass properties, for instance the mass and the mass profile within the radii at which arcs are found, or the ellipticity of the mass distribution and its substructure.

Figure 6.51 shows two clusters of galaxies which contain several arcs. The lensing mass estimate of the cluster Cl 0024+17 is quite different from the mass obtained through an X-ray analysis. Spectroscopy of its member galaxies show

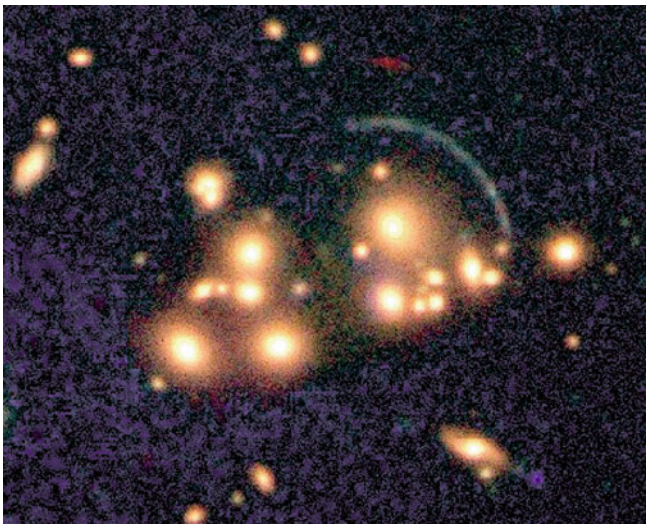

Fig. 6.49 The cluster of galaxies Cl 2244−02 at redshift $z = 0.33$ is the second cluster in which an arc was discovered. Spectroscopic analysis of this arc revealed the redshift of the corresponding source to be $z_s = 2.24$—at the time of discovery in 1987, it was the first normal galaxy detected at a redshift > 2. This image was observed with the near-IR camera ISAAC at the VLT. Above the arc, one can see another strongly elongated red source which is probably associated with a galaxy at very high redshift as well. Credit: European Southern Observatory

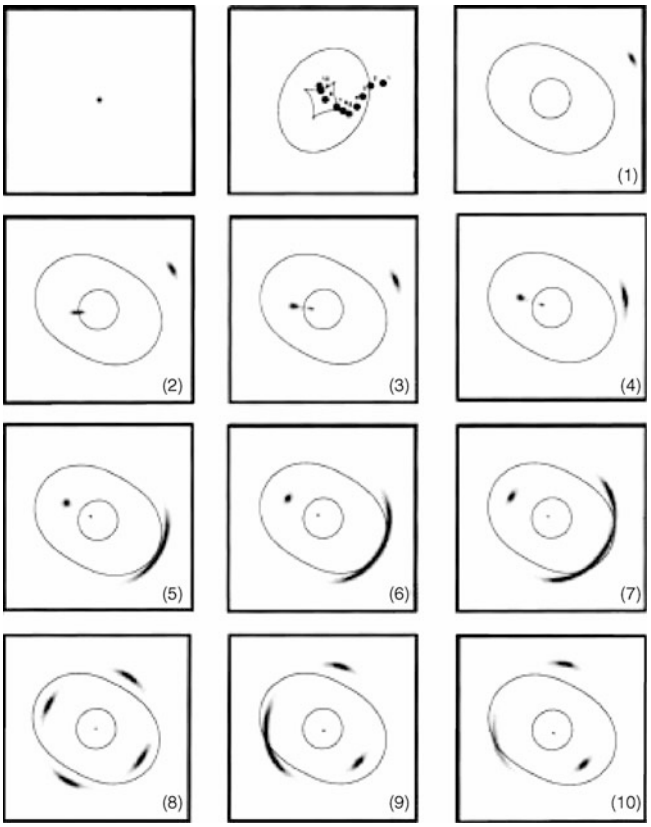

Fig. 6.50 Distortions by the lens effect of an elliptical potential, as a function of the source position. The *first panel* shows the source itself. The *second panel* displays ten positions of the source in the source plane (numbered from 1 to 10) relative to the center of the lens; the *solid curves* show the inner and outer caustics. The remaining panels (numbered from 1 to 10) show the inner and outer critical curves and the resulting images of the source. Source: B. Fort & Y. Mellier 1994, *Arc(let)s in clusters of galaxies*, A&AR 5, 239. © Springer-Verlag. Reproduced with permission

evidence for a bimodal distribution in velocity space which is interpreted as the cluster being indeed a pair of clusters, colliding along the line-of-sight. If this interpretation is correct, the mass estimate from X-rays is expected to yield discordant values.

For a long time, A 2218 was the classic example of the existence of numerous arcs in a single galaxy cluster. Then after the installation of the ACS camera on-board HST in 2002, a spectacular image of the cluster A 1689 was obtained in which more than 100 arcs and multiple images were identified (see Fig. 6.52). Several zoomed sections of this image are shown in the lower part of the figure. For clusters of galaxies with such a rich inventory of lens phenomena, very detailed mass models can be constructed.

Such mass models have predictive power, allowing an iterative modeling process. An initial simple mass model is fitted to the most prominent lensed images in the observation, i.e., either giant arcs or clearly recognizable multiple images. In general, this model then predicts further images of the source producing the arc. Close to these predicted positions, these additional images are then searched for, utilizing the morphology of the light distribution and the color. If this initial model describes the overall mass distribution quite well, such images are found. The exact positions of the new images provide further constraints on the lens model which is then refined accordingly. Again, the new model will predict further multiple image systems, and so on. By this procedure, very detailed models can sometimes be obtained. Since the lens properties of a cluster depend on the distance or the redshift of the source, the redshift of lensed sources can be predicted from the identification of multiple image systems in clusters if a detailed mass model is available. These predictions can then be verified by spectroscopic analysis, and the success of this method gives us confidence in the accuracy of the lens models.

Results. We can summarize the most important results of the examination of clusters using arcs and multiple images as follows: the mass of galaxy clusters is indeed much larger than the mass of their luminous matter. The lensing method yields a mass which is in very good agreement with mass estimates from the X-ray method or from dynamical methods. However, the core radius of clusters, i.e., the scale on which the mass profile flattens inwards, is significantly smaller than determined from X-ray observations. If the mass distribution in clusters has a core, its size is estimated to be $r_c \sim 30h^{-1}$ kpc, in contrast to $\sim 150h^{-1}$ kpc obtained from

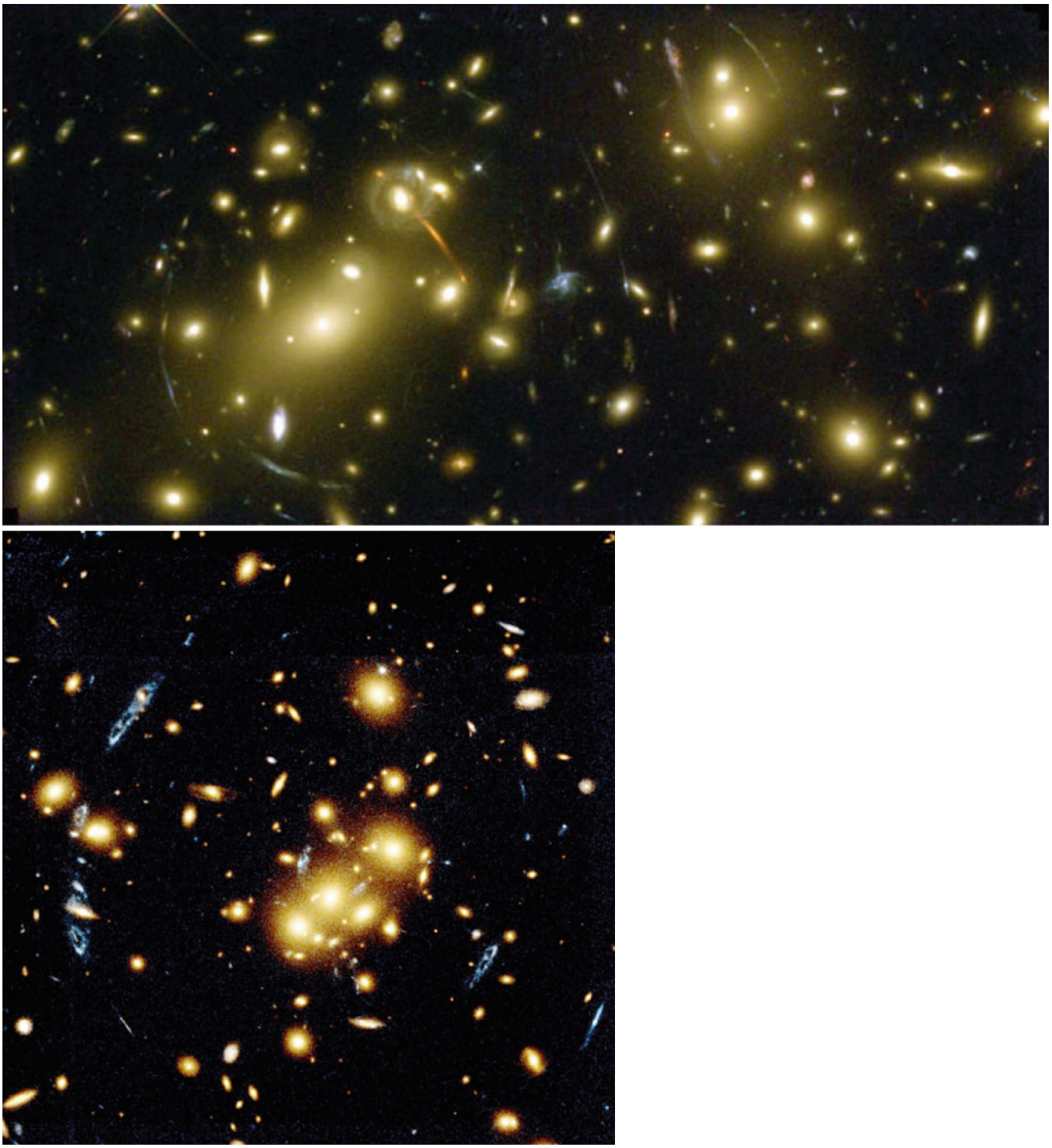

Fig. 6.51 *Top*: the cluster of galaxies A 2218 ($z_d = 0.175$) contains one of the most spectacular arc systems. The majority of the galaxies visible in the image are associated with the cluster, and the redshifts of many of the strongly distorted arcs have now been measured. *Bottom*: the cluster of galaxies Cl 0024+17 ($z_d = 0.39$) contains a rich system of arcs. The arcs appear bluish, stretched in a direction which is tangential to the cluster center. The three arcs to the left of the cluster center, and the arc to the right of it and closer to the center, are images of the same background galaxy which has a redshift of $z_s = 1.62$. Another image of the same source was found close to the cluster center. Also note the identical ('pretzel'-shaped) morphology of the images. Credit: *Top*: W. Couch/University of New South Wales, R.S. Ellis/Cambridge University and NASA. *Bottom*: W.N. Colley and E. Turner/Princeton University, J.A. Tyson/Bell Labs, Lucent Technologies, and NASA

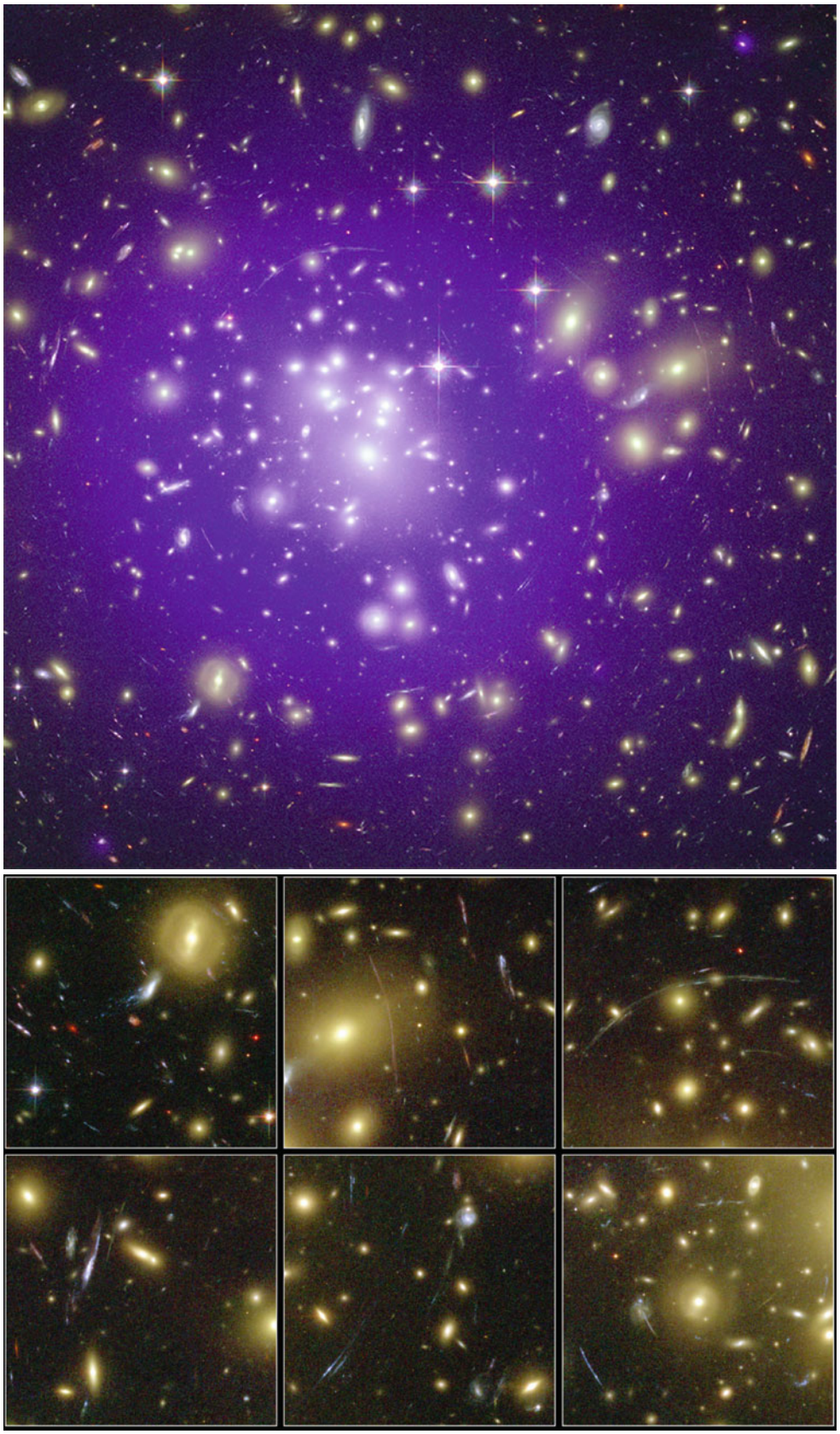

Fig. 6.52 The cluster of galaxies Abell 1689 has one of the richest system of arcs and multiple images found to date. In a deep ACS exposure of this cluster, shown *on top* with the X-ray emission superimposed in *blue*, more than a hundred such lensed images were detected. Six zoomed sections of this ACS image are shown in the *bottom part*, in which various arcs are visible, some with an extreme length-to-width ratio, indicating very high magnification factors. Credit: X-ray: NASA/CXC/MIT/E.-H. Peng et al.; optical: NASA, N. Benitez/JHU, T. Broadhurst/Racah Institute of Physics/The Hebrew University, H. Ford/JHU, M. Clampin/STScI, G. Hartig/STScI, G. Illingworth/UCO/Lick Observatory, the ACS Science Team and ESA

early X-ray analyses.[11] This difference leads to a discrepancy in the mass determination between the two methods on scales below $\sim 200h^{-1}$ kpc.

We emphasize that, at least in principle, the mass determination based on arcs and multiple images is substantially more accurate because it does not require any assumptions about the symmetry of the mass distribution, about hydrostatic equilibrium of the X-ray gas, or about an isothermal temperature distribution. On the other hand, the lens effect measures the mass in cylinders because the lens equation contains only the projected mass distribution, whereas the X-ray method determines the mass inside spheres. The conversion between the two methods introduces uncertainties, in particular for clusters which deviate significantly from spherical symmetry. Overestimating the core radius was the main reason why the discovery of the arcs was a surprise because clusters with core radii like the ones determined from the early X-ray measurements would in fact not act as strong gravitational lenses. Hence, the mere existence of arcs shows that the core radius must be small.

A closer analysis of galaxy clusters with a cool core shows that, in these clusters, the mass profile estimated from X-ray observations is compatible with the observed arcs. Such clusters are considered dynamically relaxed, so that for them the assumption of a hydrostatic equilibrium is well justified. The X-ray analysis has to account explicitly for the existence of an inner cool region, though, and the accordingly modified X-ray emission profile is more sophisticated than the simple β-model. Clusters without a cool core are distinctly more complex dynamically. Besides the discrepancy in mass determination, lensing and X-ray methods can lead to different estimates of the center of mass in such unrelaxed clusters, which may indicate that the gas has not had enough time since the last strong interaction or merging process to settle into an equilibrium state.

As we mentioned before, the cluster Cl 0024+17 in Fig. 6.51 most likely has a complex structure along the line-of-sight, and hence it is not surprising that X-ray estimated masses deviate significantly from those obtained by lensing. As a second example, the cluster A 1689 (Fig. 6.52) presumably also has a complex structure. A combined lensing, X-ray and SZ-study of this cluster suggests that it is highly elongated, with an axis ratio of ~ 2 and the long axis close to the line of sight. This orientation maximizes the lensing strength of a triaxial mass distribution, and clusters selected by their strong lensing features will be biased towards these orientations. In order to account for the differences in mass estimates from these different methods, one concludes that the gas is not in hydrostatic equilibrium, but there must be substantial fraction of non-thermal pressure in that cluster, e.g., from turbulent motions of the intracluster gas.

The mass distribution in clusters often shows significant substructure. Many clusters of galaxies in which arcs are observed are not relaxed. These clusters still undergo dynamical evolution—they are young systems with an age not much larger than $t_{\rm cross}$, or systems whose equilibrium was disturbed by a fairly recent merger process. For such clusters, the X-ray method is not well founded because the assumptions about symmetry and equilibrium are not satisfied. The distribution of arcs in the cluster A2218 (Fig. 6.51) clearly indicates a non-spherical mass distribution. Indeed, this cluster seems to consist of at least two massive components around which the arcs are curved, indicating that the cluster is currently undergoing a strong merging event. This is further supported by measurements of the temperature distribution of the intracluster gas, which shows a strong peak in the center, where the temperature is about a factor of two higher than in its surrounding region.

From lens models, we find that for clusters with a central cD galaxy, the orientation of the mass distribution follows that of the cD galaxy quite closely. We conclude from this result that the evolution of the brightest cluster galaxy must be closely linked to the evolution of the cluster, e.g., by accretion of a cooling flow onto the BCG or due to mergers with other cluster members. Often, the shape of the mass distribution very well resembles the galaxy distribution and the X-ray emission.

> The investigation of galaxy clusters with the gravitational lens method provides a third, completely independent method of determining cluster masses. It confirms that the mass of galaxy clusters significantly exceeds that of the visible matter in stars and in the intracluster gas. We conclude from this result that clusters of galaxies are dominated by dark matter.

6.6.2 The weak gravitational lens effect

The principle of the weak lensing effect. In Sect. 3.11 we saw that gravitational light deflection does not only deflect light beams as a whole, but also that the size and shape of light beams are distorted by differential light deflection. This differential light deflection leads, e.g., to sources appearing brighter than they would be without the lens effect. The giant arcs discussed above are a very clear example of these distortions and the corresponding magnifications.

If some background sources exist which are distorted in such an extreme way as to appear as giant luminous arcs, then it is plausible that many more background galaxies should exist which are less strongly distorted. Typically, these are

[11] We will see in the next chapter that the density of dark matter halos is predicted to increase right to the center, i.e., no core is formed in this case.

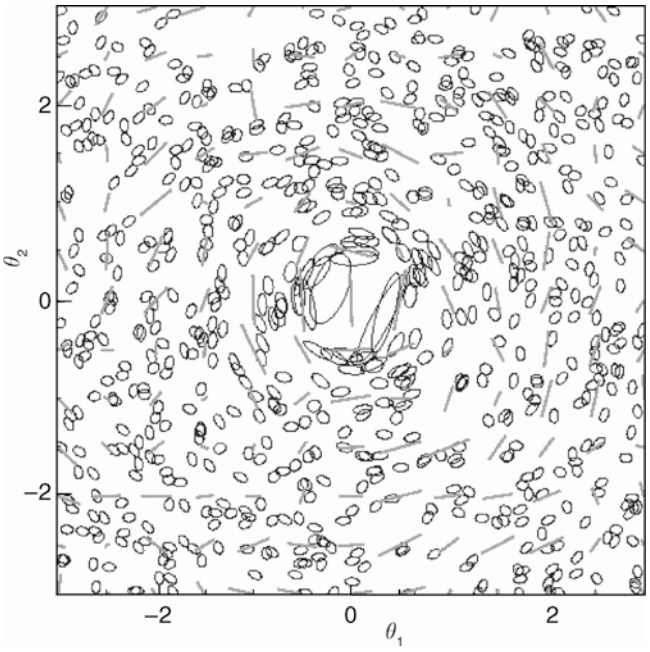

Fig. 6.53 The principle of the weak gravitational lensing effect is illustrated here with a simulation. Due to the tidal component of the gravitational field in a cluster, the shape of the images (ellipses) of background galaxies get distorted and, as for arcs, the galaxy images will be aligned, on average, tangentially to the cluster center. By local averaging over the ellipticities of galaxy images, a local estimate of the tidal gravitational field can be obtained (the direction of the sticks indicates the orientation of the tidal field, and their length is proportional to its strength). From this estimated tidal field, the projected mass distribution can then be reconstructed. Source: C. Seitz, *The determination of the mass distribution in clusters of galaxies by gravitationally distorted images of background galaxies*, Dissertation, LMU München, 1996

located at larger angular separations from the cluster center, where the lens effect is weaker than at the locations of the luminous arcs. Their distortion then is so weak that it cannot be identified in an individual galaxy image. The reason for this is that the intrinsic light distribution of galaxies is not circular; rather, the observed image shape is a superposition of the intrinsic shape and the gravitational lens distortion. The former is considerably larger than the latter, in general, and acts as a kind of noise in the measurement of the lensing effect. However, the distortion of adjacent galaxy images should be similar since the gravitational field their light beams are traversing is similar. By averaging over many such galaxy images, the distortion can then be measured (see Fig. 6.53) because no preferred direction exists in the intrinsic orientation of galaxies; it is expected to be random. After the results from the Hubble Deep Field (Fig. 1.37) became available, if not before, we have known that the sky is densely covered by small, faint galaxies. In deep optical images, one therefore finds a high number density of such galaxies located in the background of a galaxy cluster. Their measured shapes can be used for investigating the weak lensing effect of the cluster.

The distortion, obtained by averaging over image ellipticities, reflects the contribution of the tidal forces to the local gravitational field of the cluster. In this context, it is denoted as *shear*. It is given by the projection of the tidal component of the gravitational field along the line-of-sight. The shear results from the derivative of the deflection angle, where the deflection angle (3.62) depends linearly on the surface mass density of the lens. Hence, it is possible to reconstruct the surface mass density of galaxy clusters in a completely parameter-free way using the measured shear: it can be used to map the (total, i.e., dark plus luminous) matter in a cluster.

Observations. Since shear measurements are based on averaging over image ellipticities of distant galaxies, this method of *weak gravitational lensing* requires optical images with as high a galaxy density as possible. This implies that the exposures need to be very deep to reach very faint magnitudes. But since very faint galaxies are also very distant and, as a consequence, have small angular extent, the observations need to be carried out under very good observing conditions, to be able to accurately measure the shape of galaxy images without them being smeared into circular images by atmospheric turbulence, i.e., the seeing. Typically, to apply this method images from 4-m class telescopes are used, with exposure times of 1–3 h. This way, we reach a density of about 30 galaxies per square arcminute (thus, 10^5 per square degree) of which shapes are sufficiently well measurable. This corresponds to a limiting magnitude of about $R \sim 25$. The seeing during the exposure should not be larger than $\sim 0''.8$ to still be able to correct for effects of the point-spread function. The smaller the seeing, the more galaxy images can be used for the weak lensing analysis.

Systematic observations of the weak lensing effect only became feasible with the development of wide-field cameras.[12] This, together with the improvement of the dome seeing at many telescopes and the development of dedicated software for data analysis, rendered quantitative observational studies with weak lensing possible; the best telescopes at the best observatories regularly accomplish seeing below $0''.8$, and the dedicated software is specifically designed for measuring the shapes of extremely faint galaxy images and for correcting for the effects of seeing and anisotropy of the point spread function.

Mass reconstruction of galaxy clusters. By means of this method, the reconstruction of the mass density of a large

[12] Prominent examples for such cameras are Megacam at CFHT, the first square degree camera with $\sim (18000)^2$ pixels, and OmegaCAM (with the same field-of-view) at the VLT Survey Telescope on Paranal. The largest camera currently in operation is that of Pan-STARRS1, covering $\sim 6\,\mathrm{deg}^2$

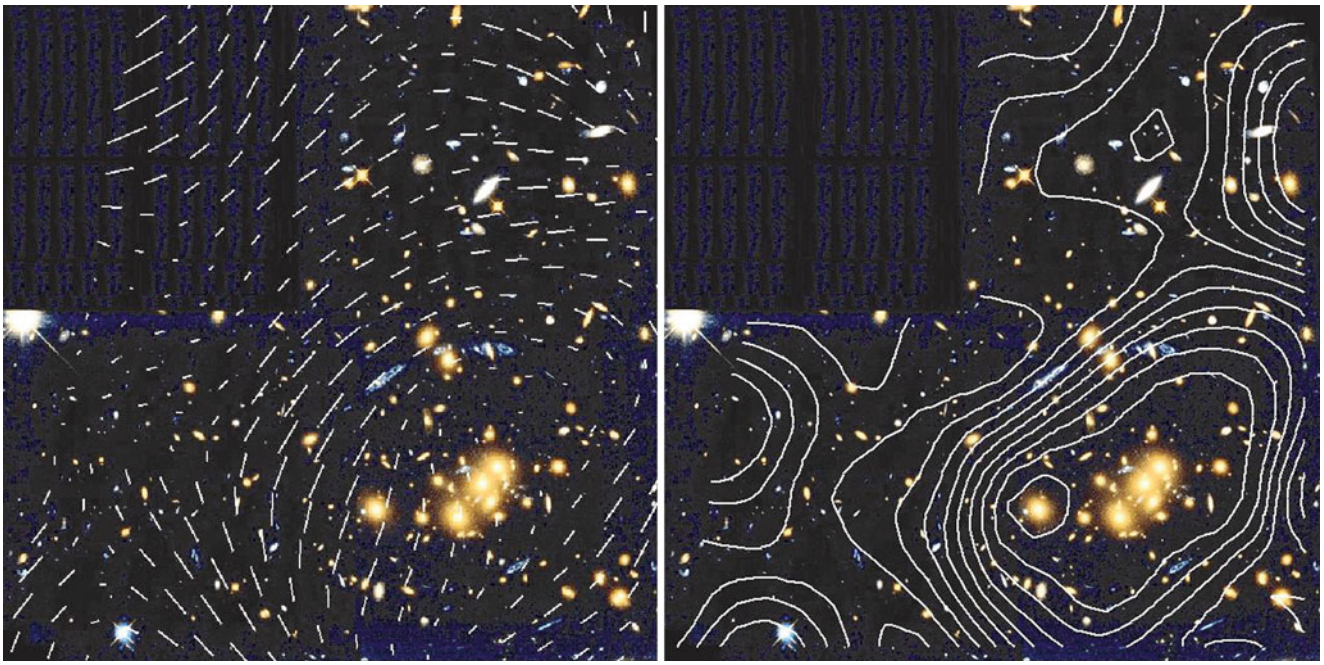

Fig. 6.54 *On the left*, the tidal (or shear) field of the cluster Cl 0024+17 (Fig. 6.51) is indicated by sticks whose length and direction represent the strength and orientation of the tidal gravitational field. *On the right*, the surface mass density is shown, reconstructed by means of the weak gravitational lens effect. The bright galaxies in the cluster are seen to follow the (dark) matter distribution; the orientation of the isodensity contours is the same as the orientation of the light in the center of the cluster. Credit: optical image: HST/NASA, Colley et al.; shear field and mass reconstruction: C. Seitz, *The determination of the mass distribution in clusters of galaxies by gravitationally distorted images of background galaxies*, Dissertation, LMU München, 1996

number of clusters became possible. The most important results of these investigations are as follows: the center of the mass distribution corresponds to the optical center of the cluster (see Fig. 6.54). If X-ray information is available, the mass distribution is, in general, found to be centered on the X-ray maximum, except in clusters which are heavily disturbed. The shape of the mass distribution—e.g., its ellipticity and orientation—is in most cases very similar to the distribution of bright cluster galaxies. The comparison of the mass profile determined by this method and that determined from X-ray data agree well, typically within a factor of ~ 1.5; we will discuss mass profiles of clusters from weak lensing further below (Sect. 7.7) where we compare them with cosmological predictions.

Through the weak lensing effect, substructure in the mass distribution is also detected in some clusters (Fig. 6.55) which does not in all cases reflect the distribution of cluster galaxies. However, in general a good correspondence between light and mass exists (Fig. 6.56). From these lensing studies, we obtain a mass-to-light ratio for clusters that agrees with that found from X-ray analyses, about $M/L \sim 250h$ in Solar units. Clusters of galaxies that strongly deviate from this average value do exist, however. Two independent analyses for the cluster MS 1224+20 resulted in a mass-to-light-ratio of $M/L \approx 800h$ in Solar units, more than twice the value normally found in clusters.

The similarity of the mass and galaxy distributions is not necessarily expected because the lens effect measures the total mass distribution, and therefore mainly the dark matter in a cluster of galaxies. The similar distributions then imply that the galaxies in a cluster seem to basically follow the distribution of the dark matter (Sect. 7.6.1), although there are some exceptions.

Bullet clusters, and the nature of dark matter. Figure 6.34 shows the X-ray emission and the galaxy distribution of the so-called Bullet cluster, actually a system of two clusters which have recently collided. Besides the hydrodynamic effects of the collision, this system is of great interest to test for the nature of the discrepancy between the observed mass in clusters (from the stars in the member galaxies and the intracluster gas) and the gravitational mass deduced from the X-ray emission, the galaxy peculiar velocities in clusters, and the lensing results. If this discrepancy is due to a modification of the law of gravity on large scales, as was speculated, then we expect that the bulk of the mass in the Bullet cluster is centered on the X-ray emitting gas, since its mass is several times higher than that of the stars in the cluster galaxies. On the other hand, if the discrepancy is due to (collisionless) dark matter, then this dark matter should behave similarly to the galaxies in a collision: the scattering cross section is very small, and

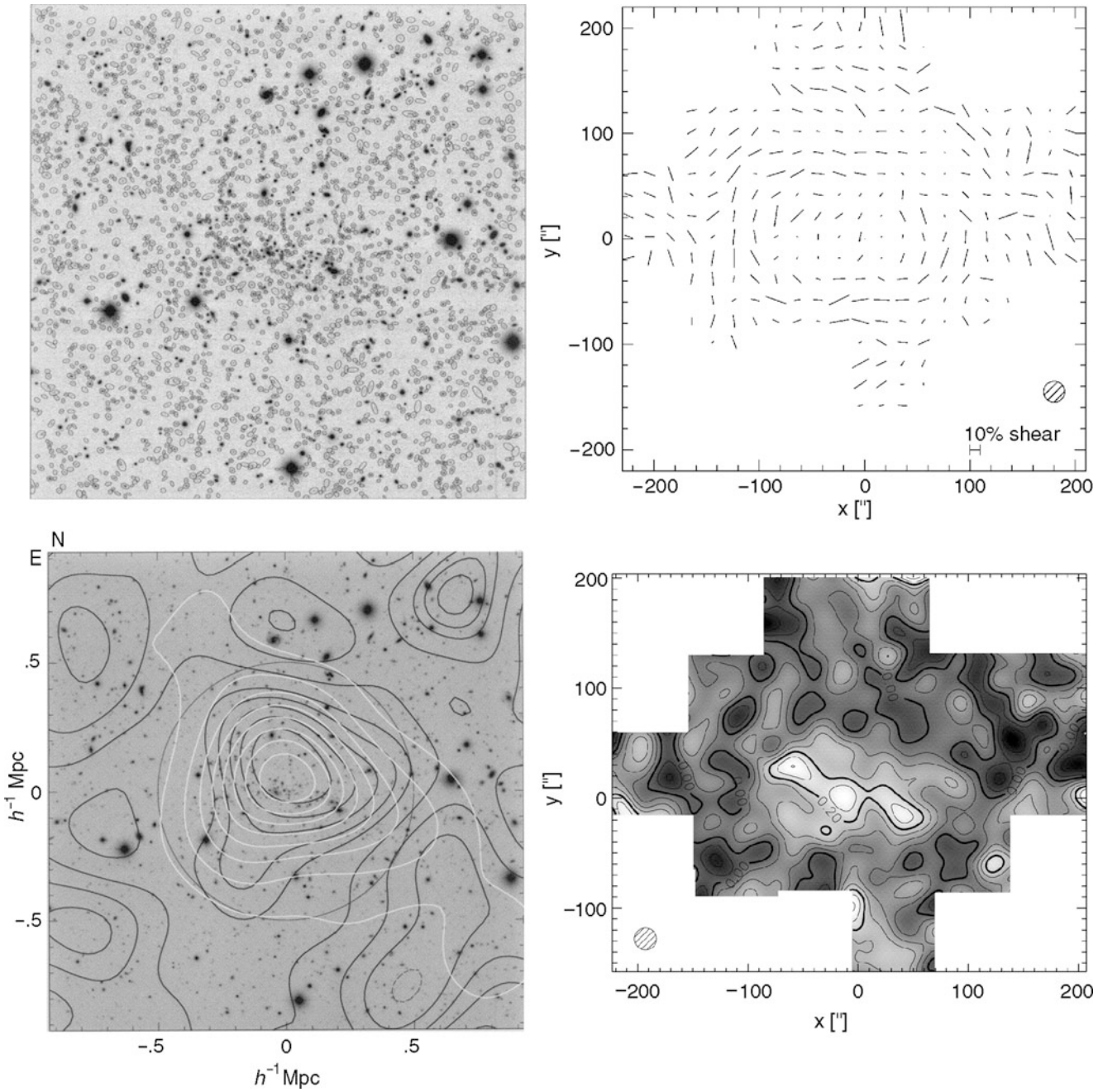

Fig. 6.55 Analysis of the cluster of galaxies MS 1054−03 by the weak lensing effect. In the *upper left panel*, a ground-based image is shown with a field size of 7′.5 × 7′.5. In this image, about 2400 faint objects are detected, the majority of which are galaxies at high redshift. From the measured ellipticities of the galaxies, the tidal field of the cluster can be reconstructed, and from this the projected mass distribution $\Sigma(\boldsymbol{\theta})$, presented in the *lower left panel*; the latter is indicated by the black contours, while the white contours represent the smoothed light distribution of the cluster galaxies. A mosaic of HST images allows the ellipticity measurement of a significantly larger number of galaxies, and with better accuracy. The tidal field resulting from these measurements is displayed in the *upper right panel*, with the reconstructed surface mass density shown in the *lower right panel*. One can clearly see that the cluster is strongly structured, with three density maxima which correspond to regions with bright cluster galaxies. This cluster seems to be currently in the process of formation through a merger of smaller entities. Source: *Left*: G.A. Luppino & N. Kaiser 1997, *Detection of Weak Lensing by a Cluster of Galaxies at* $z = 0.83$, ApJ 475, 20, PLATE 2, 3, Figs. 3, 5. ©AAS. Reproduced with permission. *Right*: H. Hoekstra et al. 2000, *Hubble Space Telescope Weak-Lensing Study of the* $z = 0.83$ *Cluster MS 1054–03*, ApJ 532, 88, p. 94, 96, Figs. 9, 12. ©AAS. Reproduced with permission

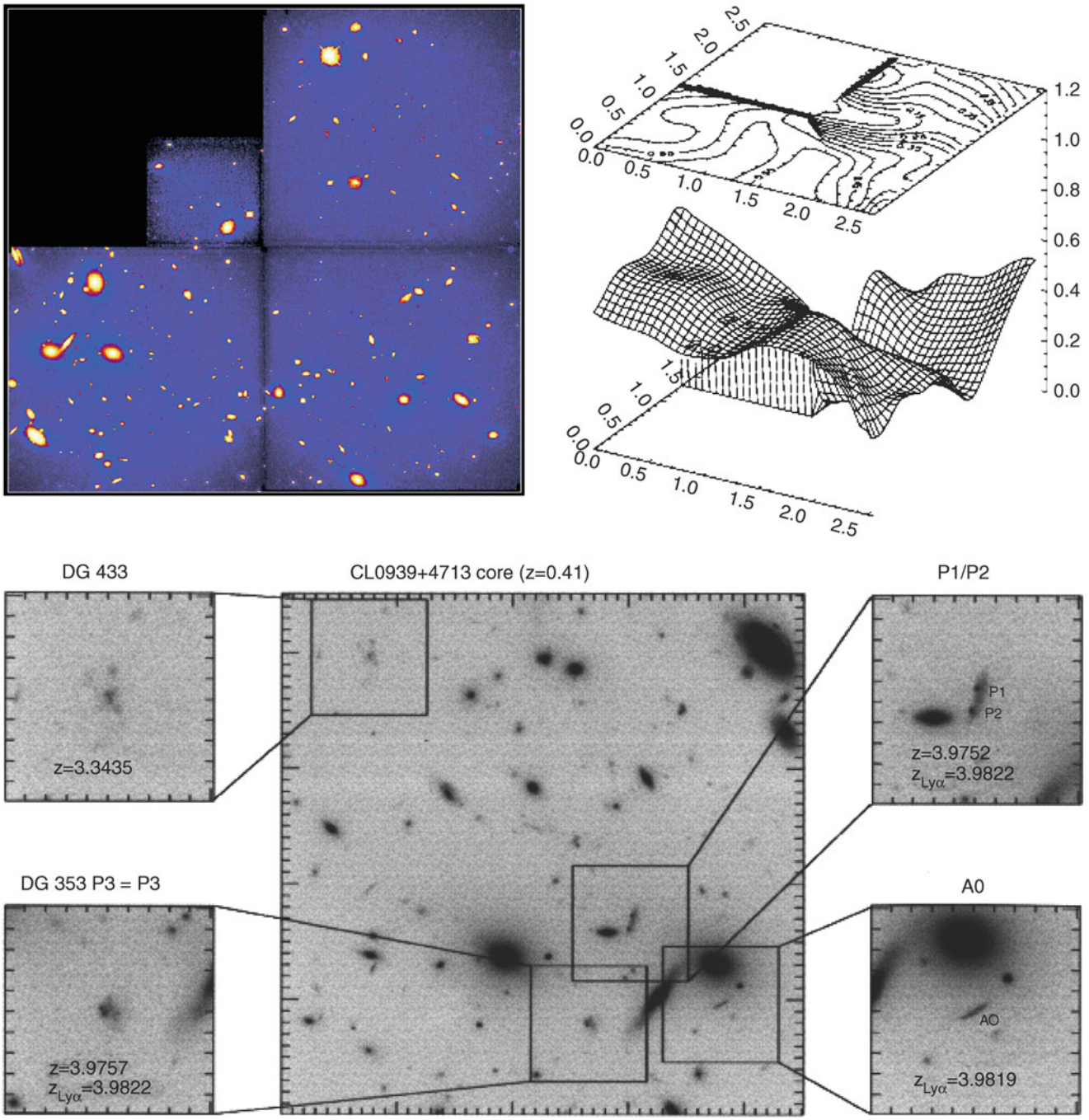

Fig. 6.56 The cluster of galaxies Cl 0939+4713 (A851) is the cluster with the highest redshift in the Abell catalog. The HST image in the *upper left panel* was obtained shortly after the refurbishment of the HST in 1994; in this image, North is down, whereas it is up in the *bottom images*. The mass distribution of the cluster was reconstructed from this image and is shown in the *upper right panel*, both as the level surface and by the contours on top. We see that the distributions of bright galaxies and of (dark) matter are very similar: their respective centers are aligned, a secondary maximum exists in both the light and the matter distribution, as does the prominent minimum in which no bright galaxies are visible either. A higher-resolution mass map from the weak lensing data predicts that the cluster is critical near its center, i.e., able to produce strong lensing features. Indeed, these were observed, as can be seen from the image at the *bottom*: a triple image system at $z \approx 3.98$ and an arc with $z = 3.98$ were confirmed spectroscopically. Source: *Top*: C. Seitz et al. 1996, *The mass distribution of CL0939+4713 obtained from a 'weak' lensing analysis of a WFPC2 image.*, A&A 314, 707, p. 708, 712, Figs. 1, 5. ©ESO. Reproduced with permission. *Bottom*: S.C. Trager et al. 1997, *Galaxies at* $z \approx 4$ *and the Formation of Population II*, ApJ 485, 92, p. 93, Fig. 1. ©AAS. Reproduced with permission

Fig. 6.57 The Bullet cluster, shown before in Fig. 6.34. In *red*, the X-ray emission is shown, superposed on the HST image of the cluster. In *blue*, the weak lensing mass reconstruction is shown, which is located on the galaxy concentrations of the two colliding clusters. Credit: X-ray: NASA/CXC/CfA/M. Markevitch et al.; Optical: NASA/STScI; Magellan/U. Arizona/D. Clowe et al.; Lensing Map: NASA/STScI; ESO WFI; Magellan/U.Arizona/D. Clowe et al.

thus the dark matter components of both colliding clusters (like the galaxies) just run through each other. So: where's the mass?

This question can be answered unambiguously with the weak lensing effect; the result is displayed in Fig. 6.57. The mass is centered on the galaxy distributions of the two clusters, and clearly displaced from the X-ray emitting gas. Therefore, the mass discrepancy cannot be ascribed to a modification of the law of gravity; instead, the main mass component of the clusters must behave very similarly as the galaxies, i.e., collisionless. Thus, the Bullet cluster provides the clearest direct proof for the existence of dark matter. Whereas the Bullet cluster was the first of its kind, in the meantime other cluster collisions have been investigated as well. Two other clusters with very similar behavior are shown in Fig. 6.58.

The weak lensing results from clusters in collision cannot be explained without the existence of collisionless dark matter in galaxy clusters, even if modifications of the law of gravity on large scales were allowed for.

Dark matter filaments between cluster pairs. The hierarchical structure growth in the Universe, a consequence of the Cold Dark Matter model, predicts that mass concentrations form near the intersection points of dark matter filaments, through which they accrete mass (see Chap. 7). These filaments in general have a density too low to produce a detectable weak lensing signal. However, if two large mass concentrations, such as two clusters, are relatively close to each other, the density of the filament between them is expected to be considerably higher than in the mean. Therefore, pairs of galaxy clusters are the best locations to look for dark matter filaments that connect the members of the pair. Indeed, several attempts for the detection of such filaments have been made, using weak lensing techniques; in most of the cases the significance of the detection is rather low. However, for the best case up to now, the double cluster Abell 222+223, there is a convincing detection of a filament (see Fig. 6.59). In addition, the location of the filament coincides with an overdensity of galaxies and soft X-ray emission. Therefore, this system may be the first detection of a dark matter filament.

Mass calibration of clusters. We saw that the mass determination of clusters from their X-ray emission is far from trivial, owing to the complexity of the baryonic physics affecting the intracluster gas, at least in the inner region of clusters. Any systematic uncertainty in the mass estimate affects the scaling relations, which are an essential tool for cluster cosmology (see Sect. 8.2). Gravitational lensing offers an alternative possibility for determining cluster masses which is independent of equilibrium and symmetry assumptions. The accuracy of weak lensing masses for individual clusters, out to large radii (e.g., within r_{500}), is not impressive, and is affected by the noise caused by intrinsic galaxy ellipticity, light deflection by other masses along the line-of-sight to the source population, and the mass-sheet degeneracy (see Problem 3.5). However, the mean mass of a statistical sample of clusters can be obtained by using the superposition of the individual lensing signals. The mass estimate from such a 'stacked' cluster profile is viewed as

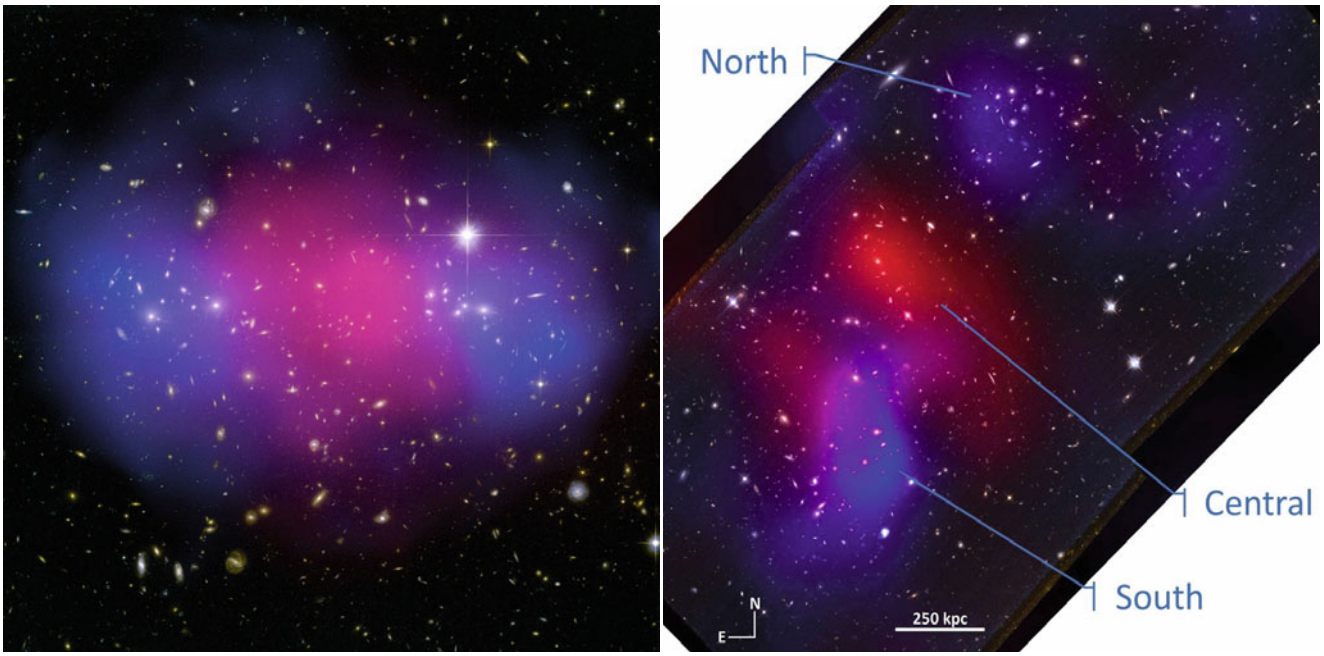

Fig. 6.58 Two clusters which are similar to the Bullet cluster. *Left panel*: The cluster MACS J0025.4−1222 has undergone a recent collision between two separate clusters. The two galaxy concentrations are seen at the left and right side of the optical image, which was taken with the HST. Shown in *pink* is the X-ray emission from this cluster, observed with Chandra. Using the weak lensing technique, the mass distribution of this cluster was reconstructed and is shown in *blue*. As for the Bullet cluster, the total mass distribution traces that of the galaxies, and is very different from the distribution of the hot intracluster gas. *Right panel*: The merging cluster DLSCL J0916.2+2951 at $z = 0.53$ also has its hot gas (indicated by the X-ray emission shown in *red*) displaced from the two concentrations of cluster galaxies, denoted by 'North' and 'South' in the image. In *blue*, the weak lensing mass reconstruction of this cluster is shown, again centered on the galaxy concentrations and clearly displaced from the intracluster gas. Credit: *Left*: NASA, ESA, CXC, M. Bradac (University of California, Santa Barbara), and S. Allen (Stanford University). *Right*: W.D. Dawson et al. 2012, *Discovery of a Dissociative Galaxy Cluster Merger with Large Physical Separation*, ApJ 747, L42, p. 2, Fig. 1. ©AAS. Reproduced with permission

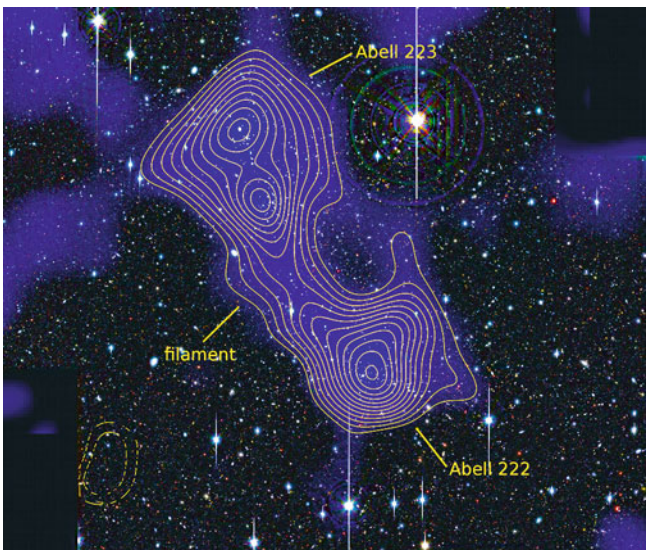

Fig. 6.59 The pair of clusters Abell 222 and 223, as observed with the Subaru telescope, with the superimposed matter distribution (*blue shades* and *yellow contours*). The filament between the pair of clusters is clearly indicated. Credit: Jörg Dietrich, University of Michigan/University Observatory Munich

being least affected by systematic effects, and therefore frequently employed in constructing scaling relations. In Sect. 7.7 we will present results of such studies.

The search for clusters of galaxies with weak gravitational lensing. The weak lensing effect can not only be used to map the matter distribution of known clusters, but it can also be employed to search for clusters. Mass concentrations generate a tangentially oriented shear field in their vicinity, which can specifically be searched for. The advantage of this method is that it detects cluster-mass matter concentrations based solely on their mass properties, in contrast to all other methods which rely on the emission of electromagnetic radiation, whether in the form of optical light from cluster galaxies or as X-ray emission from a hot intracluster medium. In particular, if clusters with atypically low gas or galaxy content exist, they could be detected in this way.

Quite a number of galaxy clusters have been detected with this method—see Fig. 6.60. Further candidates exist, where the shear signal indicates a significant mass concentration but it cannot be identified with any concentration of galaxies on

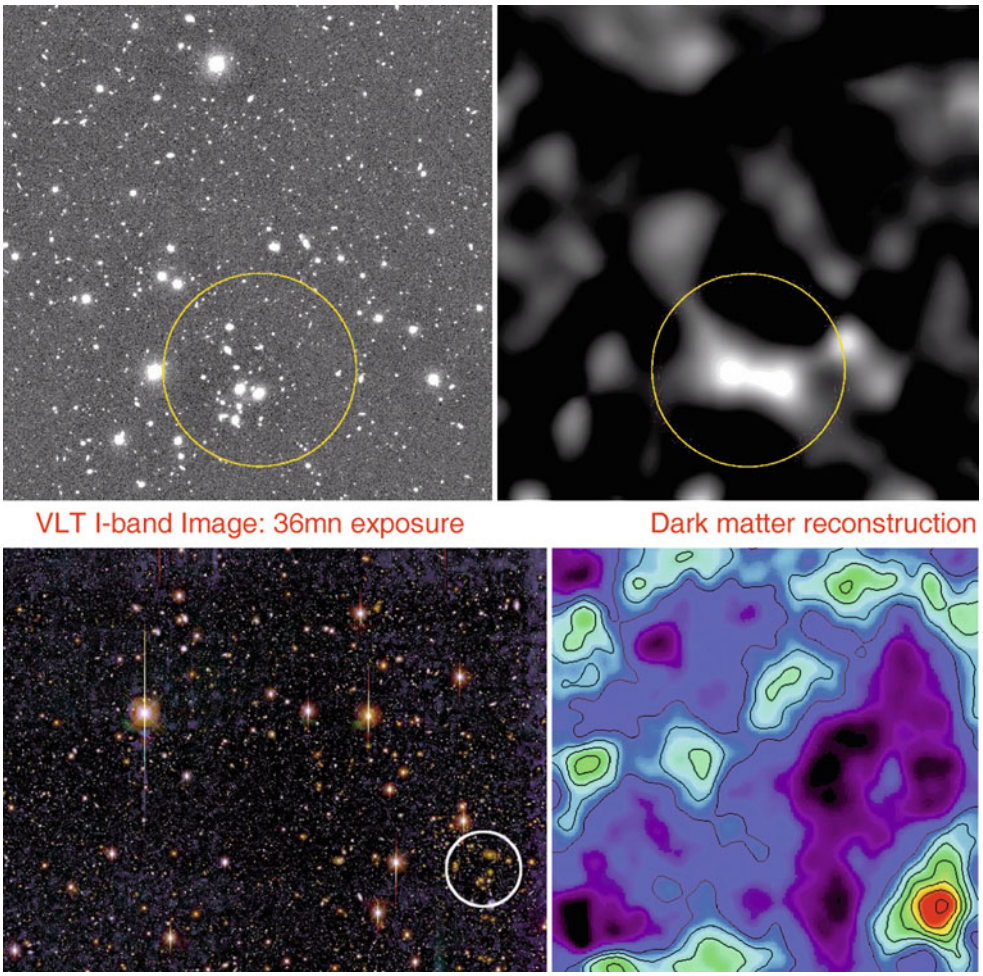

Fig. 6.60 *Top left*: a VLT/FORS1 image, taken as part of a survey of 'empty fields'. *Top right*: the mass reconstruction, as was obtained from the optical data by employing the weak lensing effect. Clearly visible is a peak in the mass distribution; the optical image shows a concentration of galaxies in this region. Hence, in this field a cluster of galaxies was detected for the first time by its lens properties. *Bottom*: as above, here a galaxy cluster was also detected through its lensing effect. *On the left*, an optical wide-field image is shown, obtained by the Big Throughput Camera, and the mass reconstruction is displayed *on the right*. The location of the peak in the latter coincides with a concentration of galaxies. Spectroscopic measurements yield that these form a cluster of galaxies at $z = 0.276$. Credit: *Top*: R. Maoli et al., ESO. *Bottom*: D. Wittman/Lucent Technologies' Bell Labs, et al., NOAO, AURA, NSF

optical images. The clarification of the nature of these lens signals is of great importance: if in fact matter concentrations do exist which correspond to the mass of a cluster but which do not contain luminous galaxies, then our understanding of galaxy evolution needs to be revised. However, we cannot exclude the possibility that these statistically significant signals are statistical outliers, or result from projection effects—remember, lensing probes the line-of-sight integrated matter density. Together with the search for galaxy clusters by means of the SZ-effect (Sect. 6.4.4), the weak lensing effect provides an interesting alternative for the detection of mass concentrations compared to the more traditional methods.

6.7 The galaxy population in clusters

6.7.1 Luminosity function of cluster galaxies

The luminosity function of galaxies in a cluster is defined in a similar way as in Sect. 3.10 for the total galaxy population. In many clusters, the Schechter luminosity function (3.52) represents a good fit to the data if the brightest galaxy is disregarded in each cluster (see Fig. 3.51 for the Virgo cluster of galaxies). The slope α at the faint end is not easy to determine, since projection effects become increasingly important for fainter galaxies. The value of α seems to vary between clusters, but it is not entirely clear whether this result may also be affected by projection effects of differing strength in different clusters. Thus, no final conclusion has been reached as to whether the luminosity function has a steep increase at $L \ll L^*$ or not, i.e., whether many more faint galaxies exist than luminous $\sim$L*-galaxies (compare the galaxy content in the Local Group, Sect. 6.1.1, where even in our close neighborhood it is difficult to obtain a complete census of the galaxy population). L^* is very similar for many clusters, which is the reason why the distance estimate by apparent brightness of cluster members, as done by Abell for his cluster catalog, is quite reliable, though a number of clusters exists with a clearly deviating value of L^*.

However, when averaging over many clusters, the picture becomes much clearer. The luminosity function of galaxies changes as one moves from field galaxies, through groups, to clusters. This change is already noticeable for poor groups with just a few galaxies, such as the Local Group. The

faint-end slope of the luminosity function is flatter in group and cluster environments than for field galaxies, and flattens with increasing cluster mass or richness. Most galaxies with $L \lesssim L^*$ live either in isolation or in relatively poor groups, whereas the most luminous galaxies are predominantly found in the central regions of rich groups and clusters. Whereas the fraction of elliptical galaxies is much smaller in low-density regions than in the inner part of clusters, they nevertheless dominate the galaxy mix at the highest luminosities.

Brightest Cluster Galaxies. Of special interest in clusters is the Brightest Cluster Galaxy (BCG), which in most cases is located near the center of the cluster. In many cases, the BCG is a *cD galaxy*; these differ from large ellipticals in several respects. They have a very extended stellar envelope, whose size may exceed $R \sim 100\,\mathrm{kpc}$ and whose surface brightness profile is much broader than that of a de Vaucouleurs-profile (see Fig. 3.11). cD galaxies are found only in the centers of clusters or groups, thus only in regions of strongly enhanced galaxy density. However, the extended stellar envelope merges into the intracluster light, and there is some ambiguity to distinguish between cD envelope and ICL, as discussed in Sect. 6.3.4. Many cD galaxies have multiple cores, which is a rather rare phenomenon among the other cluster members.

BCGs are very luminous and massive; their typical stellar mass is $M_* \sim 2 \times 10^{11} h^{-2} M_\odot$, with a spread of about a factor of 1.5. One finds that the more massive clusters contain the more luminous BCGs. At first sight, this is not too surprising, since the more galaxies a cluster contains, the larger is the probability to find one of them with very high stellar mass (or luminosity). However, there are several indications that this cannot be the sole reason. First, in most clusters, the second brightest cluster galaxy is about 1 mag or more fainter than the BCG, which cannot be explained purely by statistical arguments. Second, the BCGs appear to be not simply the extension of early-type galaxies towards the highest luminosity; for example, BCGs do not fall right on the fundamental plane for ellipticals. Their size-luminosity relation is different from that of ellipticals, in the sense that they are larger than ellipticals with the same luminosity.

6.7.2 The morphology-density relation

As mentioned several times before, the mixture of galaxy types in clusters seems to differ from that of isolated (field) galaxies. Whereas about 70 % of luminous field galaxies are spirals, clusters are dominated by early-type galaxies, in particular in their inner regions. Furthermore, the fraction of spirals in a cluster depends on the distance from the center and increases for larger r. Obviously, the local density has an effect on the morphological mix of galaxies. As in clusters, the fraction of group members which are spirals is lower than the fraction of spirals among field (i.e., isolated) galaxies, and the relative abundance of spiral galaxies decreases with increasing σ_v of the group.

More generally, one may ask whether the mixture of the galaxy population depends on the local galaxy density. While earlier studies of this effect were frequently confined to galaxies within and around clusters, extensive redshift surveys like the 2dFGRS and the SDSS (see Sect. 8.1.2) allow us to systematically investigate this question with very large and carefully selected samples of galaxies. The morphological classification of such large samples is performed by automated software tools, which basically measure the light concentration in the galaxies, or, alternatively, the best-fitting Sérsic-index n [see (3.39)]. A comparison of galaxies classified this way with visual classifications shows very good agreement.

Results from the Sloan Digital Sky Survey. As an example of such an investigation, results from the Sloan Digital Sky Survey are shown in Fig. 6.61. Galaxies were morphologically classified, based on SDSS photometry, and separated into four classes, corresponding to elliptical galaxies, S0-galaxies, and early (Sa) and late (Sc) types of spiral. In this analysis, only galaxies were included for which the redshift was spectroscopically measured. Therefore, the spatial galaxy density can be estimated. However, one needs to take into account the fact that the measured redshift is a superposition of the cosmic expansion and the peculiar velocity of a galaxy. The peculiar velocity may have rather large values ($\sim 1000\,\mathrm{km/s}$), in particular in clusters of galaxies. For this reason, for each galaxy in the sample the surface number density of galaxies which have a redshift within $\pm 1000\,\mathrm{km/s}$ of the target galaxy was determined. The left panel in Fig. 6.61 shows the fraction of the different galaxy classes as a function of this local galaxy density. A very clear dependence, in particular of the fraction of late-type spirals, on the local density can be seen: in regions of higher galaxy density Sc-spirals contribute less than 10 % of the galaxies, whereas their fraction is about 30 % in low-density regions. Combined, the fraction of spirals decreases from $\sim$ 65 % in the field to about 35 % in regions of high galaxy density. In contrast, the fraction of ellipticals and S0-galaxies increases towards higher densities, with the increase being strongest for ellipticals.

In the right-hand panel of Fig. 6.61, the mixture of galaxy morphologies is plotted as a function of the distance to the center of the nearest cluster, where the distance is scaled by the virial radius of the corresponding cluster. As expected, a very strong dependence of the fraction of ellipticals and spirals on this distance is seen. Sc-spirals contribute a mere 5 % of galaxies in the vicinity of cluster centers, whereas

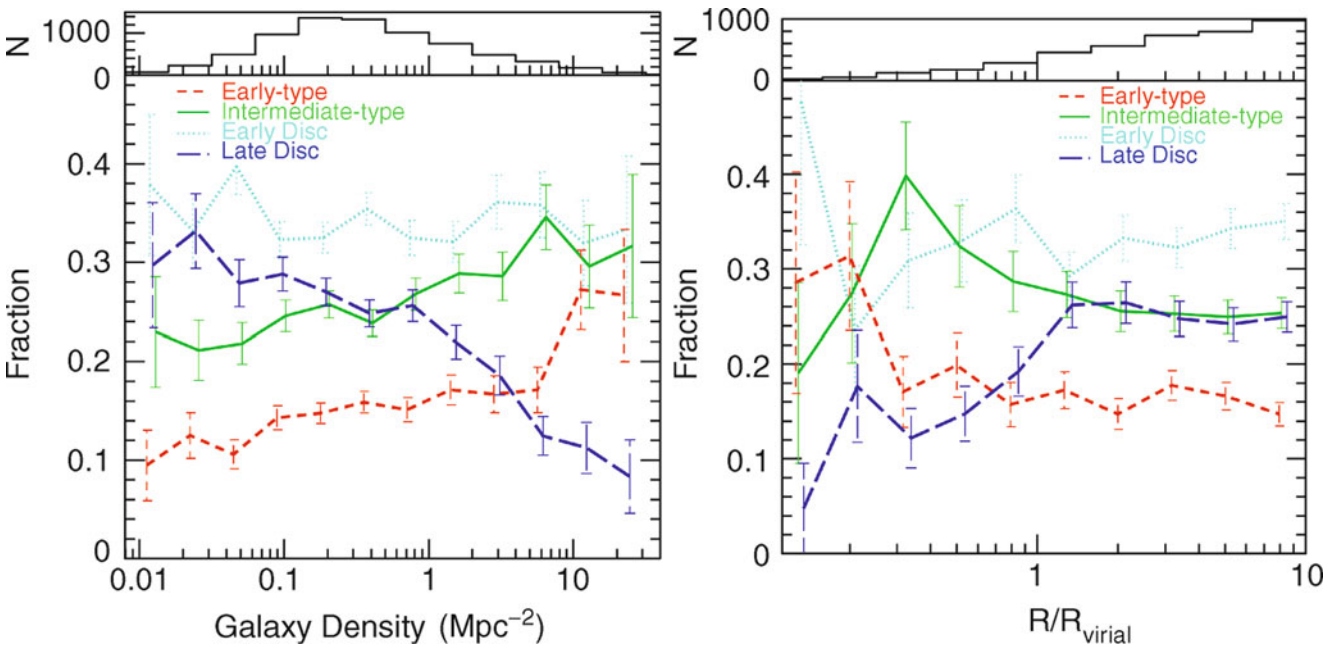

Fig. 6.61 The number fraction of galaxies of different morphologies is plotted as a function of the local galaxy density (*left panel*), and for galaxies in clusters as a function of the distance from the cluster center, scaled by the corresponding virial radius (*right panel*). Galaxies are divided into four different classes. 'Early-types' contain mainly ellipticals, 'intermediates' are mainly S0-galaxies, 'early and late discs' are predominantly Sa- and Sc-spirals, respectively. In both representations, a clear dependence of the galaxy mix on the density or on the distance from the cluster center, respectively, is visible. In the histograms at the top of each panel, the number of galaxies in the various bins is plotted. Source: T. Goto et al. 2003, *The morphology-density relation in the Sloan Digital Sky Survey*, MNRAS 346, 601, p. 607, 608, Figs. 12, 15. Reproduced by permission of Oxford University Press on behalf of the Royal Astronomical Society

the fraction of ellipticals and S0-galaxies strongly increases inwards.

The two diagrams in Fig. 6.61 are of course not mutually independent: a region of high galaxy density is very likely to be located in the vicinity of a cluster center, and the opposite is valid accordingly. Therefore, it is not immediately clear whether the mix of galaxy morphologies depends primarily on the respective density of the environment of the galaxies, or whether it is caused by morphological transformations in the inner regions of galaxy clusters.

The morphology-density relation is also seen in galaxy groups. The fraction of late-type galaxies decreases, and the fraction of early-type galaxies increases with decreasing distance from the group center, as is also the case in clusters. When considering the morphological mix of visually classified early- and late-type galaxies, averaged over the whole group or cluster, i.e., up to the virial radius, then it seems to be constant for group/cluster halo masses in excess of $\sim 10^{13} M_{\odot}$.

Alternative consideration: the color-density relation. We pointed out in Sect. 3.1.3 that galaxies at fixed luminosity seem to have a bimodal color distribution (see Fig. 3.7). Using the same data set as that used for Fig. 3.7, the fraction of galaxies that are contained in the red population can be studied as a function of the local galaxy density. The result of this study is shown in the left-hand panel of Fig. 6.62, where the fraction of galaxies belonging to the red population is plotted against the local density of galaxies, measured in terms of the fifth-nearest neighboring galaxy within a redshift of $\pm 1000\,\mathrm{km/s}$. The fraction of red galaxies increases towards higher local number density, and the relative increase is stronger for the less luminous galaxies. If we identify the red galaxies with the early-type galaxies in Fig. 6.61, these two results are in qualitative agreement. Surprisingly, the fraction of galaxies in the red sample seems to be a function of a combination of the local galaxy density and the luminosity of the galaxy, as is shown in the right-hand panel of Fig. 6.62.

Interpretation. A closer examination of Fig. 6.61 may provide a clue as to what physical processes are responsible for the dependence of the morphological mix on the local number density. We consider first the right-hand panel of Fig. 6.61. Three different regimes in radius can be identified: for $R \gtrsim R_{\mathrm{vir}}$, the fraction of the different galaxy types remains basically constant. In the intermediate regime, $0.3 \lesssim R/R_{\mathrm{vir}} \lesssim 1$, the fraction of S0-galaxies strongly increases inwards, whereas the fraction of late-type spirals decreases accordingly. This result is compatible with the interpretation that in the outer regions of galaxy clusters spirals lose gas,

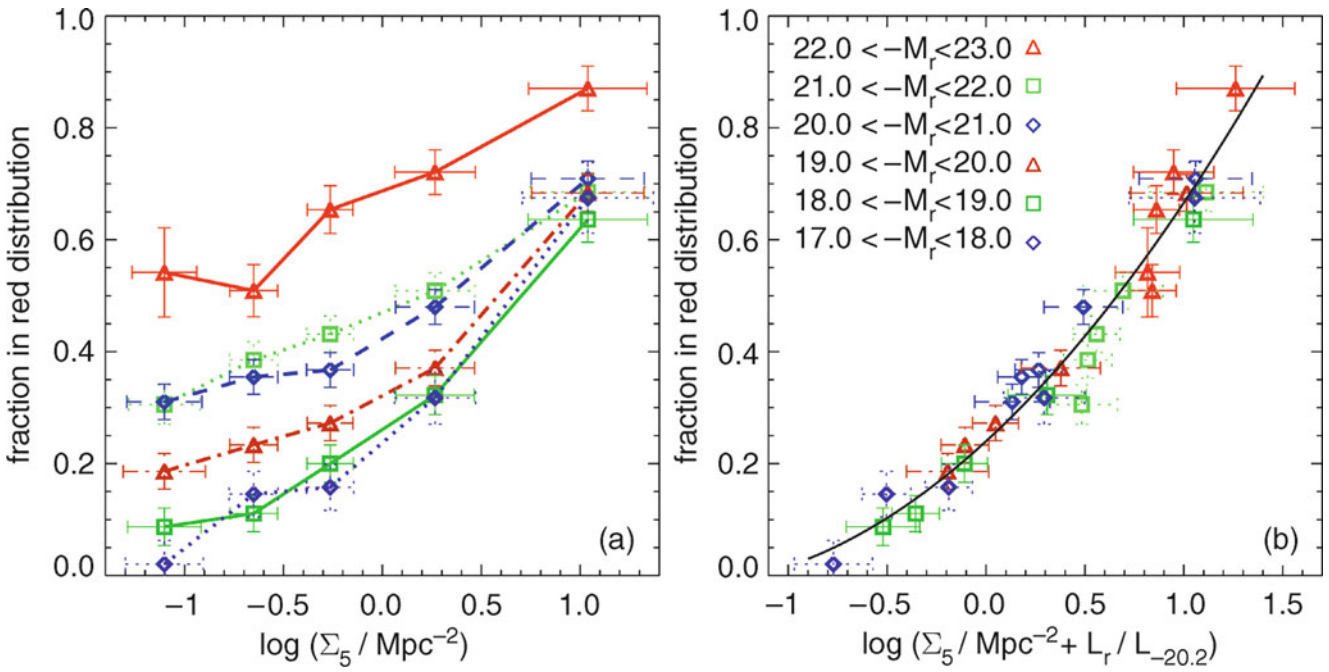

Fig. 6.62 *On the left*, the fraction of galaxies in the red population (see Sect. 3.1.3) is shown as a function of Σ_5, an estimator of the local galaxy number density based on the projected distance of the fifth-nearest spectroscopically confirmed neighbor galaxy within ± 1000 km/s. Different symbols correspond to different luminosity bins, as indicated. *On the right*, the same red fraction is plotted against a combination of the local galaxy density Σ_5 and the luminosity of the galaxy. Source: I.K. Baldry et al. 2004, *Color bimodality: Implications for galaxy evolution*, astro-ph/0410603, Fig. 6. Reproduced by permission of the author

for instance by their motion through the intergalactic medium (see Fig. 6.63), and these galaxies then transform into passive S0-galaxies. Below $R \lesssim 0.3 R_{\rm vir}$, the fraction of S0-galaxies decreases strongly, and the fraction of ellipticals increases substantially.

In fact, the ratio of the number densities of S0-galaxies and ellipticals, for $R \lesssim 0.3 R_{\rm vir}$, strongly decreases as R decreases. This may hint at a morphological transformation in which S0 galaxies are turned into ellipticals, probably by collisions or mergers. Such gas-free mergers, also called 'dry mergers', may be the preferred explanation for the generation of elliptical galaxies. One of the essential properties of dry mergers is that such a merging process would not be accompanied by a burst of star formation, unlike the case of gas-rich collisions of galaxies. The existence of a population of newly-born stars in ellipticals would be difficult to reconcile with the generally old stellar population actually observed in these galaxies. We will discuss these issues more thoroughly in Chap. 10.

Considering now the dependence on local galaxy density (the left-hand panel of Fig. 6.61), a similar behavior of the morphological mix of galaxies is observed: there seem to exist two characteristic values for the galaxy density where the relative fractions of galaxy morphologies change noticeably. Interestingly, the relation between morphology and density seems to evolve only marginally between $z = 0.5$ and the local Universe.

One clue as to the origin of the morphological transformation of galaxies in clusters, as a function of distance from the cluster center, comes from the observation that the velocity dispersion of very bright cluster galaxies seems to be significantly smaller than that of less luminous ones. Assuming that the mass-to-light ratio does not vary substantially among cluster members, this then indicates that the most massive galaxies have smaller velocity dispersions. One way to achieve this trend in the course of cluster evolution is by dynamical interactions between cluster galaxies. Such interactions tend to 'thermalize' the velocity distribution of galaxies, so that the mean kinetic energy of galaxies tends to become similar. This then causes more massive galaxies to become slower on average. If this interpretation holds, then the morphology-density relation may be attributed to these dynamical interactions, rather than to the (so-called ram-pressure) stripping of the interstellar medium as the galaxies move through the intracluster medium.

However, ram-pressure stripping of the interstellar medium has been clearly observed in clusters. In Fig. 6.63, two edge-on spiral galaxies in the Virgo cluster are shown, both in the optical and in the radio. The impact of the intracluster medium, which acts like a 'wind' in the rest-frame of the galaxies, can be clearly seen. This effect mostly acts on the atomic gas of spirals, whereas the molecular gas seems to be less affected; we recall that the molecular gas is more densely concentrated towards the

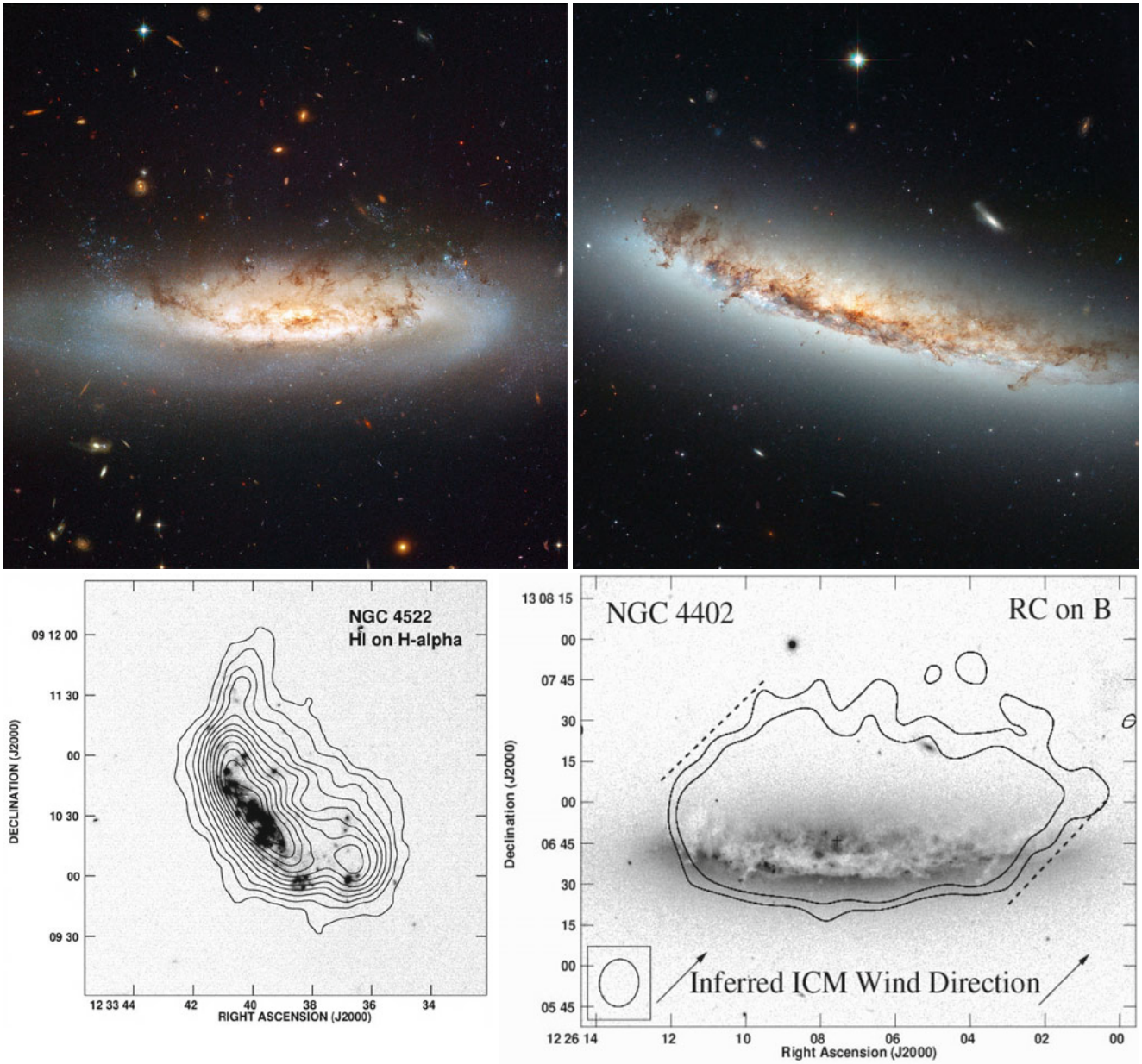

Fig. 6.63 Two edge-on spiral galaxies in the Virgo cluster, NGC 4522 (*left*) and NGC 4402 (*right*). The *top panels* show multi-color composite images of these two galaxies, taken with the HST. The high velocity of the galaxies moving through the intracluster gas removes part of the interstellar medium through ram pressure stripping; in addition, the interaction of the intracluster gas with the ISM of the galaxies triggers star formation, as can be seen by the blue knots of emission downstream (i.e., above the disk). The *bottom panels* show the neutral hydrogen gas (*left*, for NGC 4522) and the 20 cm radio emission (*right*, for NGC 4022) of these two galaxies (note that the orientation of these images are different from those of the HST images). The gas is distributed asymmetrically with respect to the galactic disk, emphasizing the stripping of gas from the galaxies. In the *bottom right*, the *arrows* indicate the direction of the ICM velocity as seen in the rest-frame of the galaxy (i.e., the galaxy moves in the opposite direction to these *arrows*). Credit: *Top panels*: NASA & ESA. *Bottom left*: B. Vollmer et al. 2008, *Ram-pressure stripped molecular gas in the Virgo spiral galaxy NGC 4522*, A&A 491, 455, p. 461, Fig. 13. ©ESO. Reproduced with permission. Bottom right: H.H. Crowl 2005, *Dense Cloud Ablation and Ram Pressure Stripping of the Virgo Spiral NGC 4402*, AJ 130, 65, p. 68, Fig. 3. ©AAS. Reproduced with permission

galactic disk, and thus more strongly bound. In fact, it has been known for a long time that there are spiral galaxies in groups and clusters which are deficient in neutral hydrogen, relative to field galaxies of the same stellar luminosity. If ram-pressure stripping, or other effects in the dense cluster environment, removes the interstellar medium from spirals, then the result could be a disk galaxy without ongoing star formation—something that may resemble an S0-galaxy. If that were the case, than S0s would be passively fading former spirals. Whereas the original spirals satisfied the

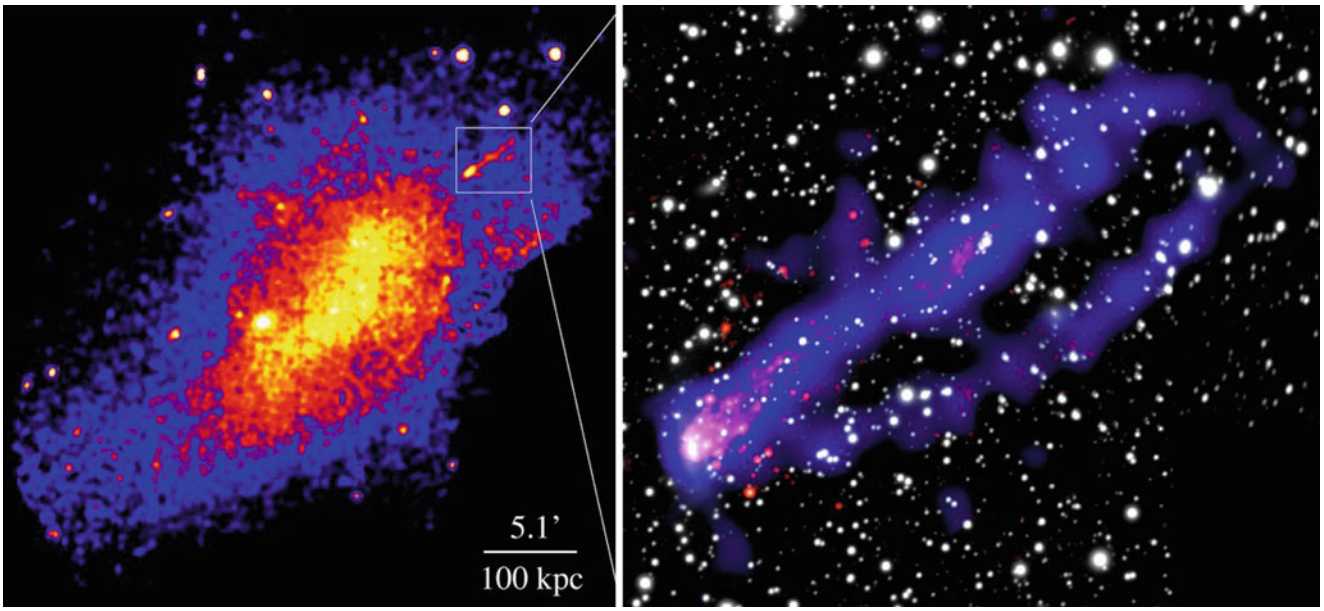

Fig. 6.64 The *left panel* shows an XMM-Newton image of the cluster Abell 3627. *On the right*, the region highlighted in the *left panel* is zoomed in, showing the X-ray emission as observed with Chandra (in *blue*), a narrow-band optical image centered on the Hα line in *red*, both of which are superposed on the broad-band optical image of the cluster (in *white*; obtained with the SOAR telescope in Chile). The X-ray image clearly shows two tails, with some 80 kpc length, originating from the galaxy ESO 137-001 located on the left in this image. These tails are generated by ram-pressure stripping caused by the hot intracluster medium (seen through its X-ray emission in the *left panel*), as the galaxy moves towards the central region of the cluster. The stripped gas is heated to temperatures of $\sim$ 1 keV, about a factor of 10 smaller than the temperature of the hot intracluster medium. The Hα emission is mainly caused by H II regions and thus indicates regions of star formation. Hence, new stars are formed in the gas that is removed from the galaxy. These stars will contribute to the intracluster light. Furthermore, 19 X-ray point sources were found around the X-ray tails, some of them being candidates for ultra-luminous X-ray sources (ULX). Together, this observation shows a clear connection between the evolution of galaxies in clusters and the intracluster medium. Credit: X-ray: NASA/CXC/UVa/M. Sun, et al.; H-alpha/Optical: SOAR (UVa/NOAO/UNC/CNPq-Brazil). Corresponding journal article: M. Sun et al. 2010, *Spectacular X-ray Tails, Intracluster Star Formation, and ULXs in A3627*, ApJ 708, 946, p. 949, Fig. 2. ©AAS. Reproduced with permission

Tully–Fisher relation, the S0s would then be expected to be considerably fainter than spirals, at fixed rotational velocity; this indeed is the case.

Ram-pressure stripping not only removes gas from cluster galaxies, but can heat the gas and also trigger local star formation, though the compression of gaseous regions by the pressure. A spectacular example for this is shown in Fig. 6.64. The newly formed stars are no longer gravitationally bound to the galaxy, and will thus contribute to the ICL in the cluster.

E + A galaxies. Galaxy clusters contain a class of galaxies which is defined in terms of spectral properties. These galaxies, which are rare in number, show strong Balmer line absorption in their spectra, characteristic of A stars, but no [OII] or Hα emission lines. The latter indicates that these galaxies are not undergoing strong star formation at present (since there are no HII regions around O- and B-stars), whereas the former shows that there was an episode of star formation within the past $\sim$ 1 Gyr, about as long ago as the main-sequence lifetime of A stars. These galaxies have been termed E + A galaxies since their spectra appears like a superposition of that of A-stars and that of otherwise normal elliptical galaxies. They are interpreted as being post-starburst galaxies. Since they were first seen in clusters, the interpretation of the origin of E + A galaxies was originally centered on the cluster environment—for example star-forming galaxies falling into a cluster and having their interstellar medium removed by tidal forces caused by the cluster potential well and/or stripping as the galaxies move through the intracluster medium. However, E + A galaxies were later also found in different environments, making the above interpretation largely obsolete. By investigating the spatial correlation of these galaxies with other galaxies shows that the phenomenon is not associated with the large-scale environment. An overdensity of neighboring galaxies can be seen only out to scales of $\sim$ 100 kpc. If the sudden turn-off of the star-formation activity is indeed caused by an external perturbation, it is therefore likely that it is caused by the dynamical interaction of close neighboring galaxies or by mergers. Indeed, about 30 % of E + A galaxies are found to have morphological signatures of perturbations, such as tidal tails, supporting the interaction hypothesis.

In fact, the spiral galaxies in clusters seem to differ statistically from those of field spirals, in that the fraction of disk galaxies with absorption-line spectra, and thus no ongoing star formation, seems to be larger in clusters than in the field by a factor ~ 4, indicating that the cluster environment has a marked impact on the star-formation ability of these galaxies.

6.8 Evolutionary effects

Today, we are able to discover and analyze clusters of galaxies at redshifts $z \sim 1$ and higher; thus the question arises whether these clusters have the same properties as local clusters. At $z \sim 1$ the age of the Universe is only about half of that of the current Universe. One might therefore expect an evolution of cluster properties.

Luminosity function. First, we shall consider the comoving number density of clusters as a function of redshift or, more precisely, the evolution of the luminosity function of clusters with z. As Fig. 6.65 demonstrates, such evolutionary effects are not very pronounced for moderate redshifts, and only at the highest luminosities or the most massive clusters, respectively, does an evolution become visible. The situation is somewhat different when one considers the evolution of the cluster abundance as a function of temperature: at redshift $z \sim 0.5$, the number of clusters above a given temperature is lower than at the current epoch by a factor ~ 3. Hence, there obviously is an evolution of the cluster population, in the sense that at high redshift, clusters of very high luminosity, high temperature, or very high mass are less abundant than they are today. The interpretation and the relevance of this fact will be discussed later (see Sect. 8.2.1). We also note that a weak redshift evolution of the X-ray luminosity function of clusters is compatible with a strong evolution of the cluster mass function, since according to (6.62), the relation between luminosity and mass evolves significantly with z

Butcher–Oemler effect. We saw in Chap. 3 that early-type galaxies are predominantly found in clusters and groups, whereas spirals are mostly field galaxies. For example, a massive cluster like Coma contains only 10 % spirals, the other luminous galaxies are ellipticals or S0 galaxies (see also Sect. 6.7.2). Besides these morphological differences, the colors of galaxies are very useful for a characterization: early-type galaxies (ellipticals and S0 galaxies) have little ongoing star formation and therefore consist mainly of old, thus low-mass and cool stars. Hence they are red, whereas spirals feature active star formation and are therefore distinctly bluer. The fraction of blue galaxies in nearby clusters is very low.

Butcher and Oemler found that this changes if one examines clusters of galaxies at higher redshifts: these contain a larger fraction of blue galaxies, thus of spirals (see Fig. 6.66). This means that the mixture of galaxies changes over time. In clusters, spirals must become scarcer with increasing cosmic time, e.g., by transforming into early-type galaxies. With 8-m class telescopes, such studies can be extended to much higher redshifts. It was found that the fraction of blue galaxies increases further, until at $z \gtrsim 1.3$ the blue fraction in clusters is essentially the same as in the field.

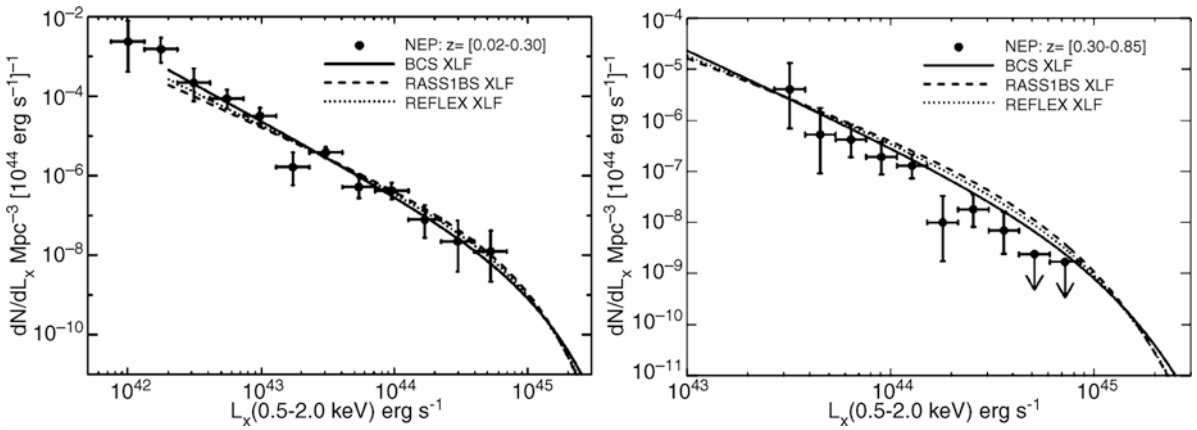

Fig. 6.65 X-ray luminosity function of galaxy clusters, as was obtained from a region around the north ecliptic pole (NEP), the region with the longest exposure time in the ROSAT All-Sky Survey (see Fig. 6.40). Plotted is $\mathrm{d}N/\mathrm{d}L_\mathrm{X}$, the (comoving) number density per luminosity interval, for clusters with $0.02 \leq z \leq 0.3$ (*left panel*) and $0.3 \leq z \leq 0.85$ (*right panel*), respectively. The luminosity was derived from the flux in the photon energy range from 0.5 to 2 keV. The *three different curves* specify the local luminosity function of clusters as found in other cluster surveys at lower redshifts. We see that evolutionary effects in the luminosity function are relatively small and become visible only at high L_X. Source: I.M. Gioia et al. 2001, *Cluster Evolution in the ROSAT North Ecliptic Pole Survey*, ApJ 553, L105, p. L106, Fig. 1. ©AAS. Reproduced with permission

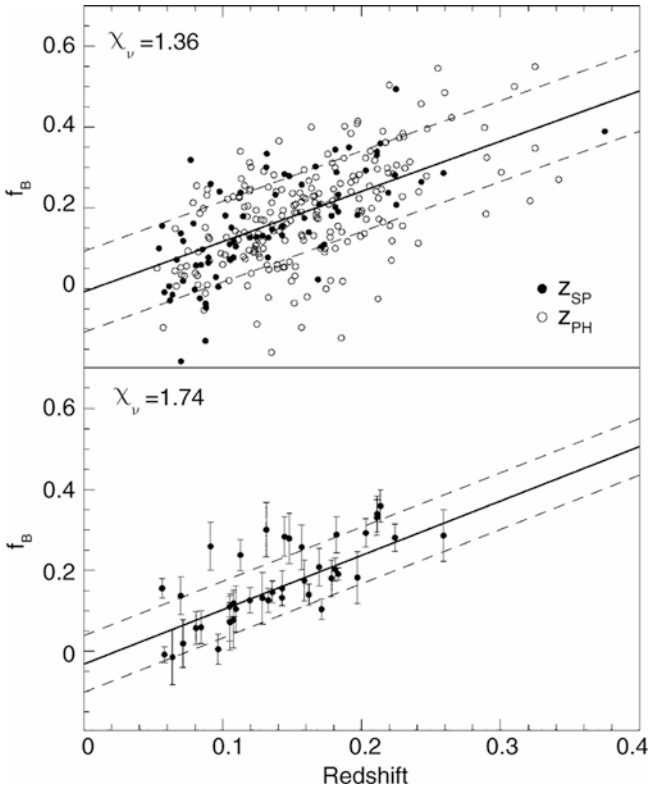

Fig. 6.66 Butcher–Oemler effect: in the *upper panel*, the fraction of blue galaxies f_b in a sample of 195 galaxy clusters is plotted as a function of cluster redshift, where *open* (*filled*) *circles* indicate photometric (spectroscopic) redshift data for the clusters. The *lower panel* shows a selection of clusters with spectroscopically determined redshifts and well-defined red cluster sequence. For the determination of f_b, foreground and background galaxies need to be statistically subtracted using control fields, which can also result in negative values for f_b. A clear increase in f_b with redshift is visible, and a line of regression yields $f_b = 1.34z - 0.03$. Source: V.E. Margoniner et al. 2001, *The Butcher-Oemler Effect in 295 Clusters: Strong Redshift Evolution and Cluster Richness Dependence*, ApJ 548, L143, p. L144, Fig. 1. ©AAS. Reproduced with permission

A possible and plausible explanation is that spirals lose their interstellar gas through ram-pressure stripping (Fig. 6.63), which is then mixed with the ICM. This is plausible because the ICM also has a high metallicity. These metals can only originate in a stellar population, thus in the enriched material in the ISM of galaxies.

Indeed, from the colors of cluster galaxies it is possible to derive very strict upper limits on their star formation in recent times. The color of cluster galaxies at high redshifts even provides interesting constraints on cosmological parameters—only those models are acceptable which have an age of the Universe, at the respective redshift, larger than the estimated age of the stellar population. One interesting example of this is presented in Fig. 6.67.

Therefore, we conclude from these observations that the stars in cluster galaxies formed at very early times in the Universe. But this does not necessarily mean that the galaxies themselves are also this old, because galaxies can be transformed into each other by merger processes (see Fig. 6.68). This changes the morphology of galaxies, but may leave the stellar populations largely unchanged.

At higher redshift (say, $z \gtrsim 0.5$), the fraction of clusters which show a cool core and which are therefore believed to be relaxed is smaller than in the current Universe. This observational finding is not unexpected, since the age of the Universe was smaller back then, and thus there was considerably less time for clusters to settle into an equilibrium state. Furthermore, the metallicity of the intracluster gas decreases towards higher redshifts, indicating that the enrichment of the gas is an ongoing process.

Clusters of galaxies at very high redshift. The search for clusters at high redshift is of great cosmological interest. As will be demonstrated in Sect. 7.5.2, the expected number density of clusters as a function of z strongly depends on the cosmological model. Hence, this search offers an opportunity to constrain cosmological parameters by the statistics of galaxy clusters.

The search for clusters in the optical (thus, by galaxy overdensities) becomes increasingly difficult at high z because of projection effects. Nevertheless, several groups have managed to detect clusters at $z \sim 0.8$ with this technique. In particular, the overdensity of galaxies in three-dimensional space can be analyzed if, besides the angular coordinates on the sphere, the galaxy colors are also taken into account. Because of the red cluster sequence, the overdensity is much more prominent in this space than in the sky projection alone.

Projection effects play a considerably smaller role in X-ray searches for clusters. With ROSAT, some clusters with $z \sim 1.2$ were found (see Fig. 6.39). The current X-ray satellites Chandra and XMM-Newton are more sensitive, and have detected several clusters with redshifts up to 2; two examples for clusters at $z \sim 1.4$ are shown in Figs. 6.69 and 6.70. These examples demonstrate that combining deep X-ray images with observations in the optical and the NIR is an efficient method of compiling samples of distant clusters. More recently, cluster detections using the Sunyaev–Zeldovich effect have obtained an increasingly prominent role in finding high-redshift clusters.

Through optical methods, it is also possible to identify galaxy concentrations at very high redshift. One approach is to assume that luminous AGNs at high redshift are found preferentially in regions of high overdensity, which is also expected from models of galaxy formation. With the redshift of the AGN known, the redshift at which one should search for an overdensity of galaxies near the AGN is defined. Those searches have proven to be quite successful; for instance, they are performed using narrow-band filter

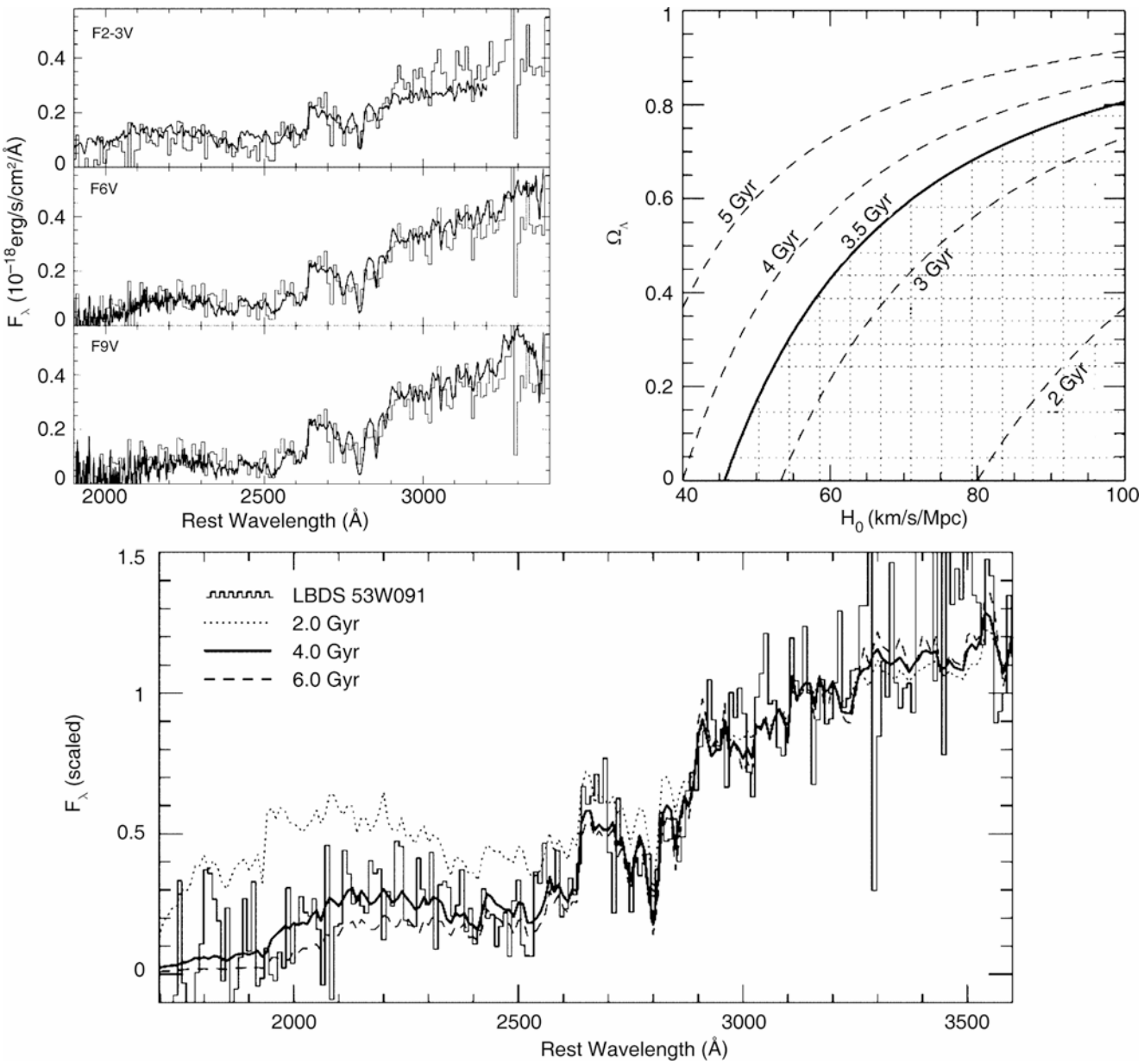

Fig. 6.67 The radio galaxy LBDS 53W091 has a redshift of $z = 1.552$, and it features a very red color ($R - K \approx 5.8$). Optical spectroscopy of the galaxy provides us with the spectral light distribution of the UV emission in the galaxy's rest frame. The UV light of a stellar population is almost completely due to stars on the upper main sequence—see Fig. 3.34. In the *upper left panel*, the spectrum of LBDS 53W091 is compared to those of different F stars; one can see that F6 stars match the spectral distribution of the galaxy nearly perfectly. In the *bottom panel*, synthetic spectra from population synthesis calculations are compared to the observed spectrum. A population with an age of about 4 Gyr represents the best fit to the observed spectrum; this is also comparable to the lifetime of F6 stars: the most luminous (still existing) stars dominate the light distribution of a stellar population in the UV. In combination, this reveals that this galaxy at $z = 1.552$ is at least 3 Gyr old. Phrased differently, the age of the Universe at $z = 1.55$ must be at least 3 Gyr. In the *upper right panel*, the age of the Universe at $z = 1.55$ is displayed as a function of H_0 and Ω_Λ (for $\Omega_\mathrm{m} + \Omega_\Lambda = 1$). Hence, this single galaxy provides significant constraints on cosmological parameters. Source: H. Spinrad et al. 1997, *LBDS 53W091: an Old, Red Galaxy at* $z = 1.552$, ApJ 484, 581, p. 587, 595, 599, Figs. 8, 17, 18. ©AAS. Reproduced with permission

photometry, with the filter centered on the redshifted Lyα line, tuned to the redshift of the AGN. Candidates need to be verified spectroscopically afterwards. One example of a strong galaxy concentration at $z = 4.1$ is presented in Fig. 6.71. The identification of a strong spatial concentration of galaxies is not sufficient to have identified a cluster of galaxies though, because it is by no means clear whether one has found a gravitationally bound system of galaxies (and the corresponding dark matter). Rather, such galaxy concentrations are considered to be the predecessors of galaxy clusters

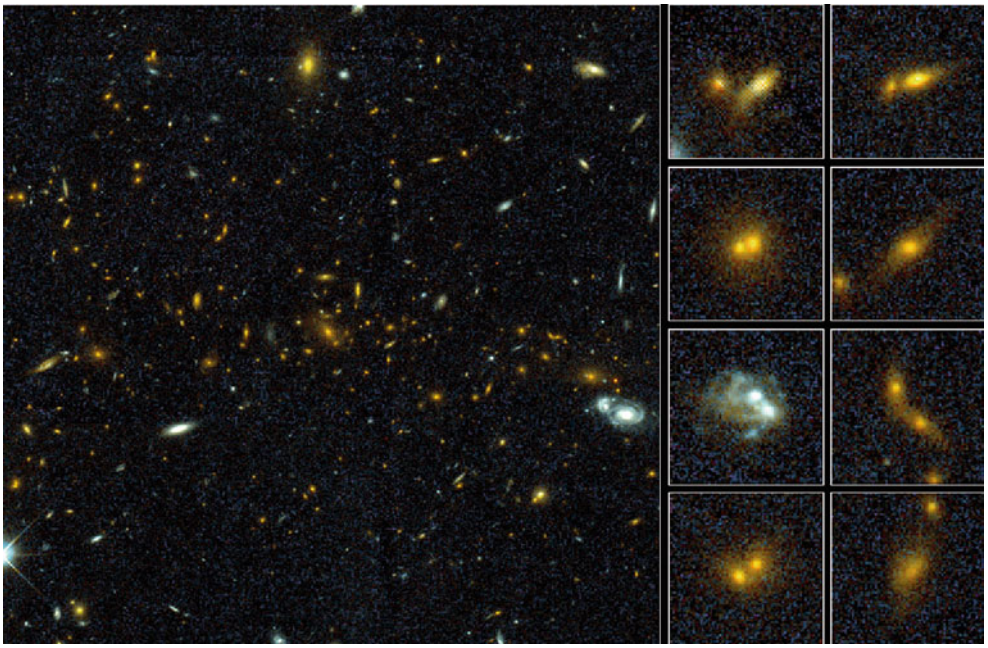

Fig. 6.68 The cluster of galaxies MS 1054−03, observed with the HST, is the most distant cluster in the EMSS X-ray survey ($z = 0.83$). The reddish galaxies in the image on the left form a nearly linear structure. This cluster is far from being spherical, as we have also seen from its weak lensing results (Fig. 6.55)—it is not relaxed. The smaller images on the right show blow-ups of selected cluster fields where mergers of galaxies become visible: in this cluster, the merging of galaxies is directly observable. At least six of the nine merging pairs found in this cluster have been shown to be gravitationally bound systems. Credit: P. van Dokkum, M. Franx/U. Groningen & U. Leiden, ESA, NASA

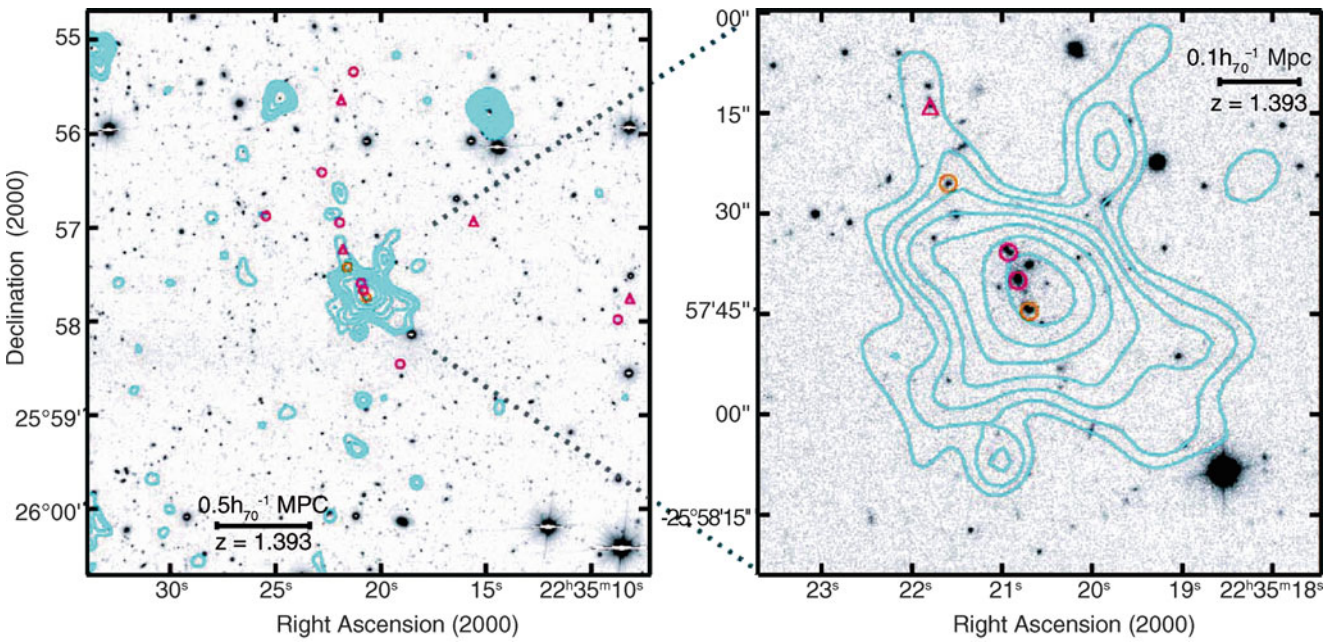

Fig. 6.69 The cluster of galaxies XMMU J2235.2−2557 was discovered in the field-of-view of an XMM-Newton image for which a different source was the original target. The image *on the left* shows the X-ray contours, superposed on an R-band image, while the image *on the right* shows the central section, here superposed on a K-band image. Galaxies in the field follow a red cluster sequence if the color is measured in $R - z$. The *symbols* denote galaxies at redshift $1.37 < z < 1.40$. The strong X-ray source to the upper right of the cluster center is a Seyfert galaxy at lower redshift. Until 2005, this cluster was the most distant X-ray selected cluster known, with a temperature of ~ 6 keV and a velocity dispersion of $\sigma \sim 750$ km/s. Source: C.R. Mullis et al. 2005, *Discovery of an X-Ray-luminous Galaxy Cluster at z=1.4*, ApJ 623, L85, p. L86, Fig. 1.

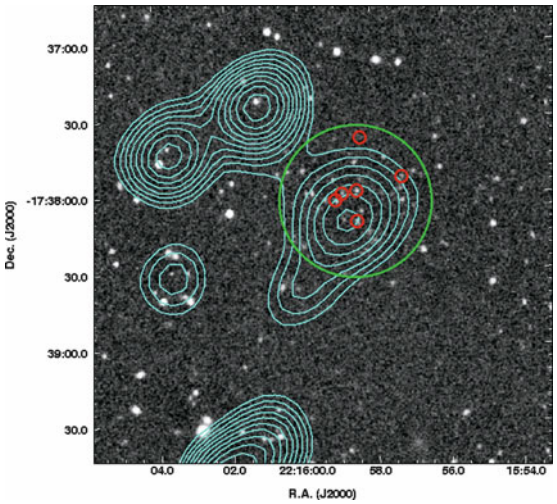

Fig. 6.70 A K_s-band image of the field containing the cluster XMMXCS J2215.9−1738, superposed by the contours of the X-ray emission observed with XMM-Newton. The cluster was discovered by XMM-Newton as an extended X-ray source, close to the center of this $3' \times 3'$ field; the other three nearby X-ray sources are unrelated point sources. The spectra of six member galaxies identified this as a cluster at $z = 1.45$, one of the highest redshift X-ray detected clusters known. The temperature of the cluster is measured to be $\sim 7\,\mathrm{keV}$, signalling a very massive object, a conclusion also obtained from the high X-ray luminosity. Source: S.A. Stanford et al. 2006, *The XMM Cluster Survey: A Massive Galaxy Cluster at z = 1.45*, ApJ 646, L13, p. L14, Fig. 1. ©AAS. Reproduced with permission

which will only evolve into bound systems during later cosmological evolution; they are thus often called 'proto-clusters'.

6.9 Problems

6.1. The virial radius. In Sect. 7.5.1 we will show, on the basis of the spherical collapse model, that the mean density within a virialized region is about 200 times the critical density of the Universe at the time of collapse. We will derive here an alternative and simple argument for that statement.

1. Consider a circular orbit with radius r_{200} of a particle in a dark matter halo of mass M_{200}. Calculate the orbital time and show that it depends only on the mean density of the halo inside the orbit, $t_{\rm orbit} \propto \bar{\rho}^{-1/2}$. Thus, this orbital time does not depend on the mass (or radius) of the halo. Recall that the free-fall time $t_{\rm ff}$ (see Problem 4.7) has the same dependence on $\bar{\rho}$—what is their ratio?
2. By setting the mean density to be $200\rho_{\rm cr}(z)$, show that the orbital time is, up to a factor of order unity, the age of the Universe at the time of the halo formation, i.e., the time of collapse!

Thus, for a halo characterized by a mean density of 200 times the critical density $\rho_{\rm cr}(z)$, a particle at the outer edge can finish one orbit within the age of the Universe at redshift z. Since the time scale for relaxation cannot be smaller than the

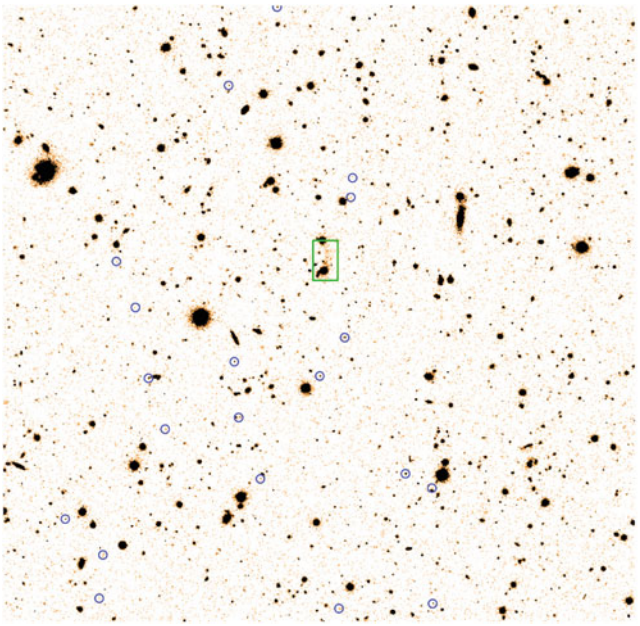

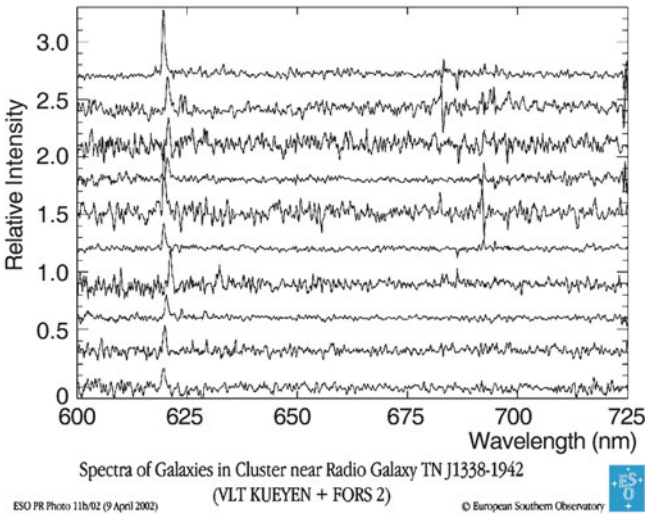

Fig. 6.71 The most distant known group of galaxies. The region around the radio galaxy TN J1338−1942 ($z = 4.1$) was scanned for galaxies at the same redshift; 20 such galaxies were found with the VLT, marked by *circles* in *the left image*. For ten of these galaxies, the spectra are shown *on the right*; in all of them, the Lyα emission line is clearly visible. Hence, groups of galaxies were already formed in an early stage of the Universe. Credits: B. Venemans, G. Miley et al., European Southern Observatory

time a particle needs to orbit through the region, the choice $\bar{\rho} = 200\rho_{\rm cr}(z)$ is indeed plausible.

6.2. Cosmological surface brightness dimming. Consider a source of bolometric luminosity L and radius R, and show that its bolometric surface brightness decreases with redshift $\propto (1+z)^{-4}$. Calculate the redshift dependence of the specific surface brightness I_ν if the source has a power-law spectrum, $L_\nu \propto \nu^{-\alpha}$.